Enabling Technologies for Coherent Optical Communications

Mostafa Khalil

Department of Electrical & Computer Engineering

McGill University, Montreal

May 2024

A thesis submitted to McGill University in partial fulfillment of the requirements of the degree of Doctor of Philosophy.

Abstract

In recent years, silicon photonics has emerged as a promising technology for optical communication systems. The integration of silicon photonics with other materials and technologies has opened up new avenues for developing high-performance and cost-effective optical communication systems. This has led to significant research and development efforts in the field, intending to achieve better performance, higher integration, and lower power consumption. In this thesis, we aim to address an intriguing question - what would coherent transceivers look like in the future to serve high-capacity wavelength division multiplexing (WDM) systems?

In the first part of the thesis, we propose a wavelength-selective filter based on waveguide Bragg gratings (WBG) on the Silicon-on-insulator (SOI) platform. The proposed WBG has 6 equidistant heater segments with a single heater element on top of the silicon waveguide, and each segment can be controlled to control the refractive index of the corresponding segment. The proposed device not only provides control of the resonance wavelength but can also provide multi-band rejection filters and Fabry-Pérot-like filters. Another design is also proposed based on a tilted heater element to create chirped WBGs. We perform a comprehensive simulation analysis and validate it with experimental results. We believe such devices can be further optimized for use in optical signal processing applications or to create chirped or phase-shifted grating structures. Furthermore, we design and propose 3-cascaded

Mach–Zehnder modulators on the SOI platform, and investigate the feasibility of generating optical frequency combs with such devices.

Among the various optical frequency comb generators, quantum dash mode-locked laser diodes (QD-MLLDs) are potential candidates for future WDM transceivers. QD-MLLDs can emit a broadband of optical carriers with a fixed frequency spacing between each carrier. QD-MLLDs have many features such as narrow linewidth, compact size, and simple operation. In the second part of the thesis, we demonstrate the performance of such devices to serve high-capacity coherent optical systems. Our experimental results showcase that QD-MLLDs can be exploited for coherent transmission over 80 km of standard single-mode fiber (SSMF) using various modulation formats from QPSK to 64QAM, and symbol rates up to 120 GBd. Our WDM transmission experiments report aggregate bit rates of 4 Tb/s in a single polarization configuration. We illustrate that each channel generated by the QD-MLLD achieves an impressive net line rate of 447.8 Gb/s. Additionally, we conduct a thorough performance comparison between QD-MLLDs and a narrow linewidth integrable tunable laser assembly (ITLA). Moreover, we demonstrate that such devices can be used not only as multi-wavelength sources at the WDM transmitter but also as multi-wavelength local oscillators (LOs) at the receiver side for coherent detections of WDM signals. We also show that the frequency spacing between the comb lines can be programmed, enabling support for higher symbol rates in super-channel WDM transmissions. Lastly, thanks to the possibility of hybrid integration, we propose a schematic for future coherent optical transceivers using chip-scale optical frequency comb sources, such as QD-MLLDs, and silicon photonic modulators.

In the last part of the thesis, we propose and verify, both analytically and experimentally, innovative encryption techniques to safeguard sensitive data. We propose an encryption technique utilizing a phase modulator at the transmitter side and based on a roundtrip mech-

anism wherein an authenticated user does not share the secret key with other entities. Then, we introduce a quantum-inspired encryption technique for one-way transmission, which is based on displacing the modulated symbol randomly with random amplitudes and phases. Only the authenticated user would be able to decrypt the signal with the correct secret key after performing synchronization processes. We finally show that the proposed techniques can be used in the existing optical fiber links and are protected against eavesdropping attacks wherein adversaries tap into the fiber link to steal sensitive information. All the experimental results are taken at a high symbol rate of 56 GBd with various modulation formats including 4/16/32QAM.

Abrégée

Au cours des dernières années, la photonique au silicium a émergé comme une technologie prometteuse pour les systèmes de communication optique. L'intégration de la photonique au silicium avec d'autres matériaux et technologies a ouvert de nouvelles perspectives pour le développement de systèmes de communication optique haute performance et rentables. Cela a conduit à d'importants efforts de recherche et développement dans le domaine, visant à obtenir de meilleures performances, une intégration plus élevée et une consommation d'énergie réduite. Dans cette thèse, nous avons pour objectif de répondre à une question intrigante : à quoi ressembleraient les émetteurs-récepteurs cohérents dans le futur pour servir les systèmes de multiplexage par répartition en longueur d'onde (WDM) à haute capacité?

Dans la première partie de la thèse, nous proposons un filtre sélectif en longueur d'onde basé sur des réseaux de Bragg à guides d'ondes (WBG) sur la plateforme Silicium-sur-isolant (SOI). Le WBG proposé comporte 6 segments de chauffage équidistants avec un seul élément chauffant au-dessus du guide d'ondes en silicium, et chaque segment peut être contrôlé pour réguler l'indice de réfraction du segment correspondant. Le dispositif proposé permet non seulement de contrôler la longueur d'onde de résonance, mais peut également fournir des filtres de rejet à bandes multiples et des filtres de type Fabry-Pérot. Un autre concept est également proposé en utilisant un élément chauffant incliné pour créer des réseaux de Bragg à pente variable. Nous réalisons une analyse de simulation approfondie et la validons avec

des résultats expérimentaux. Nous pensons que de tels dispositifs peuvent être optimisés davantage pour une utilisation dans des applications de traitement optique du signal ou pour créer des structures de réseaux de diffraction à pente variable ou déphasées. De plus, nous concevons et proposons des modulateurs Mach–Zehnder en cascade à 3 étages sur la plateforme SOI et étudions la faisabilité de générer des peignes de fréquence optique avec de tels dispositifs.

Parmi les divers générateurs de peignes de fréquence optique, les lasers à verrouillage de mode à boîtier quantique (QD-MLLDs) sont des candidats potentiels pour les futurs émetteurs-récepteurs WDM. Les QD-MLLDs peuvent émettre une large bande de porteuses optiques avec un espacement fixe entre chaque porteuse. Les QD-MLLDs présentent de nombreuses caractéristiques telles qu'une largeur de raie étroite, une taille compacte et un fonctionnement simple. Dans la deuxième partie de la thèse, nous démontrons les performances de tels dispositifs pour servir les systèmes optiques cohérents à haute capacité. Nos résultats expérimentaux montrent que les QD-MLLDs peuvent être exploités pour une transmission cohérente sur 80 km de fibre monomode standard (SSMF) en utilisant divers formats de modulation, du QPSK au 64QAM, et des débits symboles allant jusqu'à 120 Gbit/s. Nos expériences de transmission WDM rapportent des débits binaires agrégés de 4 Tbit/s dans une configuration de polarisation unique. Nous illustrons que chaque canal généré par le QD-MLLD atteint un impressionnant débit net de ligne de 447,8 Gbit/s. De plus, nous effectuons une comparaison approfondie des performances entre les QD-MLLDs et un ensemble laser accordable intégrable à raie étroite (ITLA). De plus, nous démontrons que de tels dispositifs peuvent être utilisés non seulement comme sources multi-longueurs d'onde à l'émetteur WDM, mais aussi comme oscillateurs locaux (LOs) multi-longueurs d'onde côté récepteur pour la détection cohérente des signaux WDM. Nous montrons également que l'espacement en fréquence entre les lignes du peigne peut être programmé, permettant de prendre en

charge des débits symboles plus élevés dans les transmissions WDM de super-canaux. Enfin, grâce à la possibilité d'intégration hybride, nous proposons un schéma pour les futurs émetteurs-récepteurs optiques cohérents utilisant des sources de peigne de fréquence optique à l'échelle de la puce, telles que les QD-MLLDs, et des modulateurs photoniques en silicium.

Dans la dernière partie de la thèse, nous proposons et vérifions, à la fois analytiquement et expérimentalement, des techniques de chiffrement innovantes pour protéger des données sensibles. Nous proposons une technique de chiffrement utilisant un modulateur de phase côté émetteur et basée sur un mécanisme de va-et-vient, dans lequel un utilisateur authentifié ne partage pas la clé secrète avec d'autres entités. Ensuite, nous introduisons une technique de chiffrement inspirée de la physique quantique pour une transmission unidirectionnelle, basée sur le déplacement aléatoire du symbole modulé avec des amplitudes et des phases aléatoires. Seul l'utilisateur authentifié serait capable de décrypter le signal avec la clé secrète correcte après avoir effectué des processus de synchronisation. Nous montrons enfin que les techniques proposées peuvent être utilisées dans les liaisons de fibre optique existantes et sont protégées contre les attaques d'écoute, où des adversaires se branchent sur la liaison en fibre pour voler des informations sensibles. Toutes les résultats expérimentaux sont obtenus à un débit binaire symbole élevé de 56 Gbit/s avec divers formats de modulation, y compris 4/16/32QAM.

Acknowledgements

I would like to express my special thanks to my supervisor, Prof. *Lawrence R. Chen*, for his great efforts, fruitful academic advice, constant encouragement, patience, guidance, and support during my MEng. and Ph.D. degrees at McGill University. I feel honored to have been given this great opportunity to work with him and contribute to research under his supervision since 2018. Not only that, but I admire his professionalism, charisma, and insightful criticism.

I also would like to thank Prof. *David V. Plant* for the trust he has placed in me, and his excellent collaboration and support to make this work happen.

Special thanks to Prof. *Thomas Szkopek* and Prof. *Dennis Giannacopoulos* for their supervision during my teaching assistantship.

Special thanks to *Essam Berikaa* for being more than a brother. His support and help during my Ph.D. were priceless. Thank you for the great time and encouragement throughout this journey. I am grateful for everything you have done for me.

I deeply thank the photonics group members at McGill University, especially *Md Samiul Alam* for his expertise and collaboration in the lab, *Kh. A. Shahriar* for his help and collaboration in the lab, *Zixian Wei* for his impressive ideas and advice, *Hao Sun* for his academic advice and fun time, *Bruno Taglietti* for his help and discussions, and *Yuxuan Xie* for his help. I also thank the rest of the group members for creating a friendly atmosphere.

I would like to express my deep appreciation and pay humble respects to my parents for everything. Without their extreme sacrifice and honest prayers, this journey could have never been possible. For my brother, Dr. *Mohammed Khalil*, you have been always a true inspiration to learn from. Thank you for your motivation, support, and everything you have been doing to see my success.

To my father-in-law and his precious family, Dr. *Amr Abdeldayem*, words do not exist to describe how grateful I am for everything you have done, do and still doing for me. To my precious and lovely fiancée, the deepest thanks from my heart go to you. Her unconditional love changed my life for the better, and her share of success in this thesis is just as mine if not more. I feel extremely blessed to have her beside me during this journey while building our future and wish to keep her always standing by my side for the rest of my life.

Lastly, "The deeds are considered by the intentions, and a person will get the reward according to his intention." I hope this work becomes beneficial knowledge from which benefit is derived.

Mostafa Khalil

February 2024

Associated Publications

My journey at McGill was very fruitful; it resulted in 29 different publications: 11 journal papers and 18 conference papers. The paper titled "Performance of Quantum-Dash Mode-Locked Laser Diode (QD-MLLD) for Data Rates Beyond Tb/s in WDM Coherent Transmission Over 80 km-SMF," got upgraded to an invited talk at SPPCom Advanced Photonic Congress in Busan, South Korea in July 2023. I traveled and presented there, and I received the best paper and presentation award at the conference.
The associated publications to this thesis are 14: 4 journal papers and 10 conference papers. My contributions to these papers are detailed here.

Related Publications

Journal Articles

1. **M. Khalil**, A. Chan, L. R. Chen, D. V. Plant, and R. Kuang, "Experimental demonstration of quantum encryption in phase space with displacement operator in coherent optical communications," EPJ Quantum Technology (submitted).

    - **M. Khalil** built the experimental setup, conducted the experiments, proposed the dual-polarization encryption, performed all the BER measurements, analyzed

the results, and wrote the manuscript. He also participated in the simulation analysis with A. Chan.

- R. Kuang proposed displacement operator encryption.
- A. Chan performed simulation analysis.
- D. V. Plant and L. R. Chen revised the manuscript and supervised the experiments.

2. **M. Khalil**, Y. Xie, E. Berikaa, J. Liu, Z. Lu, P. J. Poole, G. Liu, J. Weber, D. V. Plant, and L. R. Chen, "Performance of quantum-dash mode-locked lasers (QD-MLLDs) for high-capacity coherent optical communications," Optics Express, 32, pp. 217–229, Jan 2024.

   - **M. Khalil** built the experimental setup, conducted the experiments, conceived the idea of using the QD-MLLD as signal carriers and local oscillators, performed all the BER measurements with and without the silicon photonic modulator, analyzed the results, and wrote the manuscript.
   - E. Berikaa helped to build the experimental setup and the silicon photonic modulator characterization.
   - J. Liu, Z. Lu, P. J. Poole, G. Liu, and J. Weber developed the comb source at the National Research Council Canada, and revised the manuscript.
   - Y. Xie revised the manuscript.
   - D. V. Plant supervised the experiments.
   - L. R. Chen supervised the experiments, gave insightful comments and suggestions, and revised the manuscript.

3. A. Chan, **M. Khalil**, K. A. Shahriar, D. V. Plant, L. R. Chen, and R. Kuang, "Encryption in phase space for classical coherent optical communications," Scientific Reports, 13, p. 12965, Aug 2023.

    - **M. Khalil** conducted the experiments with K. A. Shahriar.
    - A. Chan performed the simulation analysis and wrote the manuscript.
    - All authors revised the manuscript.

4. **M. Khalil**, H. Sun, E. Berikaa, D. V. Plant, and L. R. Chen, "Electrically reconfigurable waveguide Bragg grating filters," Optics Express, 30, pp. 39643–39651, Oct 2022.

    - **M. Khalil** conceived the idea, performed the simulations, conducted the experiments, and wrote the manuscript.
    - H. Sun and E. Berikaa helped with the simulation.
    - D. V. Plant revised the manuscript.
    - L. R. Chen supervised the work, gave insightful suggestions, and revised the manuscript.

Conference Articles

5. **M. Khalil**, L. R. Chen, D. V. Plant, and R. Kuang, "Quantum-inspired encryption using displacement operators in coherent optical communications," in SPPCom Advanced Photonics Congress, (submitted).

    - **M. Khalil** built the experimental setup, conducted the experiments, performed all the BER measurements, analyzed the results, and wrote the manuscript.

- R. Kuang proposed displacement operator encryption.
- D. V. Plant and L. R. Chen revised the manuscript and supervised the experiments.

6. **M. Khalil**, H. Sun, T. Papatheodorakos, L. R. Chen, "Optical frequency comb generation using integrated cascaded MZMs on SOI," Photonics North (PN), (Accepted April, 2024).

    - **M. Khalil** helped with designing the device with H. Sun, built the experimental setup, conducted the experiments, analyzed the results, and wrote the manuscript.
    - H. Sun designed the device and conducted the EO responses of the modulators.
    - T. Papatheodorakos conducted part of the experiment.
    - L. R. Chen supervised the experiments, gave insightful feedback, and revised the manuscript.

7. **M. Khalil**, E. Berikaa, M. S. Alam, K. A. Shahriar, Y. Xie, J. Liu, Z. Lu, P. J. Poole, J. Weber, D. V. Plant, and L. R. Chen, "Performance of quantum-dash mode-locked laser diode (QD-MLLD) for data rates beyond Tb/s in WDM coherent transmission over 80 km-SMF," in Advanced Photonics Congress 2023, Technical Digest Series (Optica Publishing Group, 2023), paper SpW4E.2.

    - **M. Khalil** built the experimental setup, conducted the experiments, performed all the BER measurements, analyzed the results, wrote the manuscript, and presented the manuscript in Busan, South Korea.
    - E. Berikaa, M. S. Alam, and K. A. Shahriar helped to build the experimental setup.

- J. Liu, Z. Lu, P. J. Poole, G. Liu, and J. Weber developed the comb source at the National Research Council Canada, and revised the manuscript.
- Y. Xie revised the manuscript.
- D. V. Plant supervised the experiments.
- L. R. Chen supervised the experiments, gave insightful comments and suggestions, and revised the manuscript.

8. K. A. Shahriar, **M. Khalil**, A. Chan, L. R. Chen, R. Kuang and D. V. Plant, "Security performance of physical-layer encryption based on randomized phase space in optical fiber communication," 2022 IEEE Photonics Conference (IPC), Vancouver, BC, Canada, pp. 1-2, 2022.

   - **M. Khalil** built the experimental setup and conducted the experiments with K. A. Shahriar.
   - K. A. Shahriar analyzed the results, wrote the manuscript, and presented the paper.
   - A. Chan performed simulation analysis.
   - R. Kuang proposed the idea.
   - D. V. Plant and L. R. Chen supervised the experiments and revised the manuscript.

9. K. A. Shahriar, **M. Khalil**, A. Chan, L. R. Chen, R. Kuang, and D. V. Plant, "Enhancing data security in optical fiber communication through dual layer encryption with randomized phases," in Frontiers in Optics + Laser Science 2022 (FIO, LS), Technical Digest Series (Optica Publishing Group, 2022), paper JW5A.80.

- **M. Khalil** built the experimental setup and conducted the experiments with K. A. Shahriar.
- K. A. Shahriar analyzed the results, wrote the manuscript, and presented the paper.
- A. Chan performed simulation analysis.
- R. Kuang proposed the idea.
- D. V. Plant and L. R. Chen supervised the experiments and revised the manuscript.

10. **M. Khalil**, H. Sun, and L. R. Chen, "Electrically reconfigurable waveguide Bragg gratings for multiple tunable wavelength-division multiplexing filters," in Optica Advanced Photonics Congress 2022, Technical Digest Series (Optica Publishing Group, 2022), paper ITh2B.6.

    - **M. Khalil** conceived the idea, performed the simulation analysis, conducted the experiments, wrote the manuscript and presented the paper.
    - H. Sun helped with the simulation analysis.
    - L. R. Chen supervised the experiments and revised the manuscript.

11. A. Chan, **M. Khalil**, K. A. Shahriar, L. R. Chen, D. V. Plant and R. Kuang, "On the security of an optical layer encryption using coherent-based TF-QKD in classical optical fiber links," 2022 4th International Conference on Computer Communication and the Internet (ICCCI), Chiba, Japan, pp. 105-110, 2022.

    - **M. Khalil** participated in the simulation analysis with A. Chan.
    - A. Chan performed the simulations, wrote the manuscript and presented the paper.

- The rest of the authors revised the manuscript.

12. K. A. Shahriar, **M. Khalil**, A. Chan, L. R. Chen, R. Kuang, and D. V. Plant, "Physical-layer secure optical communication based on randomized phase space in pseudo-3-party infrastructure," in Conference on Lasers and Electro-Optics, Technical Digest Series (Optica Publishing Group, 2022), paper SF4L.3.

    - **M. Khalil** built the experimental setup and conducted the experiments with K. A. Shahriar.
    - K. A. Shahriar analyzed the results, wrote the manuscript, and presented the paper.
    - A. Chan and R. Kuang revised the manuscript.
    - D. V. Plant and L. R. Chen supervised the experiments and revised the manuscript.

13. A. Chan, **M. Khalil**, K. A. Shahriar, L. R. Chen, D. V. Plant and R. Kuang, "Security analysis of a next-generation TF-QKD for secure public key distribution with coherent detection over classical optical fiber networks," 2021 7th International Conference on Computer and Communications (ICCC), Chengdu, China, pp. 416-420, 2021.

    - **M. Khalil** participated in the simulation analysis with A. Chan.
    - A. Chan performed the simulations, wrote the manuscript and presented the paper.
    - The rest of the authors revised the manuscript.

14. **M. Khalil**, A. Chan, K. A. Shahriar, L. R. Chen, D. V. Plant and R. Kuang, "Security performance of public key distribution in coherent optical communications links," 2021

3rd International Conference on Computer Communication and the Internet (ICCCI), Nagoya, Japan, pp. 123-129, 2021.

- **M. Khalil** performed the simulation analysis, wrote the manuscript and presented the paper.
- A. Chan and K. A. Shahriar helped with the simulations.
- The rest of the authors revised the manuscript.

Unrelated Publications

For the following journal and conference papers, I actively contributed to the conducted experiments and the writing process.

Journal Articles

15. Y. Xie, **M. Khalil**, H. Sun, S. Moosabhoy, J. Liu, Z. Lu, P. J. Poole, J. Weber, and L. R. Chen, "Photonic beamforming using a quantum-dash optical frequency comb source," Applied Optics 62, pp. 8696-8701, 2023.

16. Z. Wei, C. Nacke, **M. Khalil**, H. Sun, K. Stitt, J. Lougheed, L. R. Chen, and D. V. Plant, "AL-aided AMC in a multi-user white-light OFDMA VLC system over a light-diffusing fiber loop," Optics Letters 48, pp. 3661-3664, 2023.

17. Y. Xie, **M. Khalil**, H. Sun, L. R. Chen, S. Moosabhoy, J. Liu, Z. Lu, P. J. Poole, and J. Weber, "Photonic beamforming using quantum-dash mode-locked frequency comb laser," 2022 IEEE International Topical Meeting on Microwave Photonics (MWP), Orlando, FL, USA, pp. 1-4, 2022.

18. H. Sun, **M. Khalil**, J. Liu, Z. Lu, P. J. Poole, J. Weber, D. V. Plant, and L. R. Chen, "Reconfigurable microwave photonic filter based on a quantum dash mode-locked laser," Optics Letters 47, 1133-1136, 2022.

19. H. Sun, **M. Khalil**, Z. Wang and L. R. Chen, "Recent progress in integrated electro-optic frequency comb generation," Journal of Semiconductors, 42, 041301, 2021.

20. Y. Wang, H. Sun, **M. Khalil**, W. Dong, I. Gasulla, J. Capmany, and L. R. Chen, "On-chip optical true time delay lines based on subwavelength grating waveguides," Optics Letters 46, 1405-1408, 2021.

21. Z. Wang, M. Ma, H. Sun, **M. Khalil**, R. Adams, K. Yim, X. Jin, and L. R. Chen, "Optical frequency comb generation using CMOS compatible cascaded Mach–Zehnder modulators," in IEEE Journal of Quantum Electronics, 55, 6, pp. 1-6, Dec. 2019.

Conference Articles

22. Y. Xie, **M. Khalil**, J. Liu, Z. Lu, P. J. Poole, J. Weber, and L. R. Chen, "Reconfigurable microwave photonic filter with linear amplitude response based on quantum dash mode-locked laser for instantaneous frequency measurement," 2023 IEEE Photonics Conference (IPC), Orlando, FL, USA, pp. 1-2, 2023.

23. L. R. Chen, **M. Khalil**, Y. Xie, H. Sun, E. Berikaa, M. S. Alam, D. V. Plant, J. Liu, and Z. Lu, "Quantum dash optical frequency comb sources for optical communications and microwave photonics." Photonics North (PN), p. 1, 2023.

24. H. Sun, **M. Khalil**, D. V. Plant, L. R. Chen, J. Liu, Z. Lu, P. J. Poole, and J. Weber, "Reconfigurable microwave photonics filters with negative coefficients based on

a quantum dash mode-locked laser," 2021 International Topical Meeting on Microwave Photonics (MWP), Pisa, Italy, pp. 1-4, 2021.

25. H. Sun, **M. Khalil**, D. V. Plant, L. R. Chen, J. Liu, Z. Lu, P. J. Poole, and J. Weber, "Reconfigurable microwave photonic filter enabled by a quantum dash mode-locked laser," 2021 IEEE Photonics Conference (IPC), Vancouver, BC, Canada, 2021.

26. Y. Wang, H. Sun, **M. Khalil**, W. Dong, I. Gasulla, J. Capmany, L. R. Chen, "Multi-cavity optoelectronic oscillators based on an integrated array of subwavelength grating waveguides," 2020 International Topical Meeting on Microwave Photonics (MWP), Matsue, Japan, pp. 184-187, 2020.

27. Y. Wang, H. Sun, **M. Khalil**, L. R. Chen and W. Dong, "Photonic beamforming based on subwavelength gratings on-chip optical true time delay lines," 2020 IEEE Photonics Conference (IPC), Vancouver, BC, Canada, pp. 1-2, 2020.

28. **M. Khalil**, R. Maram, B. Naghdi, A. Samani, M. Jacques, L. R. Chen, and D. V. Plant, "Electro-optic frequency comb generation using cascaded silicon microring modulators," in OSA Advanced Photonics Congress (AP) 2020 (IPR, NP, NOMA, Networks, PVLED, PSC, SPPCom, SOF), L. Caspani, A. Tauke-Pedretti, F. Leo, and B. Yang, eds., OSA Technical Digest (Optica Publishing Group, 2020), paper IM3A.6.

29. Z. Wang, M. Ma, H. Sun, **M. Khalil**, X. Jin, K. Yim, L. R. Chen, R. Adams, "On-chip frequency comb generation using cascaded MZMs in SiP for microwave photonics applications," 2019 International Topical Meeting on Microwave Photonics (MWP), Ottawa, ON, Canada, pp. 1-3, 2019.

Contents

List of Figures

List of Tables

Acronyms

ADC Analog-to-Digital Converter.

AMF Advanced Micro Foundry.

ASE Amplified Spontaneous Emission.

AWG Arbitrary Waveform Generator.

BER Bit Error Ratio.

BPD Balanced Photodiode.

BPS Blind Phase Search.

CBE Chemical Beam Epitaxy.

CD Chromatic Dispersion.

CMOS Complementary Metal-Oxide-Semiconductor.

CW Continuous Wave.

DAC Digital-to-Analog Converter.

DDPLL Decision-Directed Phase-Locked Loop.

DFB Distributed Feedback.

DOCS Displacement Operator in Coherent States.

DP-IQM Dual-Polarization In-phase and Quadrature Modulator.

DSP Digital Signal Processing.

DWDM Dense Wavelength-Division Multiplexing.

EDFA Erbium-Doped Fiber Amplifier.

EME Eigenmode Expansion.

ENoB Effective Number of Bits.

EO Electro-Optic.

EPS Encryption in Phase Space.

ESA Electrical Spectrum Analyzer.

FAU Fiber Array Unit.

FDTD Finite-Difference Time-Domain.

FEC Forward Error Correction.

FFT Fast Fourier Transform.

FO Frequency Offset.

FP Fabry-Pérot.

FROG Frequency-Resolved Optical Gating.

FSR Free Spectral Range.

FWHM Full Width at Half Maximum.

GaAs Gallium Arsenide.

GVD Group Velocity Dispersion.

HD Hard Decision.

IM/DD Intensity Modulation and Direct Detection.

InP Indium Phosphide.

IQ In-phase and Quadrature.

ISI Inter-Symbol Interference.

ITLA Integrable Tunable Laser Assembly.

LDC Laser Diode Controller.

LMS Least Mean Squares.

LO Local Oscillator.

MIMO Multiple-Input Multiple-Output.

MOCVD Metal-Organic Chemical Vapor Deposition.

MZI Mach-Zehnder Interferometer.

MZM Mach-Zehnder modulators.

NLLUT Nonlinear Lookup Table.

NLPD Nonlinear Pre-Distortion.

OCNR Optical Carrier-to-Noise power Ratios.

OFC Optical Frequency Comb.

OH overhead.

OOK On-Off Keying.

OSA Optical Spectrum Analyser.

OSNR Optical Signal-to-Noise Power Ratio.

OTDM Optical Time Division Multiplexing.

PAM Pulse Amplitude Modulation.

PAPR Peak-to-Average Power Ratio.

PBC Polarization Beam Combiner.

PBS Polarization Beam Splitter.

PC Polarization Controller.

PD Photodiode.

PDM Polarization Division Multiplexing.

PICs Photonic Integrated Circuits.

PLL Phase Locked Loop.

PM Phase Modulator.

PMD Polarization Mode Dispersion.

PRBS Pseudo-Random Binary Sequence.

QAM Quadrature Amplitude Modulation.

QD Quantum Dot/Dash.

QD-MLLD Quantum Dash Mode-Locked Laser Diode.

QKD Quantum Key Distribution.

QPSK Quadrature Phase Shift Keying.

QW Quantum Well.

RF Radio Frequency.

RIN Relative Intensity Noise.

ROP Received Optical Power.

RRC Root Raised Cosine.

RTO Real-Time Oscilloscope.

SD Soft Decision.

Si Silicon.

SiO_2 Silicon Dioxide.

SiP Silicon Photonics.

SNR Signal-to-Noise Ratio.

SOI Silicon-on-Insulator.

sps samples per symbol.

SSMF Standard Single-Mode Fibers.

TBPF Tunable Band-Pass Filter.

TEC Thermoelectric Cooler.

TiN Titanium Nitride.

TMM Transfer-Matrix Method.

VGC Vertical Grating Coupler.

VNA Vector Network Analyzer.

WBG Waveguide Bragg Grating.

WDM Wavelength Division Multiplexing.

Chapter 1

Introduction

1.1 Motivation

"Can we schedule an online meeting to discuss this"? has become a frequently asked question in the last few years. This increase in online communications has driven the rapid expansion of bandwidth-intensive applications, such as video streaming, cloud-based services, artificial intelligence, and many more. According to the Silicon Photonics 2023 report by Yole Group [1], the market value of silicon Photonic Integrated Circuits (PICs) was approximately US$68 million in 2022. The forecast indicates substantial growth, with expectations to exceed US$613 million by 2028, demonstrating a remarkable 44% Compound Annual Growth Rate (CAGR) in the period 2022-2028, see Fig. 1.1. The primary catalyst for this surge is anticipated to be the demand for 800G high-data-rate pluggable modules, driving the expansion of fiber-optic network capacity.

There are various approaches to achieve such high data rates of 400G for short-reach and metro applications [3]. Some methods employ low-order modulation formats and high symbol rates, such as a 110 GBd Polarization Division Multiplexing (PDM)-Quadrature

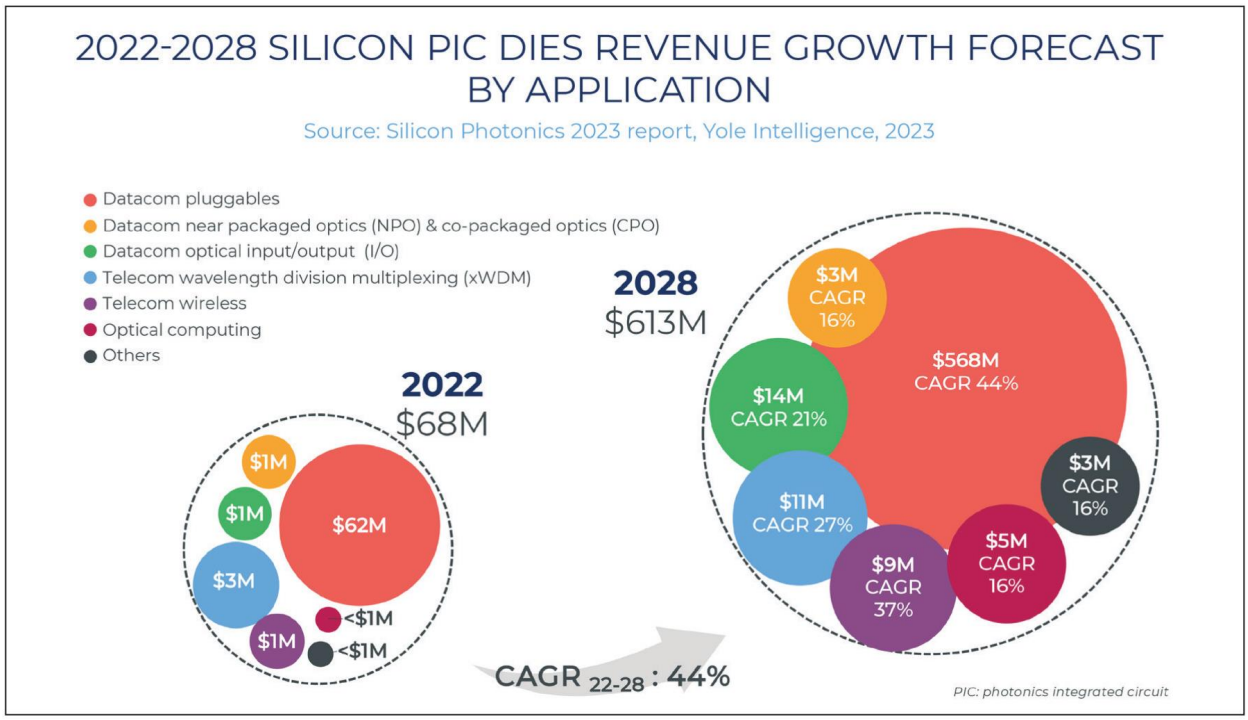

Fig. 1.1 The market value of silicon PICs according to [1].

Phase Shift Keying (QPSK) signal with a 100 GHz bandwidth [4]. Alternatively, other methods utilize higher-order modulation formats, such as 16Quadrature Amplitude Modulation (QAM) or 64QAM, with lower symbol rates [5, 6]. High-capacity signals featuring a high symbol rate and specific modulation format can potentially reduce the cost per bit by minimizing the number of devices and increasing fiber capacity. Electrical components in optical communication systems might limit the bandwidth, for example, Digital-to-Analog Converters (DACs) and Analog-to-Digital Converters (ADCs) must have a higher resolution to cope with the increasing symbol rates [7, 8]. The preferred solution is by incorporating Wavelength Division Multiplexing (WDM) [9–11]. WDM facilitates the simultaneous transmission of multiple optical signals with different wavelengths over a single fiber, thereby enhancing spectral efficiency and network capacity. As optical communication networks

evolve, there is a growing need for compact and highly efficient WDM transceivers capable of handling multi-Tb/s connectivity with ease [12, 13]. The emergence of Optical Frequency Combs (OFCs) stands out as a compelling solution for high-capacity WDM transmission systems.

In this context, OFC generators are promising sources for multi-wavelength transceivers as they can provide large numbers of optical carriers. One of the significant advantages of OFC generators is that their comb lines are equidistant in frequency, which eliminates the need for inter-channel guard bands. In WDM systems where arrays of independent laser sources are being used, precise control of each laser's frequency is required. These benefits are not limited to transmitters only; they are also applicable to receivers. On the receiver side, a single comb source can potentially replace an array of discrete Local Oscillators (LOs), which significantly simplifies the system architecture [14]. The use of chip-scale devices among the various comb generators is of particular interest due to their highly scalable photonic integrated circuits for modulation, multiplexing, routing, and reception of data signals. These devices could potentially become the key to compact and energy-efficient WDM transceivers that can be fabricated in large quantities at low cost while offering transmission capacities of tens of Tb/s.

The roadmap in Fig. 1.2 shows that PICs have been growing rapidly since 1992. The use of Quantum Dot/Dash (QD) and Quantum Well (QW) for monolithic integration appears to be the way forward for silicon photonics [15]. After roughly three decades of ongoing research, QD lasers have demonstrated intrinsic parameters that exceed the performance of OFC generators [16–18]. The QD gain medium exhibits a large tolerance to material defects, making it suitable for epitaxial integration of QD lasers on Silicon (Si) [19]. Its fast gain response makes it excellent for amplifying high-speed signals. Additionally, the QD gain medium's stability at high temperatures enables uncooled operation [20], while narrow linewidth lasers,

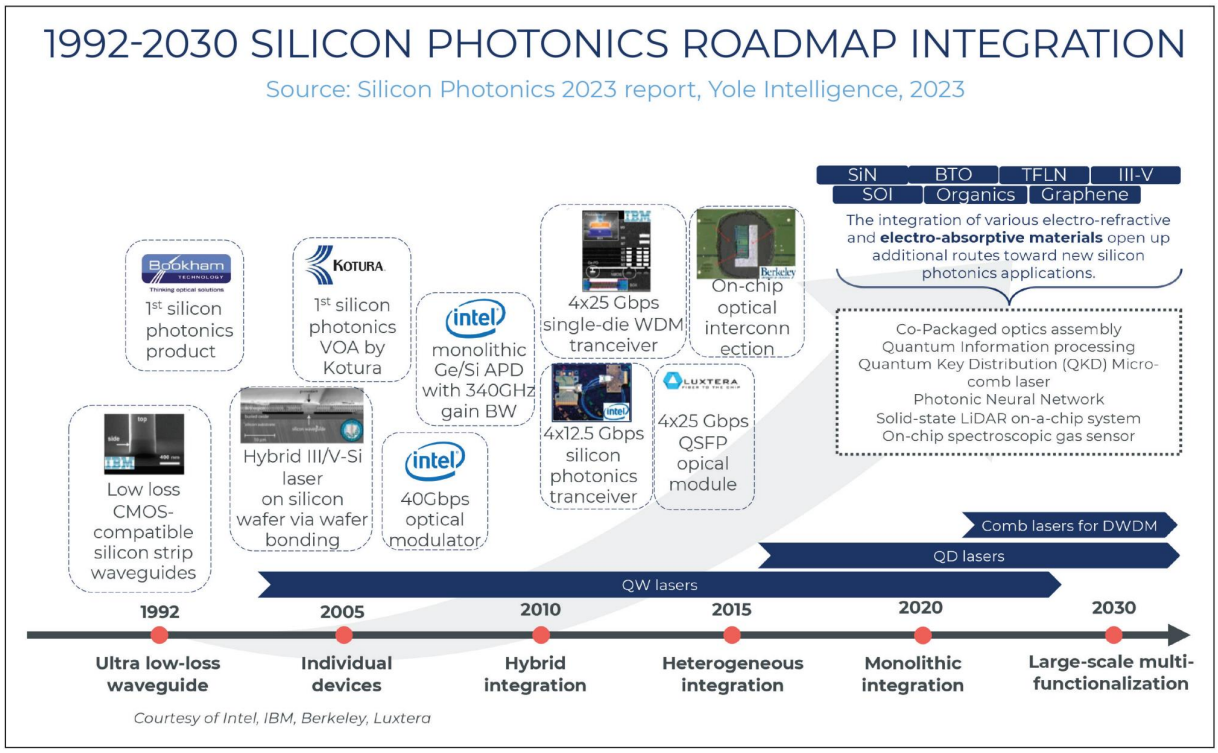

Fig. 1.2 Silicon photonics roadmap from 1992 to 2030 according to [1].

low threshold current density, internal loss, and confinement factor contribute to low noise figure operation [21]. Recent improvements in III-V-on-Si have pushed QD technology to the forefront of silicon photonics and a wide range of applications [22]. However, investigations are still going to enhance further this technology for high-performance PICs. The heterogeneous integration of QD lasers on Si has led to the generation of frequency combs with exceptional characteristics [19]. These combs exhibit sub-picosecond pulse duration, fairly narrow linewidth (in kHz range), and tens of terahertz optical bandwidth [23, 24].

Recently, extensive research has been going on to demonstrate the capabilities of Quantum Dash Mode-Locked Laser Diodes (QD-MLLDs) as multi-wavelength sources in optical communication systems [25–27]. Therefore, part of this thesis focuses on coherent optical communications that rely on QD-MLLDs for high throughput coherent WDM systems.

These versatile devices can act as both multi-wavelength light sources at the WDM transmitter and as multi-wavelength LOs for parallel coherent detection at the receiver. In fact, laser sources are just a part of future fully integrated coherent transmission modems. Moreover, In-phase and Quadrature (IQ) modulators are essential components in coherent systems and have been in development for years for future 800ZR [28]. Advances in Silicon Photonics (SiP) IQ modulators have been in progress, and many researchers demonstrated the potential of these modulators to support high-order modulation formats at high symbol rates [29, 30]. Thus, another part of this thesis focuses on the investigation of QD-MLLD with a SiP IQ modulator.

A fully integrated WDM coherent transmission system requires multiple filters, for example, to filter different channels or to reduce the Amplified Spontaneous Emission (ASE) noise. Bragg gratings are extensively used in optical communication systems for various applications such as dispersion compensation, gain equalization, and optical signal processing [31]. Recent developments in Bragg grating devices on the Silicon-on-Insulator (SOI) platform have demonstrated high-performance add-drop filters [32], high-Q resonators [33], and sampled Bragg gratings for tunable lasers and comb filters [34]. Therefore, we propose a fully reconfigurable Waveguide Bragg Grating (WBG) that not only can filter a single band but also can provide multiple-band filtering.

Indeed, the security of transferring data, more specifically over a long length of fiber, is a major concern as it is most likely to get stolen or hacked by eavesdroppers who can tap into the fiber channel and steal signals, which can lead to leakage of confidential information [35]. Therefore, it is crucial to ensure data confidentiality and secrecy during data transmission. In this regard, several encryption techniques have been investigated in optical fiber networks, such as optical chaos signal generation [36], optical steganography [37], and XOR encryption [38]. Quantum communication is widely considered a promising solution for secure

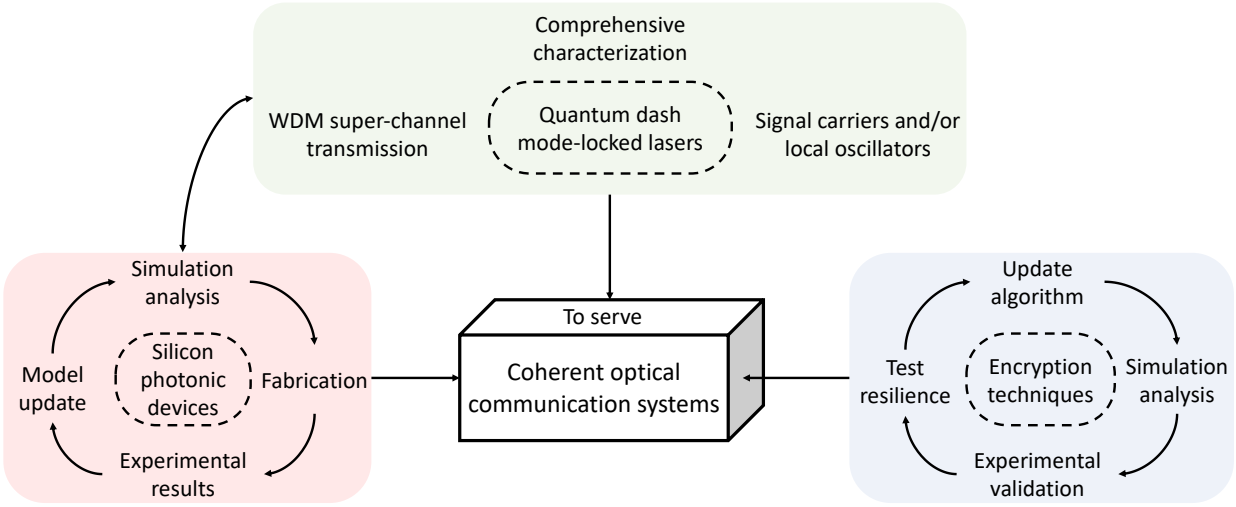

Fig. 1.3 Illustration of different topics explored in this thesis.

communications, offering provable security. One of the most popular methods of quantum encryption is called Quantum Key Distribution (QKD). QKD offers enhanced security by using the principles of quantum mechanics to distribute keys between authenticated parties. This method ensures that any attempts of eavesdropping are detected, making it a highly secure method of communications [39]. Therefore, we propose quantum-inspired encryption techniques to secure coherent optical fiber links over 80 km of Standard Single-Mode Fibers (SSMF) at high symbol rates up to 56 GBd utilizing high-order modulation formats, up to 32QAM.

The topics explored in this thesis are illustrated in Fig. 1.3. These topics fit together to serve optical communication systems for future coherent transceivers.

In the following section, state-of-the-art technologies are reviewed with attention given to WBGs on the SOI platform, and QD-MLLDs for high-capacity coherent transmissions.

1.2 State-of-the-art

1.2.1 Waveguide Bragg gratings

Since the early 2000s, WBGs on SOI platform have been explored thoroughly [40]. Such devices are made by etching periodic corrugations along the sidewalls of the waveguide, which creates a Bragg grating structure that can reflect and transmit light at specific wavelengths. The SOI platform is particularly well-suited for this type of waveguide because it provides a high-index-contrast waveguide that allows for efficient light confinement and low-loss propagation. WBG devices have been used for several applications ranging from filtering, sensing, and detection. Furthermore, they have been used to develop contra-directional couplers for coarse WDM applications [41, 42]. Other WBG structures have been developed to develop chirped WBGs that are useful to be employed in mode-locked lasers to generate ultra-short optical pulses [43]. The chirped structure helps in achieving broader bandwidths and shorter pulse durations, which is crucial in applications such as optical communications and precision sensing [44]. In addition, WBGs can be also used for evolving SiP modulators since they can be used to form micro-cavities [45].

One drawback of WBGs is their fixed response and limited tunability after fabrication. Fortunately, this limitation can be overcome by introducing an additional metal layer onto the Si waveguide. With proper adjustments of the heater voltage, we can modify the refractive index of the waveguide, thereby changing the device's response. More complex structures have been demonstrated by incorporating a PN junction on top of the waveguide [46, 47].

1.2.2 QD-MLLDs in coherent transmission systems

In recent years, several chip-scale comb generators have demonstrated their ability to facilitate high-speed WDM transmission at Tbit/s data rates. Among these, the so-called

Kerr microring resonator [48,49], utilizing the Kerr nonlinearities within optical waveguides, can generate hundreds of comb lines over a large bandwidth span of 10 THz or more, and are usable for data transmission [50, 51]. However, the associated comb spectra have few GHz comb spacing which might not be useful for WDM transmission. Another method for comb generation is by relying on gain switching of injection-locked Distributed Feedback (DFB) lasers. Although these can be integrated into chip-scale packages, they suffer from limited bandwidth, typically spanning less than 500 GHz [52,53]. Moreover, cascaded Mach-Zehnder modulatorss (MZMs) have been demonstrated over the years for frequency comb generation [54,55]; however, the setup requires Radio Frequency (RF) signal generators and additional RF amplifiers and is limited by the modulator bandwidth and the frequency of the RF signal generator [55]. QD-MLLDs overcome these limitations and offer a broadband comb lines spectrum requiring only a simple DC current [26,56].

QD-MLLDs have demonstrated excellent performance in terms of output power, wavelength coverage, and stability [57]. QD-MLLDs have been implemented with repetition rates ranging from 10 GHz [58] to exceeding 300 GHz [59]. For high-capacity data transmission experiments, the maximum achievable modulation format so far is 32QAM [60]. Researchers have made extensive efforts to push the boundaries of data transfer speeds using such comb sources to achieve data rates exceeding 10 Tb/s [61,62]. Various techniques also have been proposed to further reduce the linewidth of QD-MLLDs, such as external cavity and dual-loop optical feedback [63,64]. QD-MLLDs have not only been investigated for high-speed transmission in the C-band, but also in the O-band [65], and L-band [66–68].

1.3 Thesis objectives

To optimize and enhance the performance of optical communication systems, a comprehensive approach is essential, involving the refinement of various components such as lasers, modulators, filtering devices, electrical components, and Digital Signal Processing (DSP) units. The evolution of these devices requires multiple processes of simulations, fabrications, and testing before a final product reaches the market. Therefore, the primary objective of this thesis is to provide innovative and creative solutions to enhance capability of devices and performance of optical communications.

One of the objectives of this thesis is to address the growing demand for advanced photonic devices that can offer enhanced functionalities and performance in communication systems. Considering WDM systems, sometimes it is required to filter multiple bands. One of the most widely used integrated filters is the one based on WBGs. However, most of the reported WBGs are limited to filtering one channel at a time. The development of electrically tunable WBGs holds great potential for advancing the performance and adaptability of on-chip filtering technologies. Therefore, we aim to develop an electrically reconfigurable WBG that can filter multiple bands at the same time. Such filters can be used for applications in optical communications and microwave photonics. Another objective of this thesis is to assess the feasibility and efficiency of generating OFCs through on-chip cascaded modulators. This investigation focuses on exploring how cascading modulators can enable OFCs with precise control over the frequency spacing between the generated optical frequency channels.

Currently, coherent transceiver modems, such as Ciena's Wavelogic, operate with only a single laser source that can be tuned to a specific wavelength for data transmission. In that case, multiple laser sources are required to achieve WDM transmission. One alternative is to use a single comb source to replace the array of laser sources on the transmitter side. For

coherent detection, another comb source can also replace the array of laser sources used as LOs. Another objective of this thesis is to investigate the performance of a chip-scale comb source, i.e., QD-MLLD, in coherent transmission systems, and to see to what extent we can push these comb sources in terms of symbol rate and modulation formats. We also aim to investigate the frequency spacing between the comb lines to achieve higher symbol rates in WDM systems for data rates beyond Tb/s. Another purpose of this study is to see how well these comb sources perform with integrated modulators for future hybrid integration. Such complex systems need to be secured especially nowadays eavesdroppers can obtain a fiber-tapping tool and tap into the fiber to steal sensitive information. Another objective of this thesis is to investigate some encryption techniques that can be applied in the existing fiber links to secure data transmission.

1.4 Original contributions and thesis organization

This thesis is organized according to the main contributions. Chapter 1 provides a general introduction, and summarizes the motivation, objectives, and main contributions of this research. Chapter 2 then presents the fundamental background for this work, focusing on WBG, and coherent optical communications DSP.

- Chapter 3 demonstrates SiP devices, and our contributions are summarized as follows:
  - We propose a design for an electrically reconfigurable WBG on SOI platform. The tunability is based on an added layer of metal, thin film Titanium Nitride (TiN), that controls the refractive index of the waveguide. Thus, we can control the overall response. We showcase that different sections of the WBG structure can be heated to create multiple Bragg responses simultaneously.

  - The proposed electrically reconfigurable WBG not only provides control of the resonance wavelength but can also provide multi-band rejection filters and Fabry-Pérot (FP)-like filters. Such a device can be used in optical signal processing applications or to create chirped or phase-shifted grating structures.
  - We also investigate the possibility of generating OFC using 3 integrated and cascaded MZM on SOI platform.

- Chapter 4 demonstrates our assessment of the performance of QD-MLLD for the next generation of integrated coherent modems. The QD-MLLD emits a broadband spectrum of coherent frequency lines. The following summarizes our findings in detail.
  - We investigate each channel of the QD-MLLD, providing comprehensive device characterization to meet the requirements of future hybrid coherent modems with multi-wavelength chip-scale comb sources.
  - We demonstrate that the QD-MLLD can be used as either signal carriers or LOs in Dense Wavelength-Division Multiplexing (DWDM) systems. In our experiments, we showcase signal transmissions using high modulation formats, up to 64QAM, over 80 km of SSMF, achieving net data rates of up to 447.8 Gb/s per line. The WDM transmission experiments result in an aggregate data rate of 4 Tb/s using a single polarization configuration. Thus, there is a potential for doubling the net bit rates using a Dual-Polarization In-phase and Quadrature Modulator (DP-IQM).
  - We also provide a comprehensive comparison between the QD-MLLD and a narrow-linewidth Integrable Tunable Laser Assembly (ITLA), emphasizing their versatility as either signal carriers or LOs.

  - Additionally, we explore the use of QD-MLLD with a SiP modulator on-chip for coherent transmission over 80 km of SSMF. We achieve symbol rates up to 104 GBd using 16QAM modulation scheme. Our experimental results pave the way for a hybrid integration between QD-MLLD and silicon photonics. This integration holds promise for fully integrated WDM coherent modems, responding to the demands of long-haul and high-capacity optical communication systems.

- Safeguarding sensitive data during transmission in public fiber channels is imperative. In Chapter 5, we introduce quantum-inspired encryption techniques designed for implementation in existing fiber links.

  - The first method employs a roundtrip mechanism, eliminating the need for the authenticated transmitter to share any information about the secret key or codeword used for signal encryption. The encryption is performed at the transmitter using a Phase Modulator (PM). The codeword consists of a series of random phases applied to the signal, encrypting the symbols in the phase space. The encrypted signal is transmitted to another user, who loads the information signal and sends it back to the authenticated user.

  - We propose another encryption approach to serve one-way transmission systems. The encryption approach utilizes displacement operators on coherent states to displace the QAM symbols using random amplitudes and phases. The codeword in this case is more complex. A synchronization technique is required to correctly decrypt the received encrypted signal.

  - We further propose a dual-polarization encryption, where X and Y polarization symbols are encrypted using independent codewords. Attempting to decrypt Y-symbols with the codeword applied to X-polarization symbols makes the infor-

mation signal undetectable.

  - The efficacy of the proposed encryption techniques is examined through simulation and experimental validation in a dual-polarization coherent transmission system over 80 km of SSMF, using a symbol rate of 56 GBd and 4/16/32QAM modulation formats.

  - We also explore tapping attacks, wherein an eavesdropper attempts to steal data from the fiber link. Our findings demonstrate that, without access to the secret key, adversaries cannot extract any information from the stolen signal.

- Finally, the thesis is summarized in Chapter 6, where we also give the direction for future work and other research opportunities.

Chapter 2

Fundamental Background

In this chapter, we summarize the background necessary for better understanding of the experimental investigations presented in this thesis.

2.1 Waveguide Bragg gratings

A WBG is a wavelength-selective filter, constructed within a waveguide with a periodic grating structure. A schematic diagram of a uniform WBG is shown in Fig. 2.1. The input light propagates from the forward propagating mode to the backward propagating mode. The resulting reflection exhibits a band-pass response, while the transmission acts as a band-stop filter, with the central wavelength denoted as λ_B, the Bragg wavelength or the central wavelength of the filter. The Bragg wavelength, λ_B, is determined by the relationship

$$\lambda_B = 2n_{\text{eff}}\Lambda \tag{2.1}$$

where, n_{eff} represents the effective refractive index of the grating, and Λ is the grating period [69]. The bandwidth of the gratings can be expressed as

$$\Delta\lambda = \frac{\lambda_B^2 \kappa}{\pi n_g} \tag{2.2}$$

where, κ is the coupling coefficient of the grating, and n_g is the group index. The key parameters of the WBG play a crucial role in defining its spectral response. These parameters include the grating period Λ, the average width of the waveguide w_{avg}, corrugation width dW, and the number of grating periods N, together, they determine various aspects of the device's behavior. For example, the average waveguide width and corrugation width contribute to establishing the effective indices. When combined with the grating period, these indices set the Bragg wavelength λ_B. The corrugation width and the number of grating periods influence the filter's bandwidth and peak reflectivity. Thus, each of these parameters plays a specific role in shaping the overall spectral characteristics of the WBG.

Certainly, any SiP device requires thorough simulation before fabrication to optimize expected spectral responses. The Eigenmode Expansion (EME) solver in MODE (Ansys software) offers a rapid means to conduct parametric studies and comprehend the impacts of specific parameters. For example, we perform simulations to observe the effects of changing the waveguide's sidewall angle. In Fig. 2.2 (a) and (b), the results show the central wavelength as a function of the corrugation width and the filter bandwidth as a function of the corrugation width for a uniform WBG with two sidewall angles. It is worth noting that in many instances, the central wavelength and bandwidth of the grating provide sufficient information about its performance. To observe the full transmission spectrum of the simulated WBG, Finite-Difference Time-Domain (FDTD) method is a powerful way to perform it. However, it is not practical when it comes to simulating long structures due

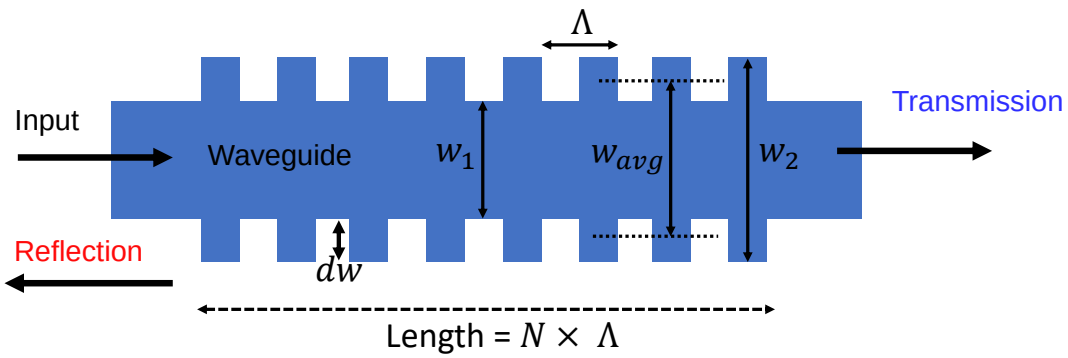

Fig. 2.1 Schematic diagram of a uniform WBG.

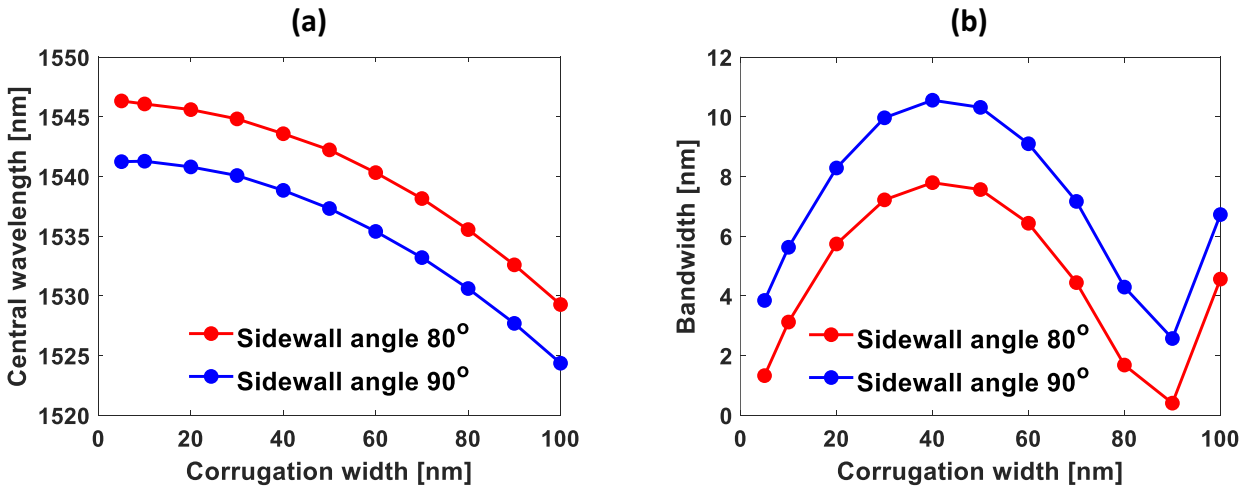

Fig. 2.2 EME optimization for two sidewall angles of a uniform WBG, (a) Central wavelength as a function of the corrugation width, and (b) filter bandwidth as a function of the corrugation width.

to the extended computational time. The Transfer-Matrix Method (TMM), described in detail in [70], provides a time-efficient and accurate transmission and reflection responses of a WBG.

We use the following steps with the TMM to study the WBG transmission and reflection responses

1. A WBG consists of a core waveguide with changing layers of higher and lower refractive

indices forming the grating. We extract these indices through MODE (Ansys software).

2. The transfer matrix, M_i, for a single grating period can be expressed as a 2×2 matrix. Each layer in the grating contributes to this matrix, and the product of these matrices for a complete grating period gives the overall transfer matrix for that period.

3. To calculate the overall transfer matrix for the entire WBG, the individual transfer matrices for each grating period are multiplied together. If there are N grating periods, the total transfer matrix T is given by $T = M_N \cdot M_{N-1} \cdot \ldots M_2 \cdot M_1$, where M_i is the transfer matrix for the i-th grating period

4. The elements of the final transfer matrix T provide information about the transmission and reflection coefficients of the entire WBG. The transmission coefficient T is given by the element in the (1,1) position of T, and the reflection coefficient R is given by the element in the (2,1) position.

The transmission and reflection coefficients can be related to the overall performance of the WBG, including the central wavelength, bandwidth, and peak reflectivity. A typical spectral response of a uniform WBG using the TMM is shown in Fig. 2.3. We extensively employed the TMM in our work in Chapter 3, and it demonstrated excellent agreement with our experimental results.

2.2 Coherent optical communications

A typical coherent optical communication system consists of three primary blocks, as depicted in Fig. 2.4. In the optical transmitter, the electrical signal from the information source is transformed into optical carrier frequencies (Electro-Optic (EO) conversion) through modulation. The modulated signals propagate through the optical fiber channel to the receiver.

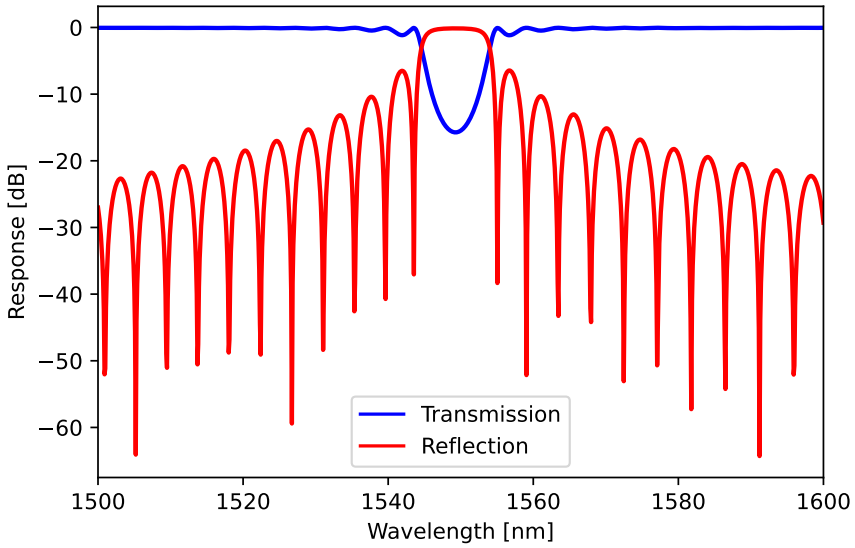

Fig. 2.3 Typical spectral response of a uniform Bragg grating simulated using the TMM.

Thanks to total internal reflection inside the optical fiber, the propagating signals are guided with low loss [71]. Optical fiber has a tremendous bandwidth, thus, it can handle a wide range of optical carriers or the so-called WDM system. In long-haul transmission, the fiber channel contains multiple optical amplifiers and repeaters. On the receiver side, optical signals are converted into the electric domain and address potential transmission impairments through compensation mechanisms.

Optical communication technologies can be classified as coherent or non-coherent based on their modulation and detection techniques. Non-coherent optical communications primarily use the modulated intensity of an optical carrier to transfer data over a channel. The associated receiver demodulates the detected intensity levels of the received signal to recover the transmitted data. This Intensity Modulation and Direct Detection (IM/DD) system has been used since the beginning of fiber-optic communications and is still frequently utilized for lines with a range of up to 10 km [72]. In this thesis, we use coherent transmission, thus,

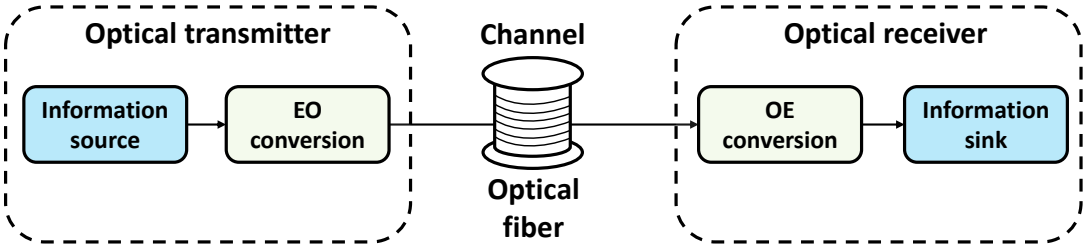

Fig. 2.4 Schematic diagram illustrating an optical communication system.

we provide a quick overview of some fundamentals of coherent communication systems.

2.2.1 Coherent transmitter

The electric field of an optical carrier wave that carries information in the amplitude and phase can be expressed as follows:

$$E_s(t) = A_s(t)\, e^{j(\omega_s t + \phi_s(t))} \tag{2.3}$$

where ω_s and $\phi_s(t)$ are the signal's carrier angular frequency and time-dependent phase variable, respectively, and $A_s(t)$ is the amplitude component of the signal. Data could also be modulated in the frequency and polarization. However, in this thesis, we focus on amplitude and phase modulation, and we use WDM and polarization multiplexing to obtain higher aggregate capacity. The optical field associated with the LO can be written as

$$E_{LO}(t) = A_{LO}(t)\, e^{j(\omega_{LO} t + \phi_{LO})} \tag{2.4}$$

where ω_{LO}, $A_{LO}(t)$ and ϕ_{LO} are the carrier frequency, amplitude and time-dependent phase variables of the LO, respectively.

Within the transmitter module, the initial step involves the mapping of an input bit

sequence onto a distinct constellation based on the chosen digital modulation format. Subsequently, the resultant symbol sequence undergoes pulse shaping. Following this, the electric analog signal modulates an optical carrier, which is then introduced into the optical fiber for transmission.

The EO conversion is accomplished through an optical modulator which modulates an optical carrier using an electric signal that carries the information to be transmitted. The modulation process is typically realized in one of two ways: direct modulation of a light source or the use of an external modulator. Direct modulation involves switching the optical source on and off (denoted as On-Off Keying (OOK) or Pulse Amplitude Modulation (PAM)) based on the information signal. While this operating principle makes direct modulation simple and cost-effective, the information cannot be modulated in the frequency or phase of the optical carrier [73]. On the other hand, external modulation involves the modulation of a continuously operated light source with the aid of an additional device. External modulators offer the advantage of modulating the information signal in the amplitude, phase, and frequency of the optical carrier.

Fig. 2.5 (a) and (b) show a typical schematic diagram of an IQ modulator and a transfer function of a MZM. The DP-IQM integrates a Polarization Beam Splitter (PBS) for splitting the input signal into two polarizations and a Polarization Beam Combiner (PBC) to combine both polarizations again at the output port. In a coherent transmission system, the inner MZMs, or the so-called child MZMs, are biased at the null point to modulate the phase, as shown in Fig. 2.5 (b). Modulation at null results in significantly lower optical signal power compared to IM/DD systems. This leads to the concept of modulation loss representing the difference between the maximum output power of the IQ modulator and the actual output power after loading the RF signal. Typically ranging from 8 to 10 dB, modulation loss compromises both signal linearity and output power.

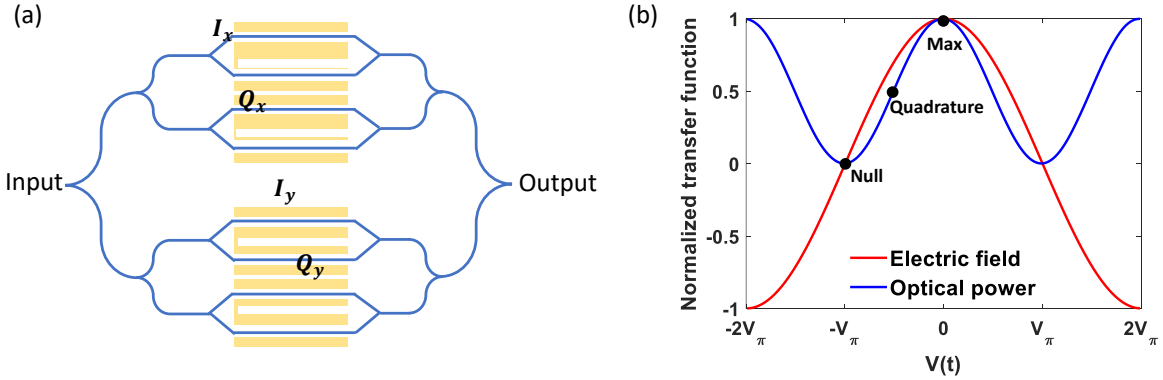

Fig. 2.5 (a) Schematic diagram of an IQ modulator. (b) Typical transfer function of a MZM.

2.2.2 Transmission impairments in optical fiber

Optical signals propagating inside optical fiber suffer from various impairments. These impairments include fiber loss, Chromatic Dispersion (CD), polarization mode dispersion, and nonlinear effects [74]. If optical amplifiers are employed in the system, another source of perturbation appears from the ASE noise. The theoretical mode of optical propagation can be determined through the nonlinear Schrödinger equation as follows [75]

$$\frac{\delta A}{\delta z} + \beta_1 \frac{\delta A}{\delta t} + j\frac{\beta_2}{2}\frac{\delta^2 A}{\delta t^2} - j\frac{\beta_3}{6}\frac{\delta^3 A}{\delta t^3} + \frac{\alpha(z)}{2}A = j\gamma|A|^2 A \tag{2.5}$$

where $A = A(z,t)$ is the optical field, $\alpha(z)$ is the fiber attenuation parameter, γ is the Kerr nonlinear coefficient, and β_n is the n-order frequency dependent chromatic dispersion parameters. These coefficients represent different impairments of the optical fiber.

The attenuation parameter $\alpha(z)$ represents the power attenuation of the optical signal as it propagates through the fiber channel and can be expressed as follows

$$\alpha_{[\mathrm{dB/km}]} = -\frac{10}{z}\log_{10}\left(\frac{P_{\mathrm{out}}}{P_{\mathrm{in}}}\right) \tag{2.6}$$

where z represents the fiber length, while P_{out} and P_{in} denote the output and input powers of the fiber channel, respectively. For a SSMF, the attenuation parameter α has a value of approximately 0.2 dB/km in the C and L bands [71]. Therefore, these bands prove to be suitable for long-haul transmission.

CD is a phenomenon where different wavelengths of light travel at different speeds through an optical fiber. This dispersion occurs because the refractive index is wavelength-dependent. As light pulses, which are often composed of multiple frequency components, propagate through the fiber, these various frequencies experience different degrees of slowing down or speeding up. Thus, the components of the light pulse spread out in time, arriving at the receiver at different moments. The consequence of CD is pulse broadening, where the originally narrow pulses become wider, potentially causing overlap with adjacent pulses. This broadening can limit the data transmission rate and quality of signals in optical communication systems. Various techniques, such as dispersion compensation methods or the use of dispersion-shifted fibers, are employed to manage or mitigate the effects of CD in optical communication systems.

The second order term β_2 in equation 2.5 corresponds to dispersion coefficient D, which is also known as Group Velocity Dispersion (GVD), and it can be expressed as follows

$$D = \frac{\delta\beta_1}{\delta\lambda} = \frac{-2\pi c\beta_2}{\lambda^2} \tag{2.7}$$

The dispersion parameter D is typically measured in units of ps/(km.nm). In a commercial SSMF, it typically falls within the range of 16-19 ps/(km.nm) in the C-band.

Another phenomenon that occurs in optical fiber channels is Polarization Mode Dispersion (PMD) where the different polarization states (X and Y) of light components within a pulse experience different propagation delays. This dispersion arises due to imperfections and

asymmetries in the optical fiber, causing variations in the velocities of orthogonal polarization modes [71]. PMD is a significant concern in high-speed optical communication systems, particularly for systems with long fiber lengths. It can limit the achievable data rates and increase the complexity of compensating for these dispersion effects. Various techniques, such as using polarization controllers or employing specialized fibers designed to minimize PMD, are employed to manage or mitigate the impact of polarization mode dispersion.

2.2.3 Coherent detection

There are several coherent detection schematics, for example, single coherent detection with single Photodiode (PD), single coherent detection with Balanced Photodiodes (BPDs), quadrature coherent detection with 90^o hybrid and dual-polarization coherent detection [76]. In this thesis, we focus on dual-polarization coherent detection as it is the general case and the one we used in our experiments. Dual polarization improves the spectral efficiency by doubling the capacity of transmission systems [77]. Fig. 2.6 shows a schematic diagram of a dual-polarization coherent detection system. Two 90^o hybrids, each equipped with four BPDs, are employed to detect the respective branches of orthogonally polarized received signals, $\overrightarrow{X}$ and $\overrightarrow{Y}$ polarizations. The received signal and LO are split into two orthogonally polarized branches using a PBS. The outputs from the two 90^o hybrids can be represented as follows:

$$\begin{bmatrix} E_1^+ \\ E_1^- \\ E_2^+ \\ E_2^- \end{bmatrix} = \begin{bmatrix} \overrightarrow{X}|E_s + E_{LO}|^2 \\ \overrightarrow{X}|E_s - E_{LO}|^2 \\ \overrightarrow{X}|E_s + jE_{LO}|^2 \\ \overrightarrow{X}|E_s - jE_{LO}|^2 \end{bmatrix} \tag{2.8}$$

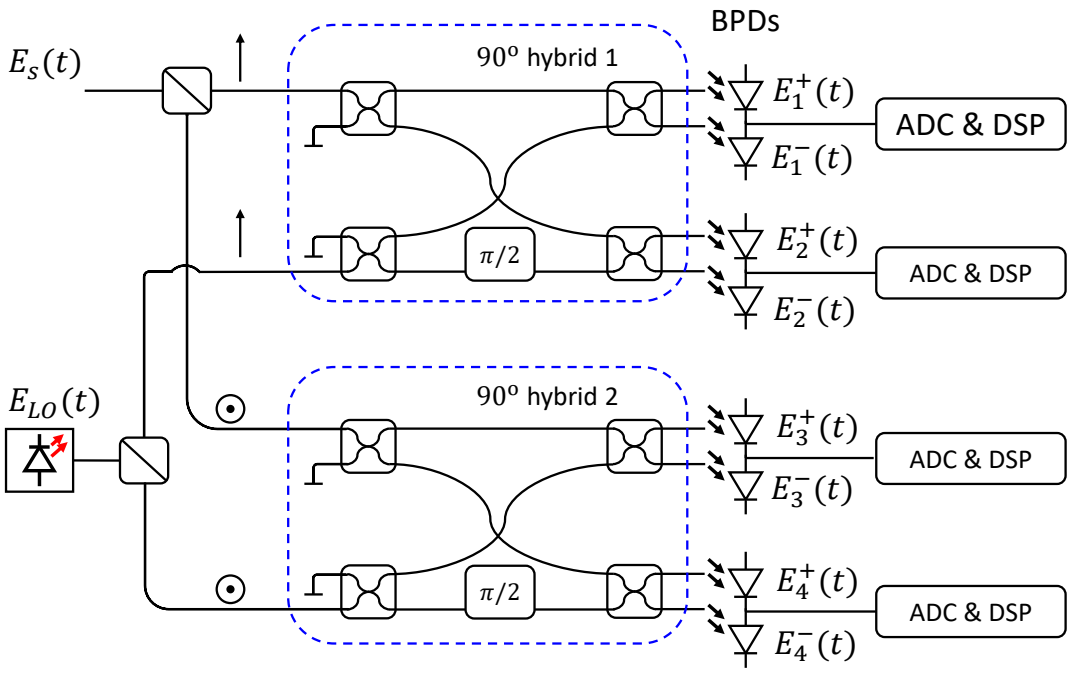

Fig. 2.6 Schematic diagram of a dual-polarization coherent detection with BPDs.

$$\begin{bmatrix} E_3^+ \\ E_3^- \\ E_4^+ \\ E_4^- \end{bmatrix} = \begin{bmatrix} \overrightarrow{X}|E_s + E_{LO}|^2 \\ \overrightarrow{X}|E_s - E_{LO}|^2 \\ \overrightarrow{X}|E_s + jE_{LO}|^2 \\ \overrightarrow{X}|E_s - jE_{LO}|^2 \end{bmatrix} \tag{2.9}$$

The IQ of polarization $\overrightarrow{X}$ and polarization $\overrightarrow{Y}$ are denoted as $E_{xI}(t)$, $E_{xQ}(t)$ and $E_{yI}(t)$, $E_{yQ}(t)$, and can be expressed as follows:

$$\begin{bmatrix} E_{xI}(t) \\ E_{xQ}(t) \end{bmatrix} = \begin{bmatrix} 2P_x(t)\cos(\Delta\omega t + \Delta\phi) \\ 2P_x(t)\sin(\Delta\omega t + \Delta\phi) \end{bmatrix} \tag{2.10}$$

$$\begin{bmatrix} E_{yI}(t) \\ E_{yQ}(t) \end{bmatrix} = \begin{bmatrix} 2P_y(t)\cos(\Delta\omega t + \Delta\phi) \\ 2P_y(t)\sin(\Delta\omega t + \Delta\phi) \end{bmatrix} \tag{2.11}$$

where $\Delta\omega$ is the intermediate frequency (also denoted to as $\omega_{IF} = \omega_s - \omega_{LO}$, the frequency difference between the signal carrier and LO) at which the photocurrent oscillates and $\Delta\phi$ is the phase different between the signal carrier and LO. The complex outputs from the BPDs are expressed as follows:

$$\begin{bmatrix} E_x(t) \\ E_y(t) \end{bmatrix} = \begin{bmatrix} 2P_x(t)\, e^{j(\Delta\omega t + \Delta\phi)} \\ 2P_y(t)\, e^{j(\Delta\omega t + \Delta\phi)} \end{bmatrix} \tag{2.12}$$

In general, coherent detection involves two techniques: homodyne detection and heterodyne detection [74]. Homodyne detection involves aligning the LO frequency with the signal carrier frequency, resulting in an intermediate frequency (ω_{IF}) of 0. This alignment significantly improves the Signal-to-Noise Ratio (SNR). However, a drawback of homodyne detection is the requirement for precise control of the LO phase during transmission. While the phase of the signal carrier and LO may fluctuate randomly over time, their phase difference ($\Delta\phi = \phi_s - \phi_{LO}$) can be maintained nearly constant through an optical phase-locked loop. Alternatively, heterodyne detection can be employed, where the LO frequency (ω_{LO}) differs from the signal carrier frequency (ω_s), resulting in an intermediate frequency (ω_{IF}) in the microwave region (approximately 1 GHz). Fast ADCs are then used to sample the IQ photocurrents, followed by DSP to extract the transmitted signal information [78]. In this thesis, we use the heterodyne detection technique.

2.2.4 DSP for coherent transmission over fiber channel

For the transmitter DSP, symbols are mapped into the desired modulation format, for example, QAM signaling. In M-QAM, each symbol represents a combination of M different amplitude levels. The most common QAM schemes include QPSK and 16QAM. A higher M allows for more bits to be transmitted per symbol, increasing the data rate. Each symbol corresponds to k bits, where $k = \log_2 M$ [79]. Increasing the modulation format order, M, is known to enhance the spectral efficiency of a system. However, this improvement comes at a cost—reducing the distance between symbols makes the system more sensitive to additive noise and phase perturbations. In high-order modulation schemes such as 16QAM and 64QAM, Gray encoding is desirable. The main characteristic of Gray mapping is that adjacent symbols have only a one-bit difference, as opposed to binary counting where consecutive symbols may have multiple-bit differences. This property is particularly advantageous in scenarios where a small error in symbol decoding is preferred over the possibility of decoding to a completely different symbol. The trade-off is that Gray mapping may sacrifice some level of data rate efficiency compared to straightforward binary mapping, but it improves robustness in the presence of noise.

After QAM mapping, pulse shaping is performed. In this thesis, we focus on Root Raised Cosine (RRC) pulse shaping technique. The frequency response of RRC filter can be expressed as follows [79]

$$G(f) = \begin{cases} T & \text{for } |f| \leq \frac{1-\alpha_{textroll-off}}{2T} \\ T\cos^2[\frac{\pi T}{2\alpha_{textroll-off}}(|f| - \frac{1-\alpha_{textroll-off}}{2T})] & \text{for } \frac{1-\alpha_{textroll-off}}{2T} < |f| < \frac{1+\alpha_{textroll-off}}{2T} \\ 0 & \text{for } \frac{1-\alpha_{textroll-off}}{2T} < |f| \end{cases} \tag{2.13}$$

where T is the symbol period, and $\alpha_{\text{roll-off}}$ is the roll-off factor. The RRC filter, when used individually, does not inherently meet the Nyquist criterion for Inter-Symbol Interference (ISI)-free transmission. The Nyquist criterion states that to avoid ISI, the pulse shape should have zero ISI at the sampling instances. However, when RRC filtering is applied at both the transmitter and the receiver, the combined response of these filters effectively satisfies the Nyquist criterion. This is due to the complementary roles of the transmitter and receiver filters in shaping the transmitted signal and compensating for any distortion introduced during transmission. In a communication system, the RRC filter at the transmitter serves to shape the pulse before transmission, and the RRC filter at the receiver helps to match the received signal to the original pulse shape. The combination of these filters ensures that the signal, when sampled at the receiver, does not suffer from ISI. This use of matched filtering, where the transmitter and receiver filters are matched to each other, helps in achieving reliable communication and mitigating the effects of ISI in the presence of channel impairments and noise.

For the receiver side, timing skew and quadrature error are the first impairments to be compensated. Timing skew occurs when there is a mismatch in the time at which the IQ components are sampled or processed. This misalignment can lead to distortion, symbol misinterpretation, and degradation in the performance of the communication system. Quadrature error refers to the phase mismatch between the IQ components of a signal. This error might occur due to imperfections in the 90^o optical hybrid. Luckily, these errors can be compensated by applying the Gram-Schmidt orthogonalization [80].

Then, we compensate for CD by directly multiplying the signal with the inverse of the CD transfer function in the frequency domain, and it can be expressed as follows [76, 81]

$$H(z,\omega) = e^{-j\frac{D\lambda^2}{4\pi c}\omega^2 z} \tag{2.14}$$

where ω is the angular frequency of the signal.

It is necessary to estimate and compensate for the Frequency Offset (FO) after CD compensation. Since the FO is independent of polarization, estimating it for a single polarization is sufficient. By increasing the received signal to the fourth power, we can estimate the FO frequency. The receiver input signal in the presence of phase and frequency offset is expressed as [82, 83]

$$r(k) = s(k)\, e^{j(\theta(k)+k\Delta\phi)} \tag{2.15}$$

where $s(k)$ is the transmitted signal, $\theta(k)$ is the phase noise, and $\Delta\phi$ is the phase offset between the instants k and $k+1$, given by

$$\Delta\phi = 2\pi\Delta f T_{sa} \tag{2.16}$$

where Δf is the difference between the signal frequency and LO frequency, and T_{sa} is the sampling time. As we mentioned earlier, the phases of the laser carrier and LO fluctuate over time, and that is why homodyne detection is not recommended.

Then, an adaptive Multiple-Input Multiple-Output (MIMO) equalizer is employed to compensate for ISI and PMD. The polarization multiplexed signal at the receiver side after fiber propagation can be presented as

$$\begin{bmatrix} E_x \\ E_y \end{bmatrix} = \begin{bmatrix} \sqrt{\alpha}e^{j\delta} & -\sqrt{1-\alpha} \\ \sqrt{1-\alpha} & \sqrt{\alpha}e^{-j\delta} \end{bmatrix} \begin{bmatrix} E_{in,x} \\ E_{in,y} \end{bmatrix} \tag{2.17}$$

where α and γ denote the power splitting ratio and phase difference between the X and Y polarizations. The received signal is combined with Jones matrix and can be expressed for

simplicity as follows [84]

$$\begin{bmatrix} E_{out,x} \\ E_{out,y} \end{bmatrix} = \begin{bmatrix} h_{xx} & h_{xy} \\ h_{yx} & h_{yy} \end{bmatrix} \begin{bmatrix} E_{in,x} \\ E_{in,y} \end{bmatrix} \tag{2.18}$$

where $E_{in,x}$ and $E_{in,y}$ represent the input complex-field signals, while h_{xx}, h_{xy}, h_{yx}, and h_{yy} denote the adaptive filters. The resulting equalized complex-field signals corresponding to the polarization multiplexed signals are denoted as $E_{out,x}$ and $E_{out,y}$. The filter coefficient can be found and optimized by the Least Mean Squares (LMS) algorithm. The goal of the LMS algorithm is to adjust the parameters of an adaptive filter iteratively so that the output of the filter closely matches a desired or target signal [85]. The LMS algorithm is computationally simple and well-suited for online or real-time applications. It is widely used for adaptive filtering tasks due to its simplicity and efficiency.

Then, carrier phase recovery algorithms are implemented to compensate for varying relative phases of the transmitter and LO lasers, due to their non-zero laser linewidth. One of the most commonly used algorithms is the Decision-Directed Phase-Locked Loop (DDPLL) [86] and Blind Phase Search (BPS) [87]. Briefly, a Phase Locked Loop (PLL) is a feedback control system designed to synchronize the phase of a LO with the phase of an incoming signal. In a DDPLL, the operation is "decision-directed," meaning it uses the decisions made on the received signal to help in tracking and adjusting the LO. The BPS algorithm estimates and synchronizes the phase of a received signal without relying on known pilot symbols or training sequences. This is particularly useful when the transmitted signal lacks explicit synchronization information, making it necessary to perform phase recovery blindly.

Finally, the symbols are demodulated with the right QAM order, and decisions are made to calculate the Bit Error Ratio (BER). In this thesis, we do not implement the Forward

Error Correction (FEC) decoder in the receiver, but we account for the FEC code overhead (OH) when calculating the net data rate.

The theoretical BER in a coherent detection system for QAM modulation schemes can be approximately expressed as follows [88]

$$\mathrm{BER} = \frac{2 \times 1.67}{\log_2(M)} \frac{\sqrt{M}-1}{\sqrt{M}} \operatorname{erfc}[\sqrt{\frac{3\gamma_b \log_2(M)}{2(M-1)}}] \tag{2.19}$$

where

$$\gamma_b = \frac{\mathrm{OSNR}}{B_e \cdot \log_2(M)} \tag{2.20}$$

where B_e is the symbol rate, and M is the QAM modulation order.

2.3 Mode-locking principles

Mode-locking in lasers is a technique that generates ultrashort pulses of light by ensuring that the modes (individual longitudinal modes or frequencies) of the laser oscillate in phase. In QD-MLLDs, the mode-locking process involves controlling the phase of the emitted combs in a way that facilitates the generation of these ultrashort pulses. The ultrashort pulses allow for the transmission of extremely high data rates. QD-MLLDs use semiconductor materials with a specific structure, often characterized by elongated nanostructures called quantum dashes. These quantum dashes have unique electronic and optical properties that make them suitable for laser applications. A numerical model of such lasers has been demonstrated in [89]. The electric field emitted by a laser with M odd modes with a frequency separation

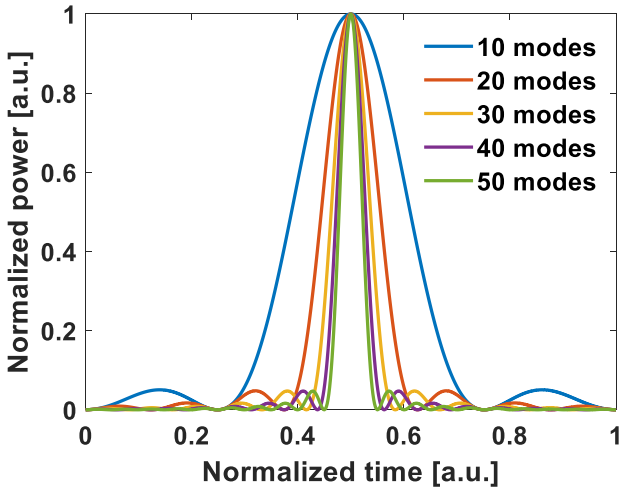

Fig. 2.7 Mode-locking principle.

$\Delta\omega$ can be expressed as follows [90]

$$E(t) = \sum_{n=-\frac{M-1}{2}}^{n=\frac{M-1}{2}} A_n(t)\, e^{j(\omega_o + n\Delta\omega)t + \phi_n(t)} \tag{2.21}$$

where $A_n(t)$ is the amplitude variation, ω_o is the frequency of the central mode, and $\phi_n(t)$ is the phase of the n-th mode. After some algebra and approximations, the total power equation can be expressed as follows

$$P(t) = \frac{\sin^2(\frac{M\Delta\omega t}{2})}{\sin^2(\frac{\Delta\omega t}{2})} \tag{2.22}$$

We plot equation 2.22 for various numbers of modes, and the simulated results are shown in Fig. 2.7. We observe that a large laser bandwidth or many modes are required for the generation of very short pulses.

2.4 Summary

Silicon photonics and coherent communications are continually advancing in technology over time. In this chapter, we have provided a brief overview of certain fundamentals used in this thesis. However, for more in-depth information on specific topics, we recommend the reader consult the corresponding references.

Chapter 3

Silicon Photonic Devices

Active silicon photonic devices refer to devices that incorporate active materials to control or modify the behavior of light in the optical domain. These devices are essential for realizing ultra-compact, low-power, and high-speed optical communication and computing systems. The most commonly used active materials in silicon photonics are III-V compound semiconductors, such as Indium Phosphide (InP) and Gallium Arsenide (GaAs), which are integrated with silicon-based waveguides to create hybrid platforms [91]. These platforms can be used for various applications, including optical amplification, modulation, detection, and switching. The active materials in these devices can be electrically or optically controlled, allowing for precise control over the optical signal. Overall, active silicon photonic devices are critical components in the development of advanced optical communication and computing systems.

In this chapter, we propose two different designs of electrically reconfigurable WBGs in SOI platform using a multiple-contact heater element. The first design has a uniform TiN heater element on top of the Silicon Dioxide (SiO_2), while the second design has a tilted heater

element. Six equidistant electrical pads are connected to the TiN heater element in the first design, allowing for the control of different segments of the gratings. We demonstrate that the proposed devices can be programmed to implement various filtering functions, including multi-band filters and FP-like filters. We present theoretical and experimental transmission responses of the proposed WBGs and perform thermal analysis using COMSOL Multiphysics to investigate the thermal distribution on the SiP chip. Furthermore, we investigate the mismatching between theoretical and experimental results to investigate the fabrication errors. In addition to the first design, we propose the second design of electrically reconfigurable WBG, which is based on a tilted heater structure. This structure creates some chirp by continuously changing the refractive index throughout the WBG structure. We demonstrate the feasibility of using this design to create chirped WBG, which are useful for dispersion compensation applications.

At the end of this chapter, we investigate the feasibility of an on-chip OFC generator based on three cascaded MZMs. We analyze the performance of the proposed device and show that only two cascaded MZMs can generate OFCs with low amplitude variations, high coherence and stability.

The work in this chapter is based on our publications in [92, 93].

3.1 Electrically reconfigurable waveguide Bragg grating filters

3.1.1 Overview

For the last three decades, the integration of silicon photonic devices on the SOI platform has attracted much attention thanks to its compatibility with the Complementary Metal-Oxide-Semiconductor (CMOS) process, low fabrication costs, and high fabrication yield [40, 94].

Photonic filtering devices are fundamental building blocks that exist in almost every photonics signal processing system due to their capability of providing a user-defined response based on the target application [95]. On-chip WBGs offer promising solutions to enable filtering capabilities and are especially appealing because of their simple operating principle [96]. The long-established limitation in conventional WBGs is that their spectral characteristics are fixed once the gratings are fabricated. Thus, to create multiple filter responses, special designs of multiple WBGs are required for a user-defined task. Recently, silicon-based WBGs have been proposed with tunable index modulation profiles. Achievements include tuning the center wavelength [97] or the amount of dispersion for chirped structures [44, 47, 98–100] or tuning resonance features [101], as in a phase-shifted structure [46].

Considering WDM systems, it may be required to filter multiple wavelengths at the same time [102]. Most of the reported electrically tunable WBGs are limited to filtering one wavelength at a time. The purpose of this work is to develop an electrically tunable WBG that can be used to create different spectral responses, such as multiple tunable reflection bands or a FP filter. Tunable multi-band filters can enable different processing functions in optical communications and microwave photonics. For example, a tunable multi-band filter, i.e., where the number of wavelength bands can be varied as well as the specific wavelengths of operation, can be used for reconfigurable optical add-drop multiplexing (of course, the spectral response needs to be optimized for this specific application). As a second example, FP-like filters with tunable Free Spectral Range (FSR) can be used for reconfigurable generation of chirped microwave waveforms based on spectral shaping and wavelength-to-time mapping (here the FP filter has a uniform FSR and needs to be combined with a dispersive medium providing a nonlinear wavelength-to-time mapping). FP filters can also be used for optical sensing and high precision measurements.

3.1.2 Operating principles

Fig. 3.1 (a) and (b) illustrate the schematic diagram and side view of the proposed reconfigurable WBG in SOI platform. The grating is uniform and incorporates an independent heater element located 2 μm above the waveguide. The heater element is made of TiN; its thickness is 120 nm, and it is 2.5 μm wide. There are six electrical pads distributed in an equidistant manner along the length of the grating; the separation between each electrical pad is 50 μm. The WBG is designed such that the average width of the waveguide is 500 nm, and the height is 220 nm to satisfy the single TE mode criteria. To maintain a transmission response in the C-band, we set the grating period, λ, to 318 nm, the number of grating periods, N, to 787, and the corrugation width, dW, to 50 nm. The total length of the grating is $N \times \lambda \approx 250\,\mu$m. The device was fabricated via a multi-project wafer run at the Advanced Micro Foundry (AMF) in a CMOS-compatible process using 193 nm ultraviolet (UV) lithography. Fig. 3.1 (c) shows the measured transmission response of the proposed WBG: the 3 dB bandwidth is 9 nm and the extinction at the Bragg wavelength is 30 dB corresponding to a peak reflectivity $> 99.9\%$. Fig. 3.1 (d) shows the chip under test with a DC probe connected to the electrical pads, and a Fiber Array Unit (FAU) coupled into the Vertical Grating Couplers (VGCs) for input and output coupling. Fig. 3.1 (e) shows a microscopic image of the proposed device.

Fig. 3.2 shows examples of how reconfiguration is achieved. An applied voltage on one segment of the grating creates a localized thermal change which, in turn, changes the effective refractive index and hence corresponding Bragg wavelength. In other words, by applying a bias voltage to a pair of electrical pads, the refractive index of the corresponding grating segment can be tuned thanks to the large thermo-optic coefficient of silicon. The thermal

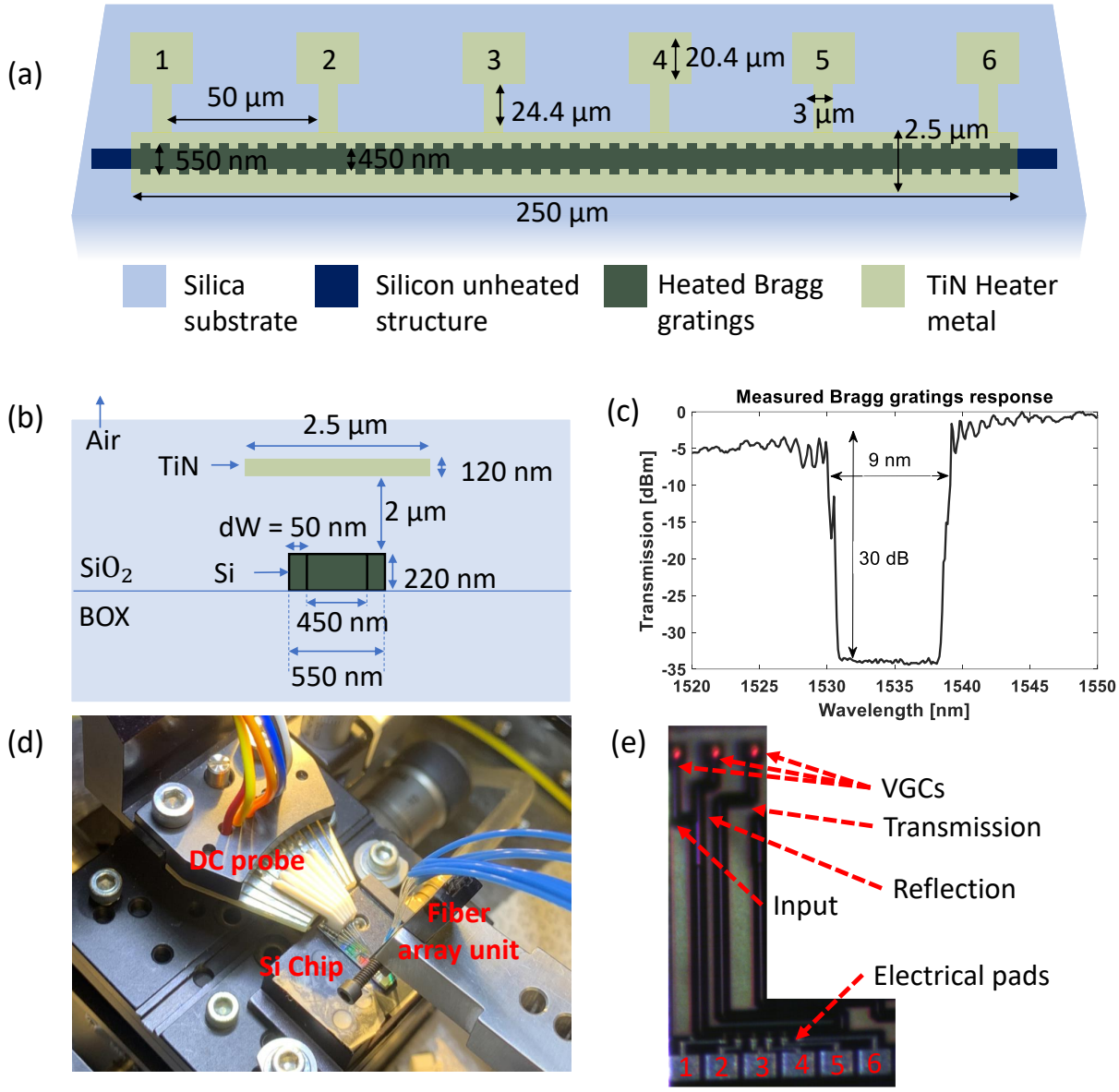

Fig. 3.1 (a-b) Schematic diagram and side view of the proposed device. (c) Measured transmission response of the proposed WBG without any applied voltage. (d) Picture of the chip under test. (e) Microscopic image of the device.

tuning coefficient can be expressed through the following [69]:

$$\frac{d\lambda}{dT} = \frac{\lambda}{n_g} \frac{dn_{\text{eff}}}{dT} \tag{3.1}$$

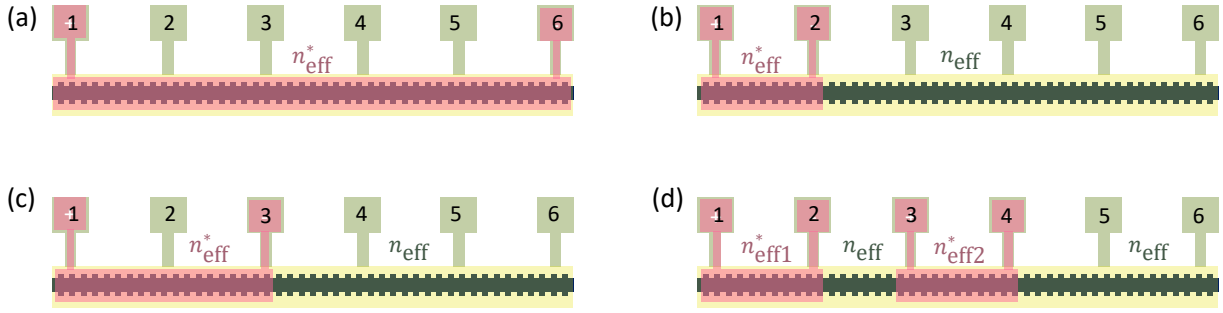

Fig. 3.2 Schematic diagrams to illustrate how reconfiguration (modes of operations) are performed. Applying voltage (heat) on particular segments creates a localized thermal change which in turn changes the effective refractive index and hence corresponding Bragg wavelength.

where T is the temperature, λ is the operating wavelength, and n_g is the group index. The thermo-optic coefficient in silicon is $\frac{dn}{dT} = (1.86 \pm 0.08) \times 10^{-4}$ K [69]. Thus, the entire index profile of the grating can be electrically reconfigured by applying voltages to multiple pairs, and with different voltages, creating a wide range of temperature distributions and hence, the possibility to obtain diverse spectral characteristics. We simulated the device using the COMSOL Multiphysics software to investigate the thermal distribution on the surface of the WBG, a snapshot is shown in Fig. 3.3. The COMSOL simulation incorporates the TiN electric heaters, Si waveguide, and a sufficiently large SiO_2 cladding layer. COMSOL simulates electromagnetic heating (resistive heating) by solving the heat equation assuming the electric current as a heat source, which requires coupling the electric current simulation and the heat transfer simulation. In electric current simulations, we apply the voltage difference directly to the desired electrical pads, whereas the rest of the metal and SiO_2 boundaries are electrically insulated, i.e., no reflections from boundaries. For the heat transfer simulations, we set the background ambient temperature of the SiO_2 cladding layer to room temperature 293.15 K. The coupling between the electric current and heat transfer modules simulates the increases in TiN, Si, and SiO_2 temperatures based on their respective thermal conduc-

tivities and heat capacities at the different electric currents. Table 3.1.2 shows the material properties used in the simulation and the thickness of each layer according to the fabrication process standards. The simulation procedure can be summarized as follows:

1. Define and optimize relevant material thermal properties
2. Using the COMSOL thermal model in steady-state and mesh-locked, we sweep the voltage applied to different electrical pads
3. Record the temperature profile along the WBG structure
4. We map that into the changes in the refractive index profile to recalculate the effective indices for each sweep
5. we use these effective refractive indices in determining the necessary parameters to simulate the WBG response using the TMM [69]

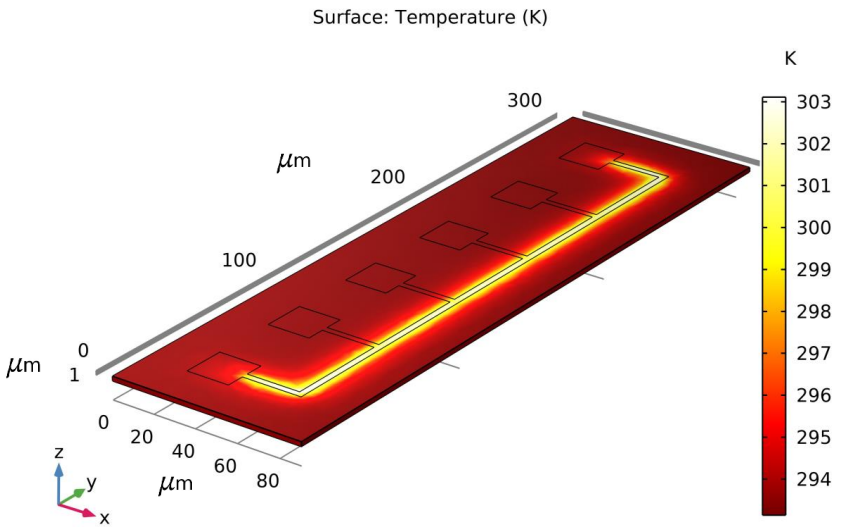

Fig. 3.3 Snapshot from COMSOL Multiphysics simulation when a 5 V is applied on electrical pads 1 and 6.

Material	Thickness [nm]	Density [kg/mˆ3]	Specific heat [J/kg.K]	Thermal conductivity [W/m.K]	Electrical conductivity [S/m]
Si	220	2330	711	148	4.3×10^{-4} [103]
SiO_2	2000	2203	709	1.4	1×10^{-11}
TiN	120	5240 [104]	598 [105]	28 [104]	2.3×10^{6} [106]

Table 3.1 Thermal and electromagnetic properties of materials used in COMSOL Multiphysics simulations.

Fig. 3.4 shows the simulated thermal distribution for different cases when voltage is applied on a pair (or multiple pairs) of electrical pads (the temperatures shown correspond to those on the surface of the waveguide though we have confirmed that there is negligible temperature difference between the surface and core of the waveguide).

For example, in Figs. 3.2 (a) and 3.4 (a), voltage is applied over the whole structure, namely, between electrical pads 1 and 6, in that case, perturbations in the refractive index happen along the whole structure, thus, shifting the response of the WBG to the longer wavelengths (see further, Fig. 3.5). In Figs. 3.2 (b,c) and 3.4 (b,c), when voltage is applied between electrical pads 1 and 2, the temperature (refractive index) of this particular segment is changed, giving rise to two separate Bragg responses. As another example, in Figs. 3.2 (d) and 3.4 (e), when two voltage sources are used to tune two different segments, namely, between electrical pads 1 and 2, and another between electrical pads 3 and 4, three cascaded WBGs at different wavelengths can be implemented (see further, Fig. 3.6). In Fig. 3.4 (f), when two independent voltage sources are used to manipulate the refractive indices of the first and last segments, a FP-like filter can be obtained. Thus, the spectral characteristics of the proposed WBG can be reconfigured according to the specifications of a given application, such as multiple band filters, or FP-like filters. Note that the heater element block extends from pads 1 to 6 and sometimes, depending on which pads are active, there is thermal

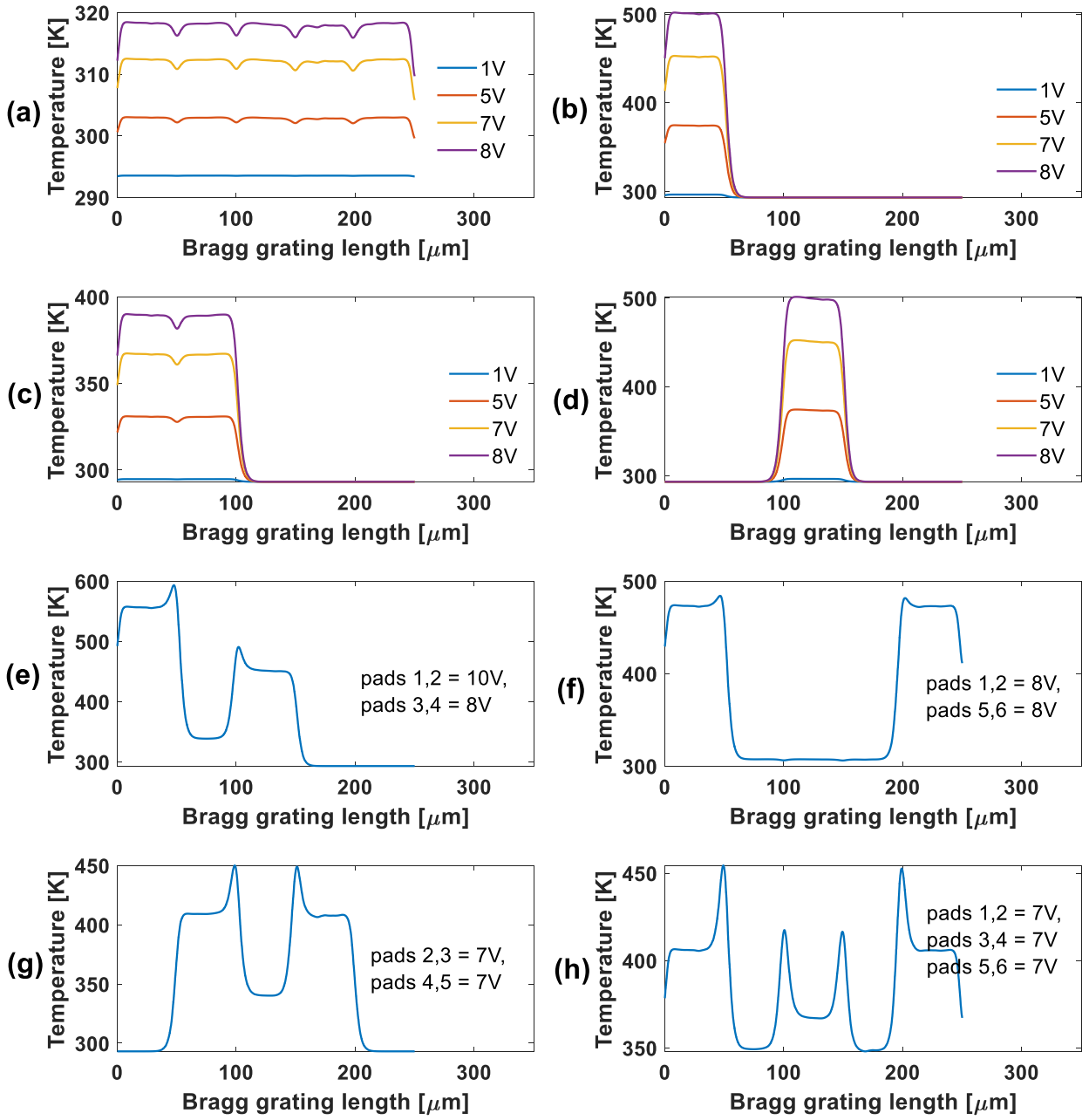

Fig. 3.4 Simulated thermal distribution on the WBG structure using COMSOL Multiphsyics. Voltage applied to electrical pads (a) 1,6, (b) 1,2, (c) 1,3 (d) 3,4 (e) 1,2 and 3,4 (f) 1,2 and 5,6, (g) 2,3 and 4,5 and (h) 1,2, 3,4 and 5,6. See numbers mapping in Fig. 3.1 (a).

crosstalk or leakage which can increase/decrease the temperature in regions where no voltage is applied. We notice that these dips or peaks have a limited impact on the spectral response.

3.1.3 Experimental results

Fig. 3.5 shows the measured and corresponding simulated transmission spectra of the reconfigurable WBG filter for different applied voltages and heat distributions. Excluding the VGCs loss, the WBG insertion loss is ~ 5 dB. In Fig. 3.5 (a), a clear redshift of the transmission response of the WBG can be observed when a variable voltage is applied over the whole structure. The total shift is around 2 nm, and the filter bandwidth is 9 nm.

In Fig. 3.5 (b), when a variable voltage is applied between electrical pads 1 and 2 (refer to Fig. 3.1 (a) for numbers mapping), two Bragg responses can be observed. One response is associated with the grating portion that is heated and the other from the unheated portion. The segment that is heated between electrical pads 1 and 2 is only 50 μm, which is four times shorter than the unheated segment; as such, while it results in a longer spectral response, it is also weaker (the peak reflectivity of the shorter grating is about half that of the unheated segment). In Fig. 3.5 (c), we apply a voltage between electrical pads 1 and 3 which increases the length of the thermally tuned segment to 100 μm. In this case, the two resulting spectral responses for an applied voltage of 8 V have approximately the same peak reflectivity. In Fig. 3.5 (d), we apply a voltage between electrical pads 3 and 4; the corresponding heated segment shifts to longer wavelengths with increasing voltage, and we also observe an FP cavity formed in the unheated grating segments between pads 1 and 3, as well as 4 and 6. The measured FSR of the formed FP is around 3.6 nm, whereas the simulated value is 4.5 nm. We discuss the fabrication errors later in section 3.3.

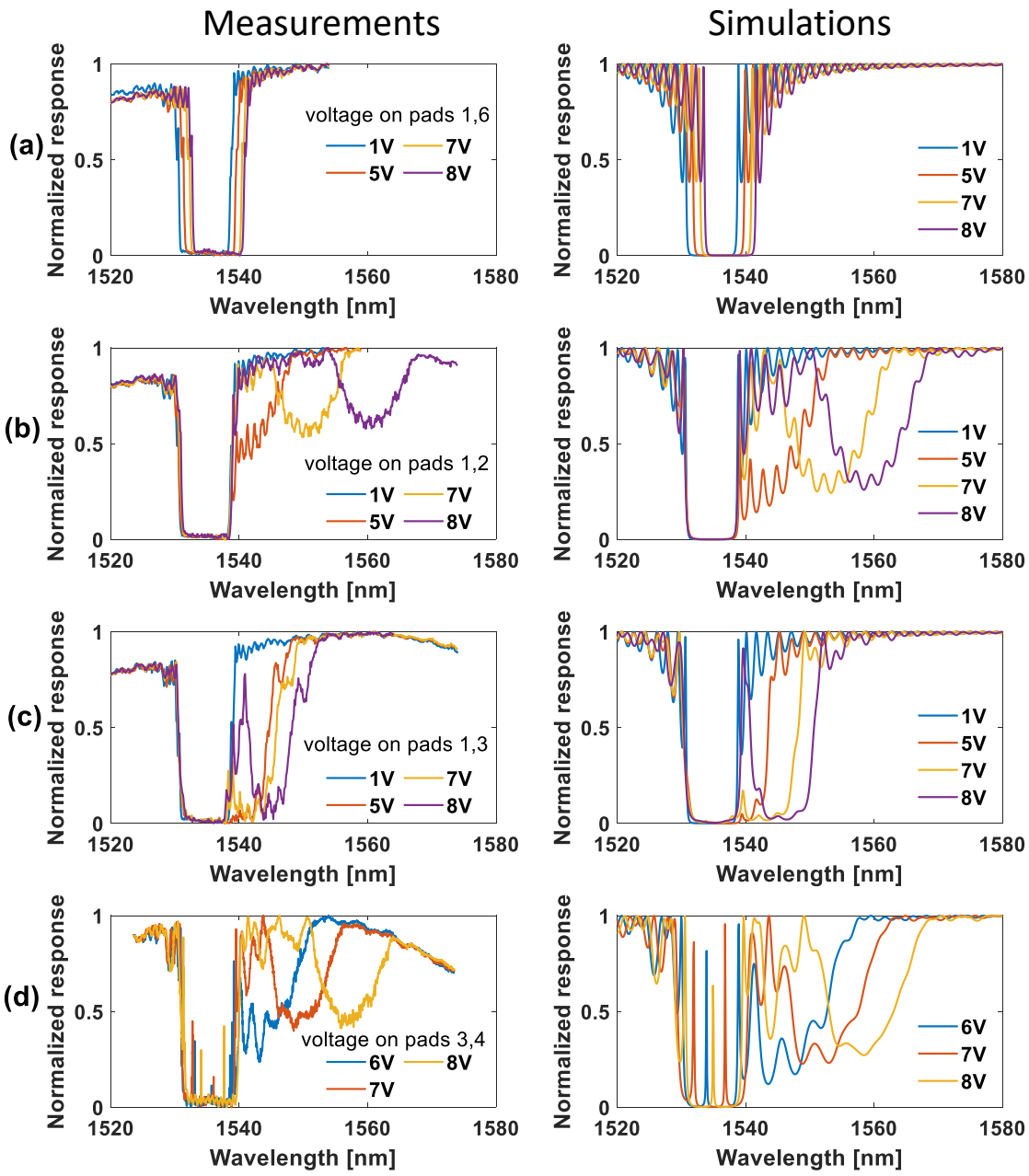

Fig. 3.5 Measured (left) and simulated (right) WBGs transmission responses with 0.01 nm resolution for voltages applied to different combinations of pads. Voltage(s) are applied between pads (a) 1 and 6. (b) 1 and 2. (c) 1 and 3. (d) 3 and 4.

Next, we investigate the spectral characteristics of the WBG when multiple voltages are applied to tune the refractive indices of multiple segments simultaneously. In Fig. 3.6 (a), the corresponding heat distribution considered is shown in Fig. 3.4 (e): two voltages are applied, one between electrical pads 1 and 2 and another between pads 3 and 4. In this case, three WBG responses can be observed. Since the two segments have the same length (50 μm), their responses will be similar. Thus, we apply a larger voltage (10 V) to one of the segments (between pads 1 and 2) so that its response experiences a greater red-shift and can be distinguished from that of the second segment, where the applied voltage is 8 V. In addition to the responses from the two thermally tuned segments, we have a third response corresponding to the remaining part of the grating that is not subjected to heating. The section between pads 2 and 3 is not heated, but there is some thermal leakage, as seen in Fig. 3.4 (e). The section between pads 4 to 6 is not heated at all. So, overall, there is a slight temperature difference, leading to a corresponding variance in the effective index between these sections. This causes a weak FP effect. It is worth noting that the 'mirror' created by the grating between pads 2 and 3 is shorter, resulting in lower reflectivity and broader bandwidth. In contrast, the mirror between pads 4 and 6 is longer, leading to higher reflectivity and a narrower bandwidth. The wavelength response of the grating between pads 2 and 3 is expected to be red-shifted a bit as well. All of this can introduce irregularities in the observed response.

In Fig. 3.6 (b), the corresponding heat distribution considered is shown in Fig. 3.4 (f), we investigate further the formation of an FP cavity by applying the same voltage to two segments, one at the beginning of the grating (between pads 1 and 2) and the second at the end of the grating (between pads 5 and 6). In this case, the two segments at the beginning and end of the structure form an FP cavity. The resonances are clear and the measured FSR

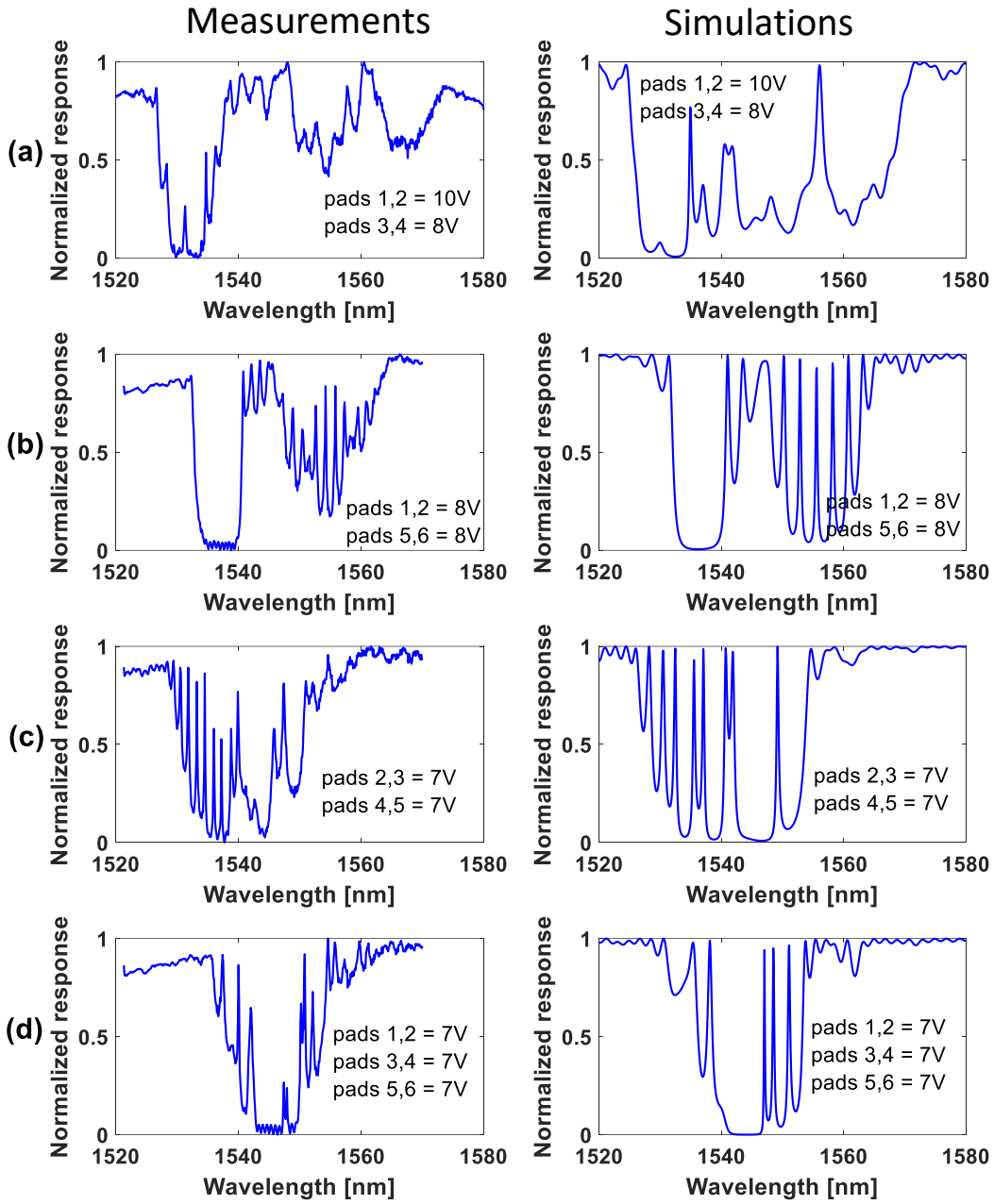

Fig. 3.6 Measured (left) and simulated (right) WBGs transmission responses with 0.01 nm resolution for two independent voltages applied to different combinations of pads. Voltage(s) are applied between pads (a) 1 and 2, another between 3 and 4. (b) 1 and 2, another between 5 and 6. (c) 2 and 3, another between 4 and 5. (d) 1 and 2, another between 3 and 4, another between 5 and 6.

is $\sim$ 1.6 nm, which agrees with the simulation results as well as the theoretical expression for the FSR for an FP cavity as derived in [107], which can be expressed as follow

$$\Delta\lambda = \frac{\lambda^2}{2n_{\text{eff}}(L_0 + L_{\text{eff1}} + L_{\text{eff2}})} \tag{3.2}$$

where, λ is the free-space wavelength, n_{eff} is the effective refractive index of the side Bragg segments, L_0 is the Bragg cavity length, i.e., the segment in the middle, and $L_{\text{eff1,2}}$ are the effective lengths of the side Bragg segments, and they are defined as

$$L_{\text{eff1,2}} = \frac{c\,\tau_{1,2}}{2n_{\text{eff}}} \tag{3.3}$$

where, c is the speed of light in vacuum, and $\tau_{1,2}$ are the group delays of the side Bragg segments. Using the thermal distribution values and the TMM technique, we simulated the group delay for this case, and it was found to be around 1.3 ps. The effective refractive index calculations are done in Lumerical (Ansys) software. Note that in this case, $L_{\text{eff1,2}}$ are identical. Thus, the theoretical FSR value can be calculated as follows

$$\Delta\lambda = \frac{(1550 \times 10^{-9})^2}{2 \times 2.405(150 \times 10^{-6} + \frac{2\times3\times10^8\times1.3\times10^{-12}}{2\times2.405})} \cong 1.6nm \tag{3.4}$$

Fig. 3.6 (c-d) illustrates the capability of the proposed device to create different FP-like cavities. In all cases, the simulated responses show an excellent agreement with the measured responses. Note that the effective refractive indices and the corrugation width of the WBG were adjusted to account for variations/errors in fabrication and processing to match the simulated and measured responses.

3.2 Tilted heater structure for a chirped WBG

Figure 3.7 (a) presents the schematic diagram of the proposed WBG featuring a tilted heater structure. The operating principle is similar to what we discussed earlier. The primary objective of this device is to systematically adjust the refractive index of the WBG structure, creating a form of chirped WBGs. An example of chirped WBG is the variation of waveguide width along the WBG structure, as reported in [47, 108].

In our proposed design, the lateral distance between the heater and the waveguide varies across the WBG structure. Thus, after uniformly heating the entire WBG (achieved by applying voltage to electrical pads 1 and 6), a gradual change in the refractive index occurs. According to the schematic diagram in Figure 3.7 (a), launching light into the WBG from the right side results in an increasing refractive index as it propagates through the grating, yielding an effective red chirp. On the contrary, light coupled in from the left side experiences a decreasing refractive index with propagation, leading to an effective blue chirp. The group delay values generated from such a chirp depend on many factors such as grating length, coupling coefficient, and thermal distribution.

Figure 3.7 (b) illustrates the temperature distribution at the midpoint on the surface of the gratings, plotted against the lateral displacement. As observed, the temperature on the surface of the gratings returns to the ambient temperature after an approximate lateral displacement of 9 μm of the heater element. We COMSOL thermal simulation to investigate the thermal distribution along the WBG structure with the influence of the tilted heater structure. Fig. 3.8 shows the simulated thermal distributions for the maximum voltage applicable to the electrical pads. As observed, the heat distribution is not as intense as in the case of a uniform heater structure. It is worth mentioning that we received multiple copies

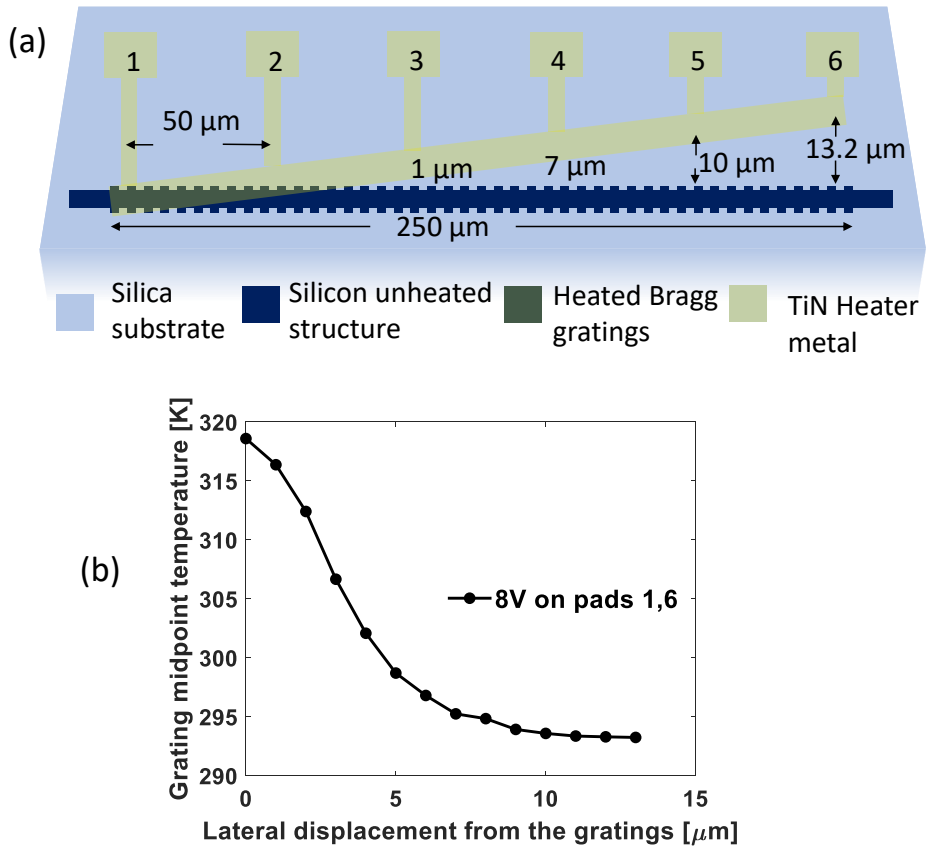

Fig. 3.7 (a) Schematic diagram of the proposed WBG with tilted heater structure. (b) The temperature at a middle point on the surface of the grating as a function of the lateral displacement of the heater element when 8 volts are applied between pads 1 and 6.

of the chip and one of them was sacrificed to assess the voltage tolerance of the electrical pads. Our findings indicate that the maximum voltage tolerated falls between 10 V.

3.2.1 Experimental results

To examine the performance of the tilted heater structure device, we employ the same methodology. In Figure 3.9 (a), we apply a variable voltage between electrical pads 1 and 6. As expected, the red-shift effect is less pronounced compared to the uniform heater structure,

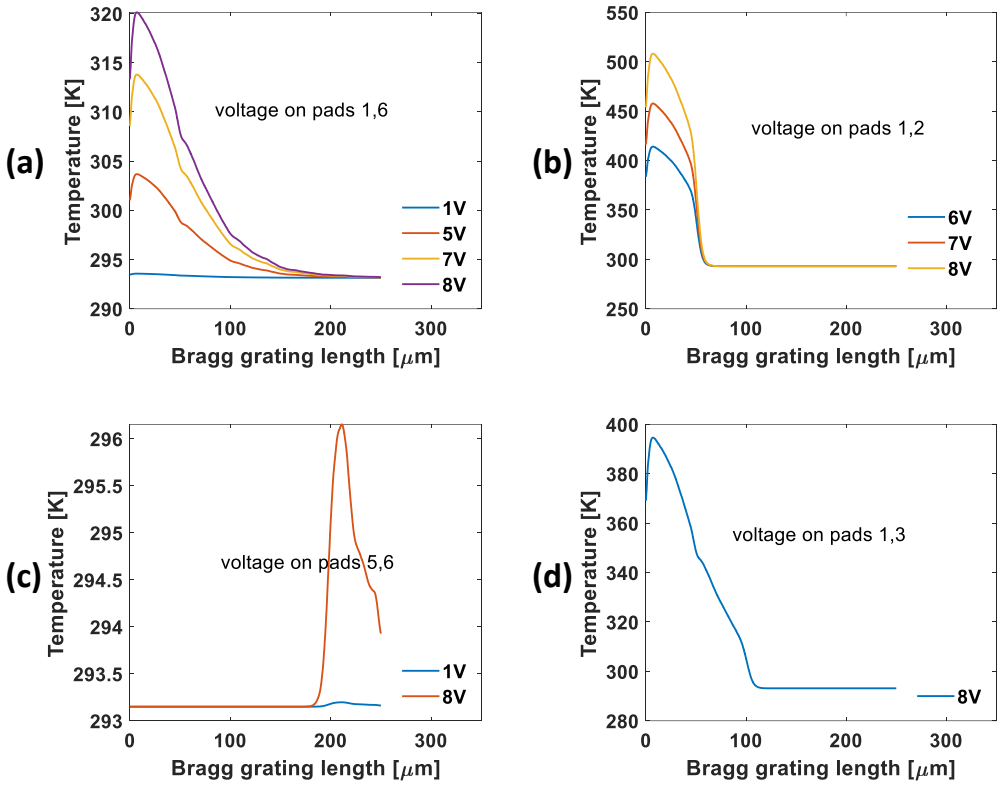

Fig. 3.8 Simulated thermal distribution on the WBG with a tilted heater structure using COMSOL Multiphsyics. Voltage applied to electrical pads (a) 1,6, (b) 1,2, (c) 5,6 (d) 1,3. See numbers mapping in Fig. 3.7 (a).

indicating a weaker response. Figure 3.9 (b) presents the response when voltage is applied specifically to electrical pads 1 and 2. The shorter Bragg gratings exhibit a weaker response compared to the uniform heater structure. In Figure 3.9 (c), applying voltage to electrical pads 5 and 6 results in a minimal thermo-optic effect, barely altering the original Bragg response.

Further investigation in Figure 3.9 (d), where voltage is applied to pads 1 and 3, yields similar findings. Once again, the simulation results align excellently with the measured results. These observations emphasize the nuanced impact of the tilted heater structure on the device's response to varying voltage configurations. The comparative analysis provides

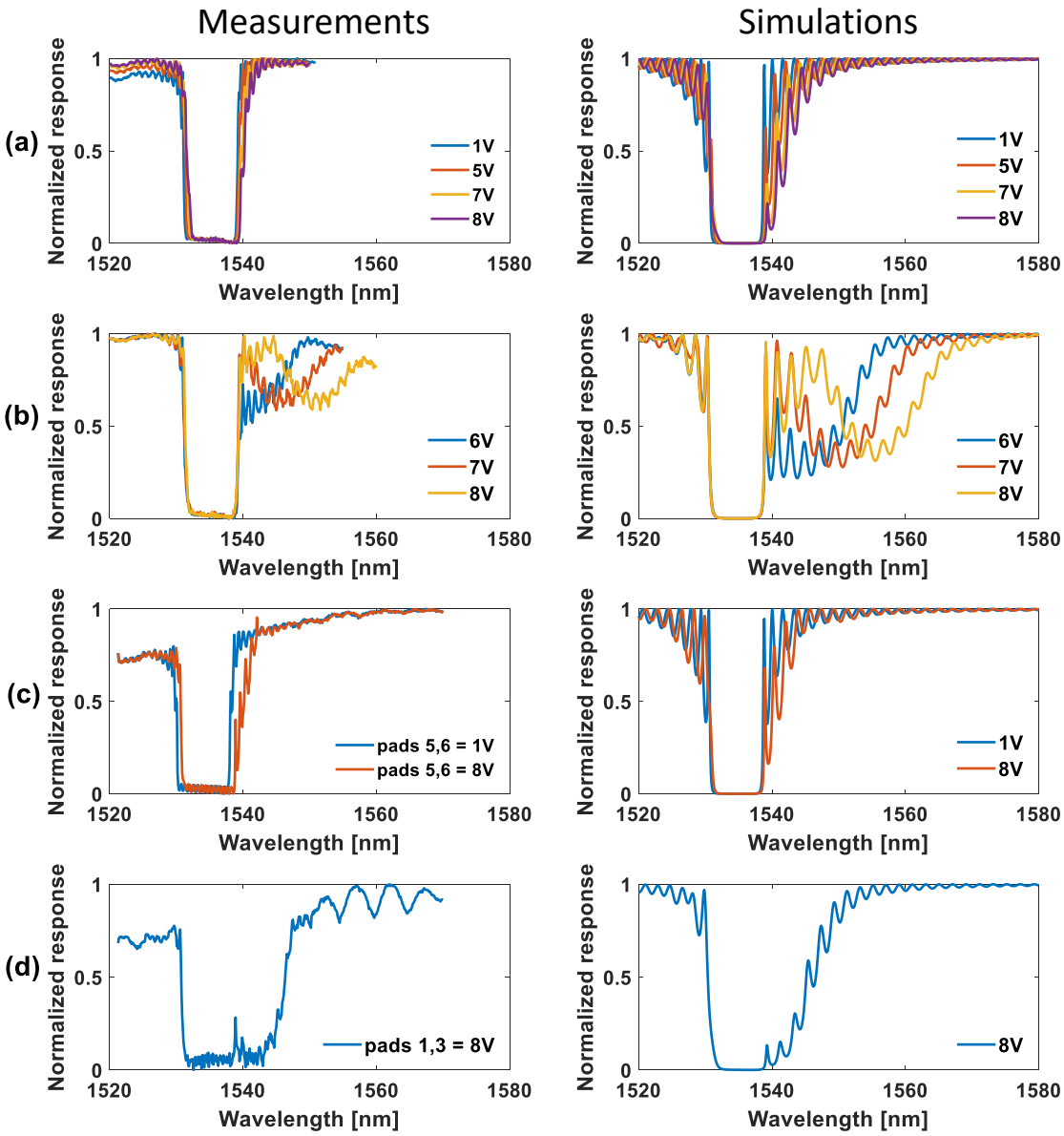

Fig. 3.9 Measured (left) and simulated (right) WBGs transmission responses with 0.01 nm resolution for voltages applied to different combinations of pads. Voltage(s) are applied between pads (a) 1 and 6. (b) 1 and 2. (c) 5 and 6. (d) 1 and 3.

valuable insights into the behavior of the proposed device under different operational conditions, facilitating a comprehensive understanding of its capabilities. The low changes in the thermal distribution correspond to low changes in the refractive indices along the WBG

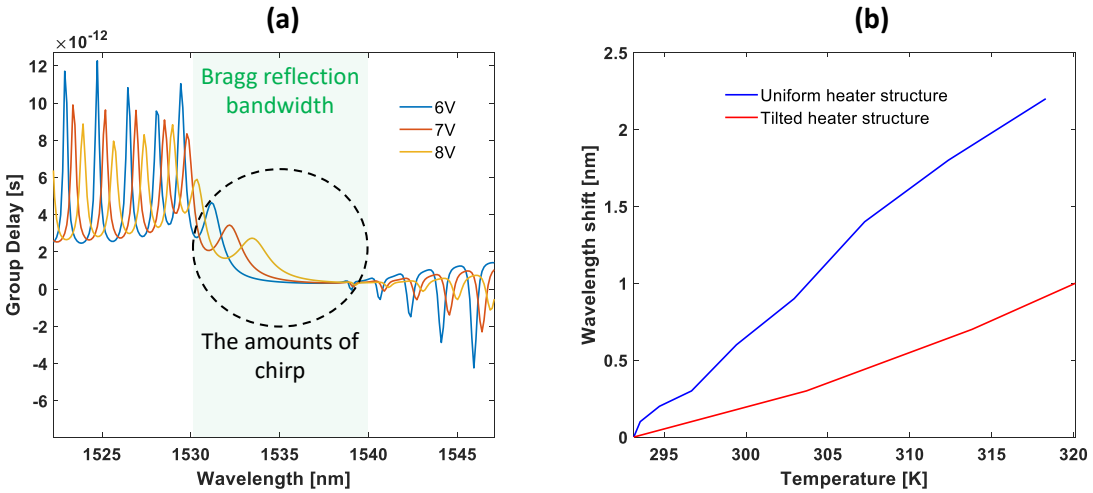

Fig. 3.10 (a) Simulated group delay of the tilted heater structure for different voltages applied on electrical pads 1 and 6. (b) A comparison between the uniform and tilted heater structures, examining wavelength shifts as a function of temperature.

structure. Thus, the chirp is negligible.

3.2.2 Group delay calculations

Based on the experimental results for the tilted heater structure, we calculate the group delay profile for different voltages. Indeed, the group delay values are small due to the short grating length and weak thermal distribution along the WBG structure. Thus, the group delay might not be detected in an experiment, however, a clear increase in the group delay can be indicated by increasing the voltage applied to the electrical pads 1 and 6 as seen in Fig. 3.10 (a). While the group delay values currently fall within the range of a few picoseconds, further increases can be achieved by bringing the tilted heater element closer to the WBG structure or applying a higher voltage. Additionally, enhancing the heater material by using a more conductive metal could facilitate greater refractive index changes.

In Figure 3.10 (b), we examine the shifts in the central wavelength of the filter, also known as the Bragg wavelength (λ_{Bragg}), resulting from temperature changes along the WBG structure. For the maximum applied voltage of 8 V, the drifts are around 2.2 nm and 1 nm for the uniform and tilted heater structure, respectively.

3.3 Discussion on the proposed WBGs

The choice of the parameters for the proposed WBG was based on the length of the fabrication area. We chose 6 equidistant electrical pads to have a wide tunability in such a small length of only 250 μm. We could not add more electrical pads since there were limitations in terms of the spacing between the heater materials according to the fabrication foundry. The simulations were undertaken for the same number of segments, spacing, and length of the device. Table 3.2 provides a summary of the power required to make reconfigurable filers using WBGs.

Table 3.2 Power required to make WBG filter reconfigurable and comparison with relevant works on Si platform

Reference	Length of the device	Heater type	Power required [mW]
This work [92, 93]	250 μm	TiN	0.13 mW
[46]	1.56 mm	PN junction	27.5 mW
[98]	250 μm	NiCr	47.3 mW
[109]	<200 μm	Micro-heater	11 mW

By extending the grating length, increasing the number of electrical pads, and incorporating independent heating elements, we can induce a broader range of perturbations in the refractive index. This allows for more precise control over shaping the spectral response of

the device. An additional strategy for improvement involves thermal isolation, achieved by introducing an unheated segment between two neighboring heated segments, as proposed by Zhang et al. in [46].

For example, the structure presented in Fig. 3.11 (a) serves as a means to enhance the heat distribution depicted in Fig. 3.4 (e), with the corresponding spectral response shown in Figure 3.6 (a). In contrast to a one-block heater element, this proposed structure is designed so that each segment is controlled by an independent heater element. Moreover, the unheated segment serves to minimize thermal crosstalk. Simulation results confirm that the discontinuity in the heater element effectively blocks heat dissipation to other segments, as depicted in Fig. 3.11 (b) and (c) when the thermal isolation is 50 μm and 30 μm, respectively. The corresponding spectral responses indicate that the FP resonances and distinct reflection bands become more pronounced, particularly with 50 μm isolation.

Simulations show that the necessary length of the unheated segment to maintain thermal isolation while still ensuring spectral results similar to Fig. 3.11 (c) is approximately 30 μm. Fig. 3.11 (d) is the same as Fig. 3.6 (a) for easier comparison. However, there is a trade-off between achieving thermal isolation and the amount of reconfigurability. In other words, if the two segments are isolated as shown in Fig. 3.11 (a), electrical pads 1 and 3 can no longer be activated. Thus, a new design is required to achieve the case in Fig. 3.5 (c). The ultimate choice between a single-block heater and multiple independent heater blocks depends on the specific requirements of the target application.

Additionally, in the design of WBGs, apodization plays a crucial role in shaping the spectral response and optimizing performance. Apodization involves deliberately modifying the amplitude or refractive index profile of the grating along its length. This technique

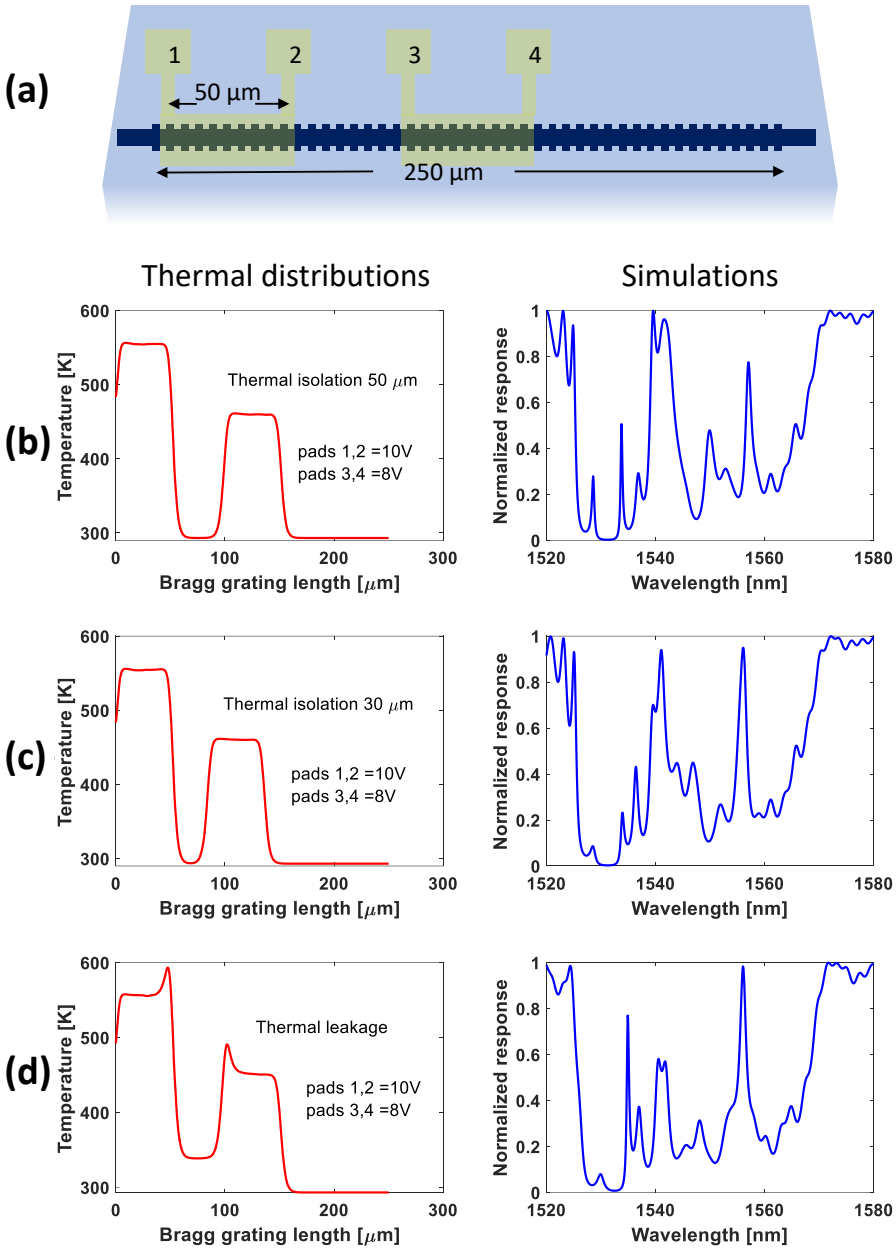

Fig. 3.11 (a) The simulated schematic diagram when there is no thermal crosstalk between electrical pads 2,3, namely, the heater element is divided into two independent blocks. (b) Thermal isolation of 50 μm and the corresponding spectral response. (c) Thermal isolation of 30 μm and the corresponding spectral response. (d) Thermal leakage and the corresponding spectral response.

is essential for mitigating issues such as side lobes, optical reflections, and undesired resonances within the grating structure. By carefully tailoring the apodization profile, we can achieve specific desired outcomes, such as flattening the pass-band, enhancing the side-lobe suppression, or reducing the group delay ripple. Apodization is particularly important in applications like optical communications and sensing, where precise control over the spectral characteristics of the grating is crucial for achieving optimal system performance and mitigating signal distortions [110, 111].

3.4 Cascaded MZMs for optical frequency comb generation

In recent years, OFC generators have attracted attention as a multi-wavelength source in optical communications systems such as DWDM, Optical Time Division Multiplexing (OTDM) systems, and microwave photonics [55]. OFC is defined as a series of discrete, equally spaced spectral lines in the frequency domain. One of the most widely used methods for OFC generation on-chip is based on EO modulation of a Continuous Wave (CW) laser, this method includes microring resonators [112, 113], or cascaded MZMs [114, 115]. This method exploits the nonlinear interaction between an optical carrier and a RF signal in an EO modulator. Key advantages of this approach include the ability to achieve a wide range of comb spectra and precise control over comb properties, such as center frequency and spacing between comb lines, through simple adjustments to input wave properties.

In this section, we explore the feasibility of generating EO modulation-based OFC using integrated 3-cascaded push-pull traveling-wave MZMs in SOI. Leveraging the periodic response of the modulator, we produce two sets of comb lines using two narrow linewidth ITLAs, each operating at a specific wavelength. We demonstrate that any pairing of two

modulators can yield two sets of 9 comb lines with amplitude variations within the range of $4.5 - 5$ dB.

The designed modulator exhibits a 3 dB bandwidth of approximately 15 GHz, with the maximum bandwidth of the generated OFC reaching 144 GHz. This limitation is determined by the modulator bandwidth and the capabilities of the RF signal generators. While the generation of OFC using three cascaded MZMs poses several challenges, we envision that this approach holds significant potential for future integrated OFC generation on SiP chips, particularly for applications in optical signal processing and microwave photonics.

3.4.1 Operating principles

The operating principles for generating OFCs using cascaded modulators is demonstrated in Fig. 3.12 and can be summarized as follows: Initially, the first modulator is fine-tuned to produce three spectral components. This involves applying an RF signal at frequency f_1 with appropriate RF power adjustments and tuning the DC bias and heater voltage of the corresponding modulator. Then, the second modulator, cascaded in series, re-modulates these three spectral components using another RF signal at a frequency of $f_2 = f_1/3$. As a result of this operation, nine comb lines are generated, with a frequency separation of f_2 between each comb line. To further refine the process, a third cascaded modulator is introduced to re-modulate the nine spectral components. This is achieved by employing a third RF signal generator at a frequency $f_3 = f_2/3 = f_1/9$, expanding the comb lines to 27 with a frequency spacing equal to f_3, and so forth. It is crucial to synchronize the RF signal generators to ensure uniform amplitude and phase across the resulting comb lines.

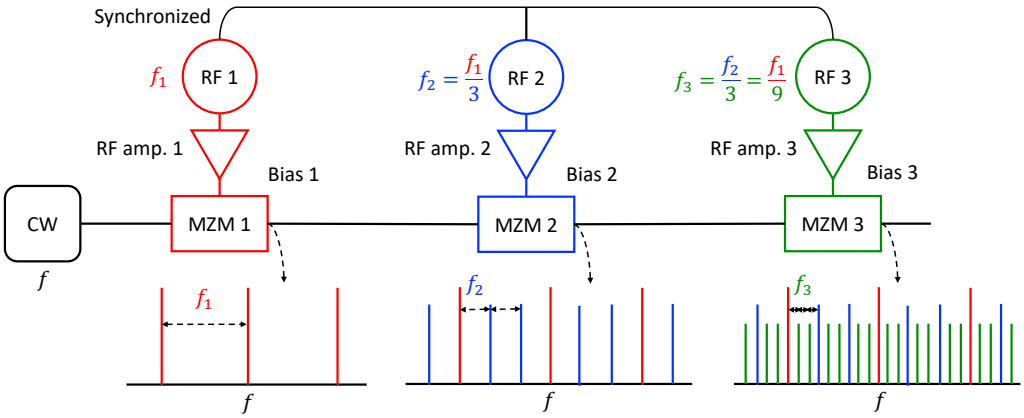

Fig. 3.12 Principle of OFC generation using cascaded modulators.

3.4.2 Device design and fabrication

Fig. 3.13 (a) illustrates the layout of the 3-cascaded MZMs, along with a photograph of the SiP chip under test. Operating in a push-pull configuration, these modulators are fabricated on a 220 nm SOI wafer with a 2 μm buried oxide, utilizing a CMOS-compatible foundry process at AMF during a multi-project wafer run. The three modulators are identical, each featuring a path imbalance of 100 μm. This imbalance introduces an additional phase shift in one of the arms of the Mach-Zehnder Interferometer (MZI), creating a periodic spectral response. To fine-tune the modulator response, an n^{++} doped heater with a total length of 382 μm overlays the upper arm of each modulator. The individual modulator dimensions include a length of 2.42 mm and a net p-n junction loading of 2.04 mm.

The 3 MZMs are connected in series using compact Y-branches. To facilitate the characterization of each modulator separately, additional taps are employed, resulting in an increase in insertion loss as each tap reduces the output optical power by 3 dB. Input and output coupling, as well as testing, are achieved through VGCs designed for TE mode operation over the C-band. The device size, excluding the length of the waveguides to the VGCs, is 1.42

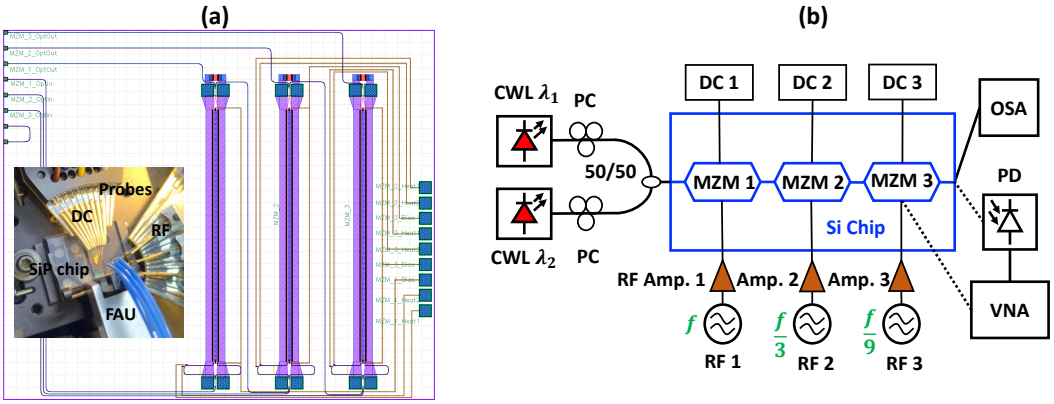

Fig. 3.13 (a) Layout of the device design. The inset shows a zoom-in picture of the SiP chip, FAU, DC and RF probes. (b) Schematic diagram of the experimental setup.

mm × 2.56 mm. Each modulator is equipped with a 50 Ω electrode matching termination.

The experimental setup, depicted in Fig. 3.13 (b), involves the use of two ITLAs to launch optical power into the SiP chip at two distinct wavelengths. The ITLAs have a relatively narrow linewidth below 100 kHz. To ensure optimal performance during characterization, each branch is equipped with a Polarization Controller (PC) to align the polarization of the input light with the waveguide's preferred polarization state.

The two wavelengths are combined using a 3-dB coupler, and the resultant output is directed into the VGCs on the SiP chip. The total optical input power to the SiP chip amounts to 14 dBm, with the chip insertion loss reaching approximately 40 dB. This includes a 10 dB insertion loss for the VGCs and an additional 10 dB for each modulator. Again, this is due to the Y-branches existing between each modulator to be able to characterize each modulator separately. To drive the 3-cascaded MZMs, three RF signal generators and RF amplifiers are utilized through a custom-designed high-frequency GS-GS-GS RF probe. This probe is tailored to match the spacing between the electrical pads on the SiP chip. Two of the RF amplifiers feature a gain of 26 dB and a bandwidth of 33 GHz, while the third amplifier

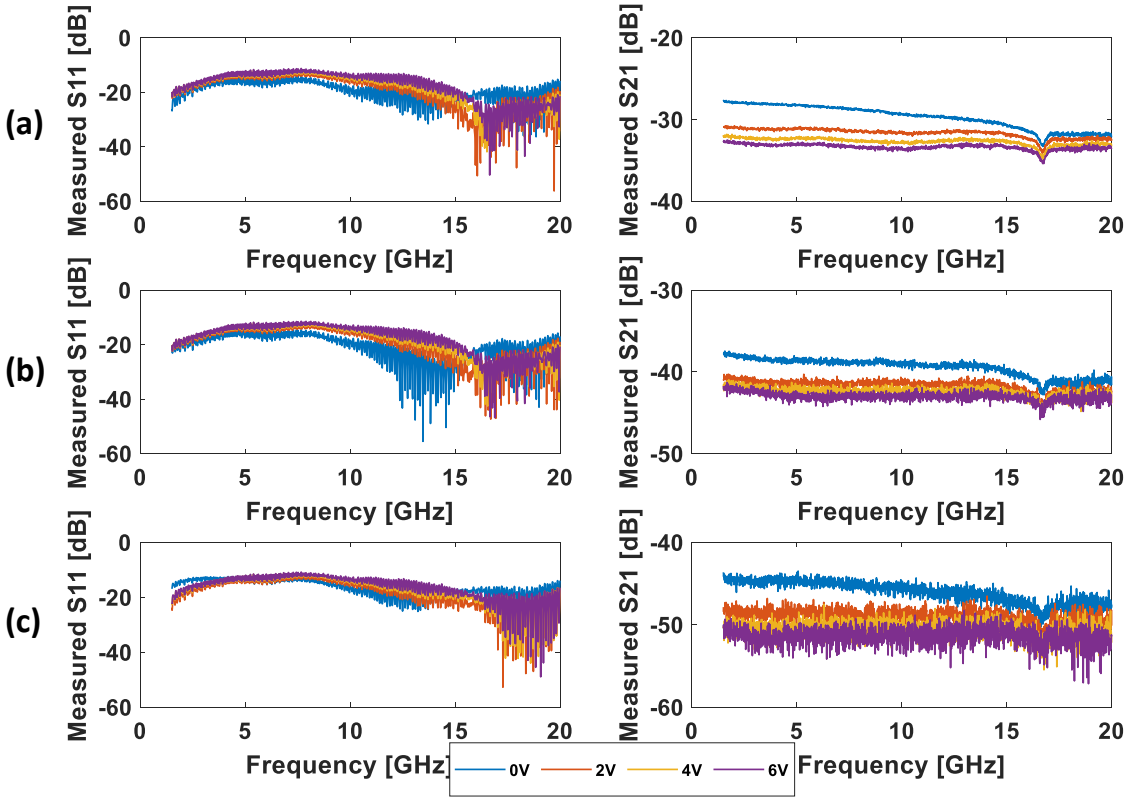

Fig. 3.14 (a) Measured EO responses S11 and S21 of the three MZMs: (1) MZM 1, (2) MZM 2, (3) MZM 3.

has a gain of 16 dB with a bandwidth of 25 GHz. The output optical spectrum of the chip is monitored using an Optical Spectrum Analyser (OSA) with a resolution of 0.01 nm. Small signal properties of the three MZMs are characterized using a 20 GHz Vector Network Analyzer (VNA) at various DC bias voltages. The characterizations of each modulator are illustrated in Fig. 3.14. The curves are normalized to the response at a reference frequency of 1.5 GHz, showcasing a 15 GHz bandwidth achieved under a 6 V bias voltage.

3.4.3 Experimental results

By adjusting the amplitude of the first RF signal (RF 1) and the heater voltages of MZM 1, we generate two first-order sidebands with amplitudes quite similar to the seed carrier. These three spectral components, with a frequency spacing f controlled by RF 1, are then injected into MZM 2. MZM 2, driven by another RF signal generator (RF 2), utilizes these as new seed carriers to produce additional first-order sidebands. The result is the observation of 9 comb lines with a frequency spacing $f/3$ from RF 2. Now, making use of the periodic response of MZMs, we fine-tune the two wavelengths from the two ITLAs to generate two sets of 9 comb lines. One ITLA is set to a specific wavelength ($\lambda_2 = 1553.188$ nm) close to the quadrature point of one modulator. The RF power of the signal generator, heater, and biasing voltages of the corresponding modulator are adjusted until 3 flat-top comb lines are achieved. Another RF signal is then launched into the second (cascaded) modulator, and the heater and biasing voltages are adjusted to obtain a set of quite flat-top 9 comb lines.

To generate another set of 9 comb lines, we fine-tune the wavelength of the second ITLA around the periodic raising edge of the modulator response without changing the heater or bias voltages. In this case, the second wavelength is around 1544.156 nm. This precision is crucial because any changes in the heater or biasing voltages significantly impact the first set of comb lines. The fine-tuning of the second wavelength is achieved with a step resolution of 1 pm, as illustrated in Fig. 3.15. The resulting 9 comb lines exhibit a frequency spacing of 10 GHz and amplitude variations within the range of $4.5 - 5$ dB.

We observe that the third modulator faces challenges in fully re-modulating the 9 comb lines, attributed to factors such as the high insertion loss of the device and insufficient RF gain from the RF amplifiers to amplify the RF signal on the third modulator. Another

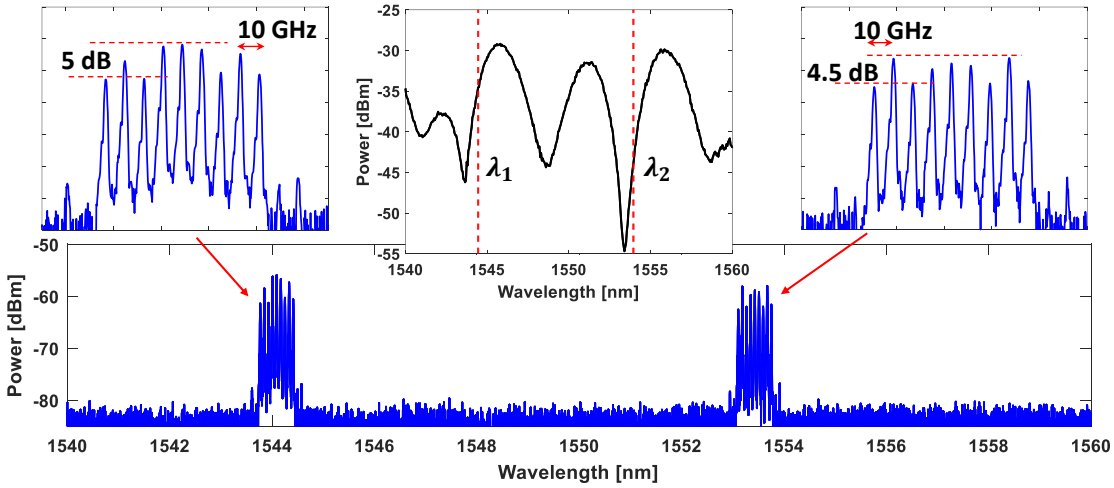

Fig. 3.15 OFC generation using two independent ITLAs, the wavelengths are set at $\lambda_1 = 1544.156$ nm and $\lambda_2 = 1553.188$ nm. The middle curve shows the optical spectrum when the optical power is launched into MZM 1 and the output is observed at MZM 2. The generated 9 comb lines have a frequency spacing of 10 GHz and amplitude variations within 4.5 to 5 dB. The OSA resolution is 0.01 nm, and spectra are captured without averaging.

noteworthy aspect is the impact of the heater voltage on the third modulator, where we find that modifying this parameter affects the generated comb lines even when the optical power is launched between the first two modulators only. This observation suggests that changes in the temperature of the SiP chip have a comprehensive influence on the overall device performance.

To enhance the overall device performance and ensure sufficient power reaching the third modulator, we propose removing the additional tapers. We believe that such modifications can lead to improvements in the device design. In theory, utilizing the generated 9 comb lines as a seed carrier into a third modulator, driven by a third RF signal generator (RF 3), should result in each carrier generating two first-order sidebands, yielding a total of 27 comb lines, and so forth.

Fig. 3.16 (a) depicts the scenario when we drive the three-cascaded modulators with RF frequencies of 36, 12, and 4 GHz, respectively. It is noteworthy that some frequency components are challenging to be detected. The optimization of the generated OFCs is achieved through careful control of the biasing and heater voltages of the three modulators, along with the RF power used to drive the RF amplifiers. In Fig. 3.16 (b), we explore amplitude variations as a function of frequency spacing for 2-cascaded modulators (MZM 1 and MZM 2 or MZM 2 and MZM 3). The maximum achievable frequency spacing is 16 GHz, resulting in an overall achievable bandwidth of 144 GHz. These findings are constrained by the modulator bandwidth and the limitations of the RF signal generators. As observed, an increase in frequency spacing between the comb lines corresponds to more fluctuations in amplitude. This behavior stems from the inherent characteristics of the modulation process. Investigating these amplitude variations is crucial, as they impact the stability and uniformity of the comb lines, limiting their applications in scenarios where consistent and evenly spaced frequency components are essential, such as in spectroscopy and optical communications. Therefore, the control and mitigation of these amplitude variations are imperative for optimizing the performance of OFCs generators. We believe that cascading two or more EO modulators on-chip can be used as a building block for advanced integrated subsystems for applications in optical communications, microwave photonics, and optical signal processing.

3.4.4 Discussion on OFC generation

Other OFC generation methods such as that based on supercontinuum generation can produce a broadband of closely spaced frequency lines over a wide spectral range [116]. This method enables high repetition rates, enabling applications in fields like high-speed precision spectroscopy [117], low-noise microwave generation [118], and optical arbitrary waveform

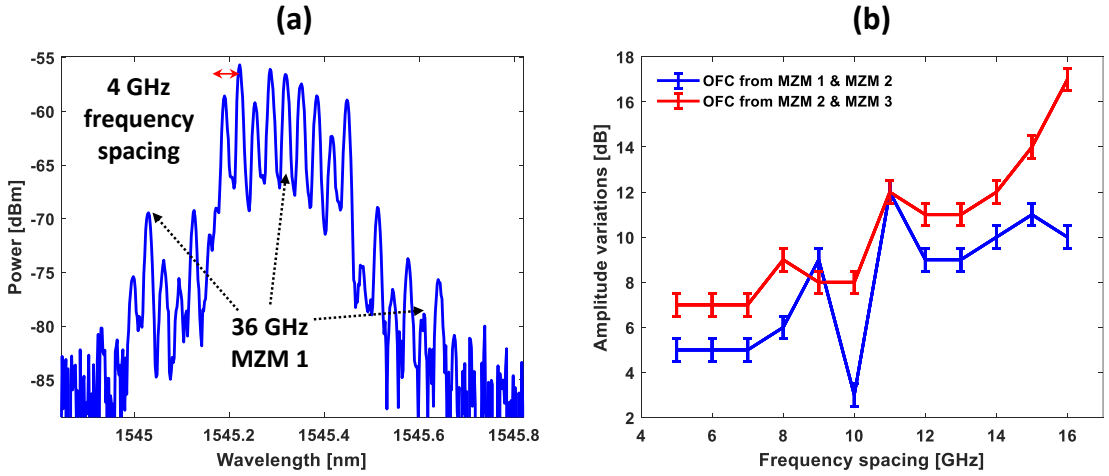

Fig. 3.16 (a) OFC generation using 3 cascaded MZMs, the RF signal generators are set at 36, 12, and 4 GHz frequencies, respectively, resulting in a frequency spacing between the comb lines of 4 GHz. (b) Amplitude variations as a function of frequency spacing between comb lines for two cascaded MZMs.

generation [119]. However, achieving optimal supercontinuum generation requires precise control over parameters such as input pulse characteristics, dispersion, and nonlinear effects, and it also requires high optical power. In addition, spectral coherence and stability can be susceptible to environmental factors like temperature variations and mechanical perturbations, requiring active stabilization techniques. The peak power of individual comb lines might be lower compared to other comb generation methods, which could impact certain applications requiring high peak powers. On the other hand, the OFC generation using cascaded MZMs offers better tunability in terms of the frequency spacing between the comb lines and the peak power variations. However, this method is limited by the bandwidth of the modulators, the RF amplifiers and signal generators.

3.5 Summary

In summary, we introduced a programmable WBG capable of achieving versatile spectral responses, facilitating the implementation of multi-band filters and FP-like filters. While alternative approaches, such as employing multiple gratings with individual heating elements for multi-band filters or using pairs of gratings separated by a length of waveguide with heating elements for FP filters, exist, our proposed design stands out for its simplicity and ease of reconfiguration. Demonstrating a proof-of-principle, we have shown that the proposed WBG offers advantages in terms of performance and adaptability. Simulations align closely with the measured responses, affirming the viability of the device. We envision further optimization of this structure for applications in integrated microwave photonics, optical signal processing, and the creation of chirped or phase-shifted grating structures.

We also demonstrate the feasibility of generating OFCs using 3-cascaded MZMs on-chip, however, due to the high insertion loss and low RF power, the third modulator could not generate 27 comb lines. Furthermore, we explored the amplitude variations as a function of frequency spacing for 2-cascaded modulators, we achieved a maximum frequency spacing of 16 GHz, leading to an overall achievable bandwidth of 144 GHz. These results were constrained by the modulator bandwidth and limitations of the RF signal generators. Our findings contribute valuable insights into the potential applications and limitations of cascaded MZMs in optical signal processing applications.

Chapter 4

Quantum-Dash Mode-Locked Laser Diodes for High-Capacity Coherent Communications

4.1 Introduction

To serve the ever-increasing demand for high-speed data transmission rates, optical communication systems have been evolving rapidly in recent years [120]. Today's fiber optic communication systems achieve their impressive capacity thanks to WDM, a method that merges data channels operating at various wavelengths, typically relies on numerous separated lasers, and offers significant potential by effectively utilizing the bandwidth of optical fiber. OFC sources have emerged as a promising alternative to multiple lasers in WDM systems. This shift offers advantages such as stable spacing and broad phase coherence

among the comb lines, enhancing the spectral efficiency of transmission systems while potentially saving energy in WDM transmitters. In this chapter, we delve into a comprehensive exploration of QD-MLLDs and their performance in coherent transmission systems.

Table 4.1 provides a summary of recent findings regarding the utilization of QD-MLLDs in coherent optical transmission systems. Various designs of QD-MLLDs demonstrate that these devices can exhibit diverse frequency spacings between comb lines. This characteristic holds significance in coherent transmissions, as it determines the maximum symbol rate achievable without the occurrence of ISI. The aggregate bit rates, in turn, are influenced by factors such as the number of comb lines, frequency spacing, symbol rate, modulation format, and polarization multiplexing. For example, in [56], the authors used a 56-channel InAs/InP QD-MLLD with a 28.4 GHz frequency spacing to demonstrate a transmission of an aggregate data rate of 12.5 Tb/s using 16QAM modulation format over 100 km of SSMF. This marks a significant advancement for QD-MLLDs, showcasing the highest data rate. Another demonstration of a high aggregate data rate, achieving 12 Tb/s over 75 km of SSMF, was demonstrated in [60]. In this study, the authors used a QD-MLLD with 60 channels and a 25 GHz frequency spacing between each channel. Despite employing a high-order modulation format of 32QAM, the symbol rate remained relatively low at 20 GBd. Such high data rates can be achieved using a dual polarization scheme. In summary, there is a trade-off among these parameters. It is also important to note that coherent transmission systems are not only limited by the characteristics of QD-MLLDs but also the electronic limitations, such as the bandwidth of DACs, ADCs, BPDs, and DP-IQMs.

The work in this chapter is published in [128, 129]

Table 4.1 QD-MLLDs used for optical data transmission

Reference	Number of comb lines	Freqyency spacing [Ghz]	Symbol rate [GBd]	Aggregate bitrate	Modulation format	Fiber length [km]	BER	Single/dual polariza-tion
This work	10	100	96	1.92 Tb/s	4QAM	80	$< 3.8 \times 10^{-3}$	Single
	1	-	80	480 Gb/s	64QAM	80	$< 2 \times 10^{-2}$	Single
	20	50	50	4 Tb/s	16QAM	80	$< 2 \times 10^{-2}$	Single
[21]	52	28.4	32	256 Gb/s	16QAM	b2b	$< 2 \times 10^{-2}$	Dual
[56]	56	28.4	28	12.5 Tb/s	16QAM	100	$< 3.8 \times 10^{-3}$	Dual
[57]	48	34.2	28	10.8 Tb/s	16QAM	100	$< 1.6 \times 10^{-2}$	Dual
[121]	48	34.2	28	5.4 Tb/s	PAM4	25	$< 1.6 \times 10^{-6}$	Dual
[122]	12	25	18	800 Gb/s	16QAM	78	$< 2 \times 10^{-3}$	Single
[123]	23	50	45	4.14 Tb/s	4QAM	75	$< 1 \times 10^{-9}$	Dual
[62]	38	42	38	11.55 Tb/s	16QAM	75	$< 1.4 \times 10^{-2}$	Dual
[61]	47	34.36	32	12 Tb/s	16QAM	b2b	$< 3.8 \times 10^{-3}$	Dual
[124]	50	40	25	100 Gb/s	4QAM	10	$< 3.8 \times 10^{-3}$	Dual
[60]	60	25	20	12 Tb/s	32QAM	75	$< 4.4 \times 10^{-3}$	Dual
[125]	36	34.5	12.5	1.8 Tb/s	4QAM	50	$< 4 \times 10^{-3}$	Dual
[126]	25	42	18	1.56 Tb/s	16QAM	75	$< 1 \times 10^{-2}$	Single
[127]	4	100	28	112 Gb/s	OOK	100	$< 1 \times 10^{-9}$	-

4.2 Characteristics of the QD-MLLD comb source

A simplified schematic of the QD-MLLD used in this work is depicted in Fig. 4.1(a). The QD-MLLD is a specialized InP-based p-n blocked buried heterostructure Fabry-Pérot (FP) laser. The core of the laser structure comprises a 170 nm thick Indium Gallium Arsenide Phosphide (InGaAsP) waveguide with 10 nm $In_{0.816}Ga_{0.184}As_{0.392}P_{0.608}$ (1.15Q) barriers that encase five layers of InAs QDashes, serving as the active gain region. These layers are elongated in the direction transverse to the beam propagation inside the laser cavity and are surrounded by cladding layers of both n- and p-type InP material. The n-type InP cladding includes 1.03Q ballast layers, optimizing the laser's optical performance. The InAs QDash material was grown using Chemical Beam Epitaxy (CBE) and underwent additional processing through Metal-Organic Chemical Vapor Deposition (MOCVD) to create the buried heterostructure. Each active layer had an average QDash density of around $1.5 \times 10^{10}\,\mathrm{cm}^{-2}$. The laser's 1735

μm long waveguide was crafted using standard photolithography techniques, involving dry and wet etching, and contact metallization. A 2 μm wide waveguide mesa was formed to confine the current. The laser chip was mounted on a commercially available Aluminum Nitride (AlN) carrier with gold electroplated contacts and packaged into a standard 14-pin butterfly laser diode as shown in Fig. 4.1(a) inset. In [130,131], it has been demonstrated that the central wavelength of the spectrum of the QD-MLLD and the number of the generated comb lines depend on the cavity length, the number of stack layers, and the height of the QDash material.

The temperature of the QD-MLLD is controlled by a Thermoelectric Cooler (TEC) and biased by a Laser Diode Controller (LDC). The QD-MLLD exhibits a lasing threshold at approximately 50 mA and can achieve an average output power of 40 mW when operated at a bias current of 450 mA. At this operating point, its 6 dB optical bandwidth extends to approximately 9 nm, and it produces over 50 comb lines with a comb spacing (or FSR) of 25 GHz, corresponding to an approximate wavelength of 0.2 nm. It is obvious that increasing the bias current leads to an increment in the number of optical comb lines present in the 3-dB bandwidth as well as a slight shift of the overall optical spectrum towards longer wavelengths. It is important to note that not all these comb lines can be used for data transmission, the side comb lines do not have the same average peak power-to-noise ratio as the middle comb lines. Therefore, only the comb lines in the middle exhibit the best performance when it comes to data transmission.

To investigate the characteristics of the QD-MLLD source, we conducted a comprehensive assessment of the device using different setup configurations as illustrated in Fig. 4.1(b). We set the operating current at 350 mA and the temperature was set at 27^{o}C using a LDC (ILX Lightwave LDC-3900). This deliberate temperature choice was made to shift the comb

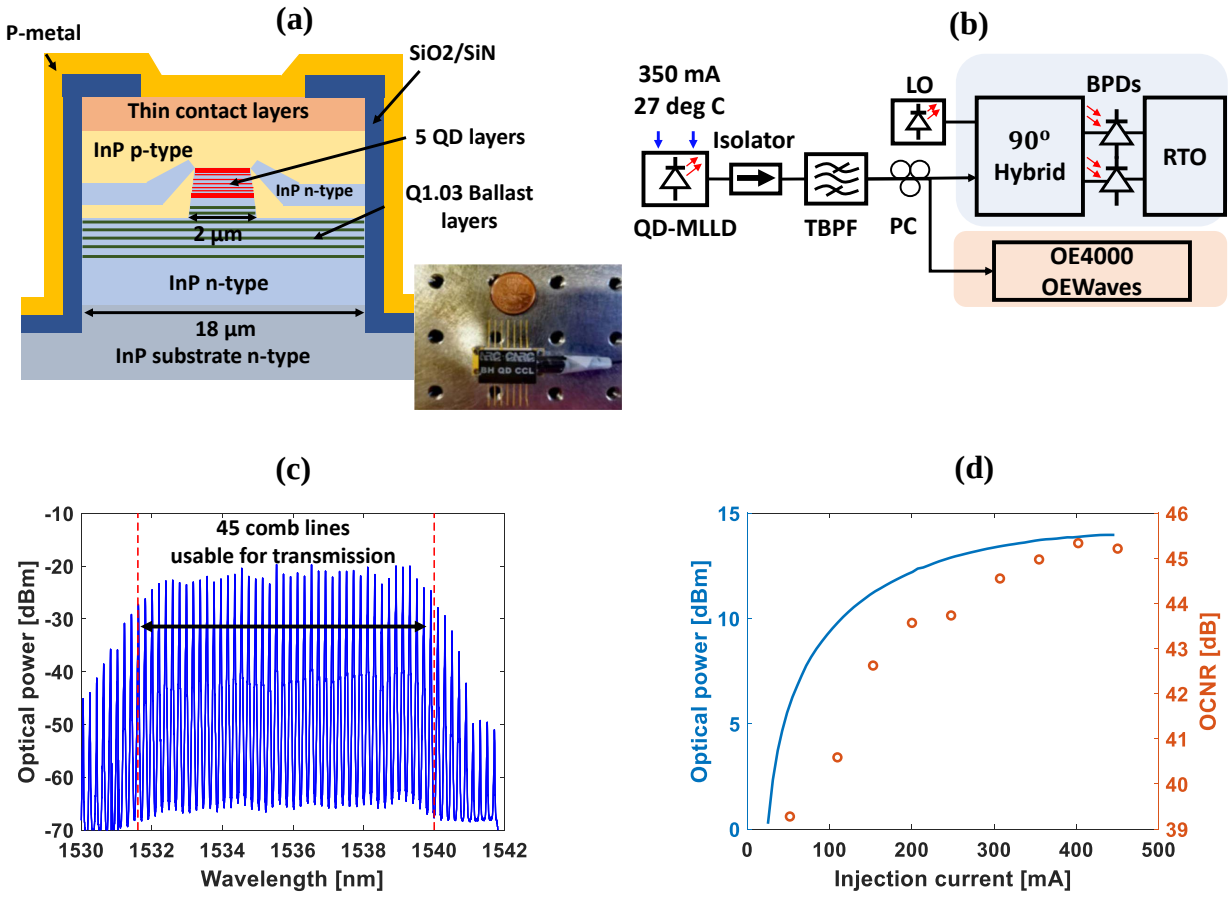

Fig. 4.1 (a) Approximate schematic design of the QD-MLLD, the inset shows a picture of the QD-MLLD after packaging. (b) Experimental setup used to characterize the QD-MLLD. (c) The output optical spectrum of the QD-MLLD with a resolution of 10 pm. (d) Optical output power (blue) and OCNR (red) as a function of injection current.

spectrum towards the C-band. At these operating conditions, there are 45 comb lines (6 dB bandwidth) that are usable for coherent transmission, and the comb lines exhibit OCNR to be around 45 dB as shown in Fig. 4.1(c). While it was possible to increase the temperature further to observe additional shifts towards the middle of the C-band, operating at higher temperatures for a prolonged time is not advisable as it may reduce the lifetime or degrade the performance of the devices. For the safety and optimal functioning of the device, we

maintained it at room temperature. An isolator is used to protect the device from potential back reflections within the system. It is followed by a Tunable Band-Pass Filter (TBPF) (Santec OTF-350) to select two or more carriers from the comb source. The selected carriers are then directed through a PC and combined with a LO laser within a 90^o optical hybrid. The LO used is an ITLA that has a linewidth less than 100 kHz. At the output of the optical hybrid, BPD (Finisar 43 GHz) followed by a 160 GSa/s Real-Time Oscilloscope (RTO) (Keysight 2 channels, 63 GHz bandwidth, 8-bit resolution) are used to capture the in-phase and quadrature component of the beat signal. A fully automated laser linewidth and phase noise analyzer (OEWaves OE4000) is also used to validate the laser linewidth measurements.

Fig. 4.1(d) shows the optical output power and the average OCNR as a function of injection current into the QD-MLLD. The OCNR values are initially calculated for each comb line based on the optical spectrum of the frequency combs that are captured using a 0.01 nm resolution OSA. The OCNR at a current of 300 mA or higher exhibits small variations, approximately within ± 1 dB. The average OCNR shows a consistent increase with injection current and stabilizes at around $44 - 45$ dB beyond 300 mA. It is evident that the output optical power, the number of lines, and the OCNR consistently rise with injection current until they eventually saturate.

It is important to set up the injection current to a high value during transmission experiments because low injection currents do not stabilize the comb source. Thus, we have to choose a value in the range of 300 to 450 mA, of course, without exceeding the current limit of the QD-MLLD. The value of the injection current and operating temperature must be kept constant to avoid changes in the OCNR or drift in the central wavelength of the comb lines. Throughout our experiments, we monitored the LDC current and temperature values

and made sure the accuracy of the stabilization was minimal.

4.2.1 RF beating linewidth measurement

The FSR, or the frequency spacing between the comb lines, is approximately 25 GHz. In the RF domain, there should be a beat signal at that frequency, and the corresponding linewidth in this case is referred to as the RF beating linewidth. The experimental setup in Fig. 4.1(b) can be simplified with just a single photodetector and an Electrical Spectrum Analyzer (ESA) for the RF linewidth measurements. The TBPF is turned off to launch all comb lines into the optical hybrid and BPD. Fig. 4.2(a) shows the measured RF linewidth with respect to the beating RF note at approximately 25 GHz. The Full Width at Half Maximum (FWHM) is measured to be around 35 kHz indicating that the comb tones are closely synchronized and coherent which is essential for reliable data transmission and enhancing signal quality [132, 133]. We repeated this measurement 100 times to observe if there was any drift in the FSR or the RF linewidth. Fig. 4.3(a) and (c) show that the average of the RF beating linewidth is approximately 10 kHz, and small variations in the sub-kHz for the FSR; the corresponding histograms are shown in Fig. 4.3(b) and (d).

4.2.2 Optical phase noise and optical linewidth measurement

To characterize the noise performance of the device, we use an automated laser linewidth and phase noise measurement system (OE4000 OEWaves Inc.) to measure the optical frequency noise of the selected comb line. The optical phase noise is determined by the instantaneous phase of each of the frequency components and originates from ASE noise [134]. For this characterization, the use of an OSA becomes impractical due to its resolution which does not

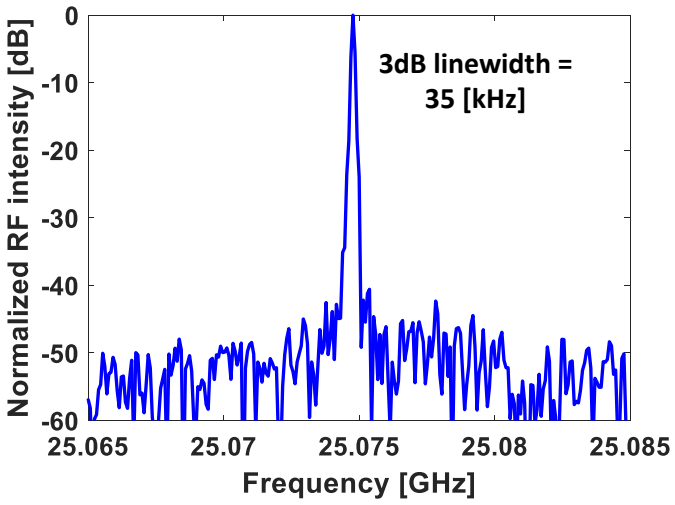

Fig. 4.2 Linewidth measurement of the QD-MLLD highlighting a 3-dB RF linewidth of 35 kHz, at FSR of 25 GHz indicating the frequency spacing between the comb lines.

allow measurements below 0.01 nm. As a result, several indirect measurement techniques for estimating the optical linewidth of narrow-linewidth lasers have been proposed and investigated, these include heterodyne detection [135], self-heterodyne detection [136] and frequency discriminators [137]. The laser linewidth analyzer (OE4000) is a homodyne-based system that does not require another low-noise reference laser source. Briefly, the signal is split into two paths, one of the paths has a phase modulator that is driven by an RF signal generator at a low frequency. The other path has a delay line or a length of fiber to introduce some delay. The resulting signals are mixed and detected by a photodetector. The instantaneous linewidth estimation using the OE4000 analyzer recorded an average optical linewidth of approximately 150 kHz. The comb lines on the edges experienced a larger average optical linewidth of 300 kHz. We note that the measured RF beating linewidth values are about eight orders of magnitude lower than the optical linewidth. This difference can be attributed

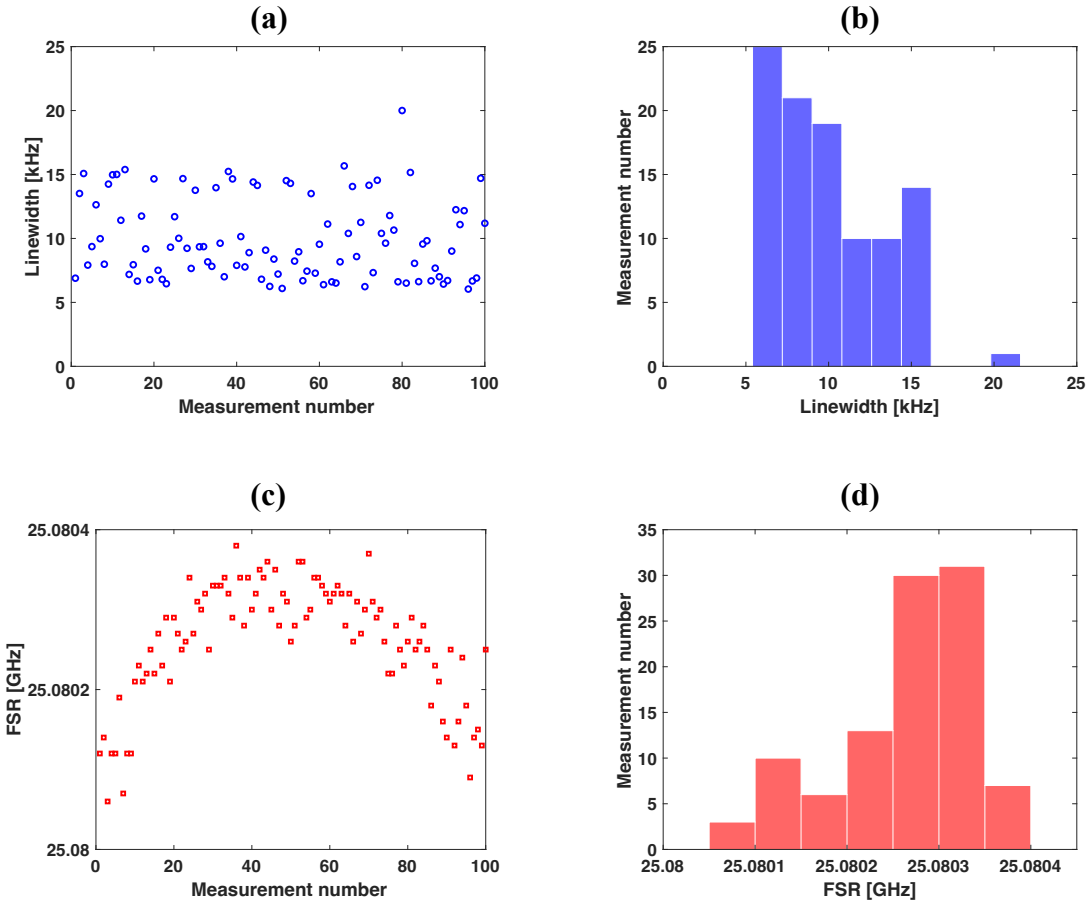

Fig. 4.3 Multiple captures of (a) RF linewidth and (b) FSR measurements of the QD-MLLD.

to the high correlation between the frequency components which results in a reduction of the noise of the beating signal. Note that the transmission performance is relevant to the optical linewidth of the individual comb lines and not the RF beating linewidth.

Semiconductor laser cavities typically have small fluctuations caused by the ASE. The RIN can be identified as the ratio between the small fluctuations to the average output power. The existence of RIN among the comb lines can have a significant impact on overall transmission performance. Specifically, in WDM systems, the RIN associated with individual

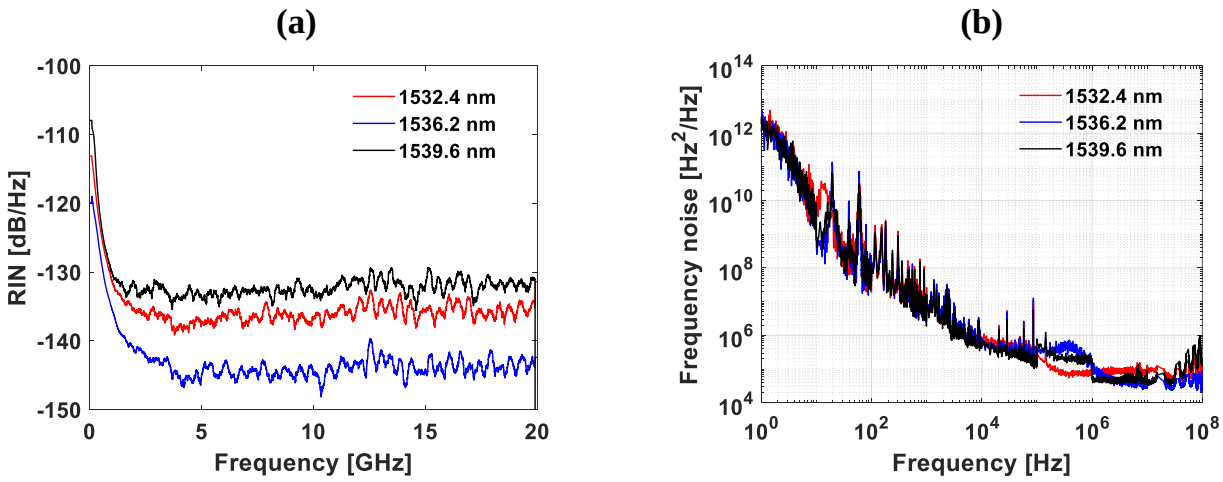

Fig. 4.4 (a) RIN measurements of 3 comb lines selected in the beginning, the middle, and the end of the comb spectrum. (b) Frequency noise measurements of the 3 selected comb lines.

comb lines is more important than the RIN of the whole comb [138]. In the RIN measurement experiment, the RIN for the selected individual channels over a frequency range of 10 MHz to 20 GHz is measured between -130.7 dB/Hz and -145.2 dB/Hz as shown in Fig. 4.4(a), and the frequency-noise spectra are shown in Fig. 4.4(b). Frequency-noise components below 100 MHz are typically mitigated through phase tracking techniques in the DSP, while spectral components exceeding 100 MHz can potentially deteriorate signal quality [62]. Low phase noise and narrow optical linewidth of any semiconductor laser are desirable features for almost any foreseen application, particularly in high-speed optical coherent systems which usually require a narrow linewidth for both the signal and the LO.

4.2.3 The estimated optical pulse of QD-MLLD

In optical communication systems, short pulses are less susceptible to dispersion and nonlinear effects that can occur during optical fiber transmission. Previous literature demonstrated

that QD-MLLDs can emit sub-picosecond pulses [139, 140]. Some nonlinear techniques such as Frequency-Resolved Optical Gating (FROG) or spectral phase interferometry exist to obtain more information on optical pulses [59, 141, 142]. For instance, FROG involves spectrally resolving the autocorrelator output beam, incorporating the spectrum as additional information to recover the laser intensity profile. In principle, an autocorrelator can provide an estimation of the pulse duration generated by a laser, presuming knowledge of the initial pulse shape. Unfortunately, we were not able to measure the optical pulse width of our QD-MLLD, however, we performed an approximate simulation to estimate the expected optical pulse width of such devices. Fig. 4.5 (a) shows the simulation of optical pulses of the QD-MLLD for multiple number of comb lines. As expected, the optical pulse duration is within sub-picosecond. Based on our simulation, we observe that the pulse width is inversely proportional to the number of comb lines. Since our QD-MLLD can emit more than 60 comb lines, including the combs that are not usable for transmission, the pulse width estimation is less than 1 ps as illustrated in Fig. 4.5 (b).

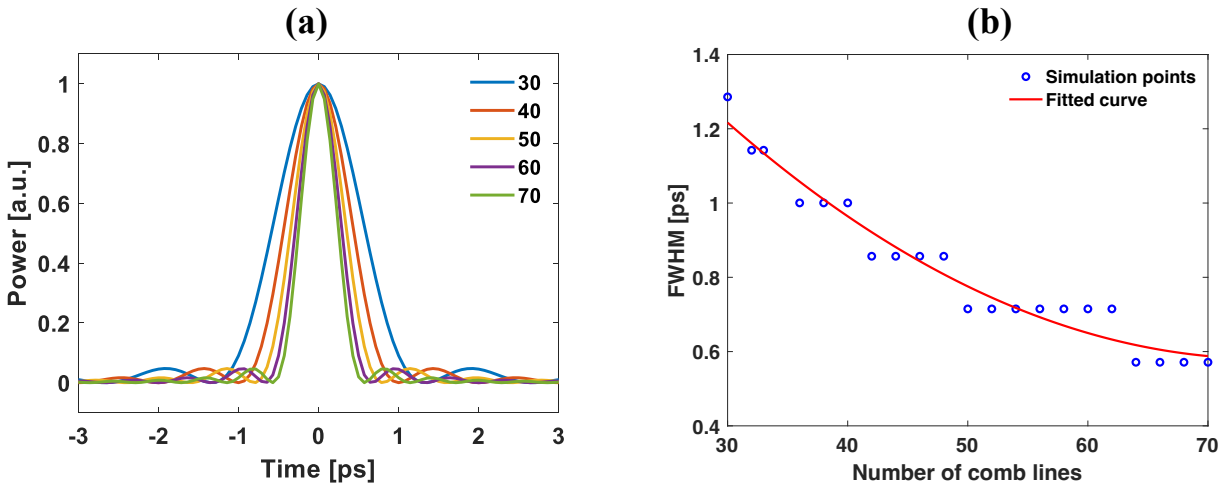

Fig. 4.5 (a) Approximate simulation of the optical pulse of the QD-MLLD. (b) FWHM of the QD-MLLD optical pulse as a function of the number of comb lines.

4.3 Coherent transmission using QD-MLLD

In this section, we showcase the extensive capabilities of QD-MLLDs in coherent WDM transmission. Our focus is on illustrating their performance across high-order modulation formats and symbol rates over 80 km of SSMF transmission. To provide comprehensive insights, we conduct WDM super-channel transmission experiments, highlighting the potential of the QD-MLLD as a versatile multi-wavelength light source for high-capacity optical communication systems. Additionally, we conduct a performance comparison between the QD-MLLD and a commercial narrow-linewidth ITLA, demonstrating that the QD-MLLD is a competitive candidate for high-speed coherent transmissions. Moreover, we demonstrate the potential of such comb sources for future hybrid integration with silicon photonics. In this context, we employ an on-chip silicon photonic modulator to modulate the comb lines in a coherent transmission system over 80 km of SSMF.

4.3.1 Performance analysis of the QD-MLLD

Fig. 4.6(a) illustrates the experimental setup and the DSP routine employed in the system. At the transmitter, we generate the desired symbols for the QAM order. Because of the increased level count and susceptibility to nonlinearity, we implement Nonlinear Pre-Distortion (NLPD) on high-order modulation format symbols through the utilization of a 3-symbol Nonlinear Lookup Table (NLLUT) [143]. These symbols then undergo two essential steps: upsampling and pulse shaping, which are accomplished using a RRC filter featuring a variable roll-off factor. The roll-off factor is set to limit the signal bandwidth to 60 GHz for symbol rates below 120 GBd based on which modulation format is being used. These digital filters pre-compensate the frequency response of the Arbitrary Waveform Generator

(AWG) channels and the RF amplifiers. The AWG (Keysight M8199A) employed in this process boasts a substantial output swing capacity, reaching up to 830 mVpp, and maintains high signal fidelity throughout. Following these preparations, the RF signals are loaded into the SHF QAM transmitter (SHF 46213D, single polarization) equipped with integrated RF amplifiers. To ensure precise control over the modulated signal, the biasing of the IQ modulator within the SHF QAM transmitter is manually adjusted and monitored continuously throughout the entire duration of the experiment.

On the optical side, after the comb source, an isolator is employed to safeguard the device against potential back reflections generated within the system. Subsequently, a TBPF is used to select either a single comb line or multiple comb lines for the WDM transmission as illustrated in subsequent contexts. Following this, a high gain Erbium-Doped Fiber Amplifier (EDFA)1 is used to boost the total power of the comb source to 16 dBm, aligning with the maximum optical input power requirement for the SHF QAM transmitter. A PC is used to control the polarization state of light as the SHF QAM transmitter is a single polarization device. The total number of comb lines that can be used for transmission is 45 comb lines due to their high OCNR. To control the spacing between the comb lines, a programmable optical filter (Finisar Waveshaper 1000s) is used, e.g., to select 10 comb lines with a frequency spacing of 100 GHz. After modulation, optical launch power optimization is carried out using EDFA2 (Oclaro PG2800) to minimize nonlinearities across the 80 km span of SSMF as illustrated in Fig. 4.7 (b). Given an approximate 17 dB fiber loss in the channel, EDFA3 (Oclaro PG2800) is employed to compensate for this loss. The signal is subsequently directed into a 90-degree hybrid and combined with an ITLA functioning as a LO. The output beating signal of the optical hybrid is detected by 43 GHz BPD, followed by analysis with 160 GSa/s RTO (Keysight DSOX96204Q). To meet our experimental requirements, we utilize the RTO's

2 channels with a bandwidth of 63 GHz. The received signals are subsequently processed offline.

Within the receiver's DSP, IQ deskew has been employed to compensate for the mismatching from the BPDs. Then, we apply Gram-Schmidt orthogonalization [144] to rectify any imperfections that may arise from the hybrid. Then, we resample the signals to 2 samples per symbol (sps) to compensate for CD [145] and correct FO. Following this, synchronization is performed using a cross-correlation between the received symbols captured by the RTO and the training symbols. Then, we employ an RRC-matched filter to enhance the SNR. To mitigate linear distortion and phase noise, we utilize a second order PLL [146] that is included within the adaptive blind equalizer based on the LMS algorithm. Lastly, the recovered symbols are de-mapped to bit sequence for BER calculations.

We select a single comb line at around 1536.2 nm (in the middle of the comb spectrum) for our symbol rate sweep analysis. The programmable optical filter is used to filter out any unwanted ASE noise and to guarantee that no additional comb lines were introduced into the modulator. Fig. 4.6(b) shows the measured BER across various symbol rates, encompassing four distinct modulation formats, ranging from 4QAM to 64QAM. The dashed lines represent the back-to-back (B2B) data transmission results. The summary of the achieved transmission net rates is presented in Table 4.2. On a single polarization, we transmit 80 GBd 64QAM over 80 km of SSMF, achieving a BER below the 25% OH Soft Decision (SD)-FEC threshold (BER $< 5 \times 10^{-2}$), corresponding to a net data rate of 447.8 Gb/s. At 4QAM signaling, we transmit a 112 GBd transmission rate over 80 km-SSMF, achieving a BER below the 6.7% OH Hard Decision (HD)-FEC threshold (BER $< 3.8 \times 10^{-3}$), corresponding to a net data rate of 111.1 Gb/s. Next, we demonstrate the performance of the individual channels from the comb source. Fig. 4.6(c) shows a comprehensive view of the measured BER of the

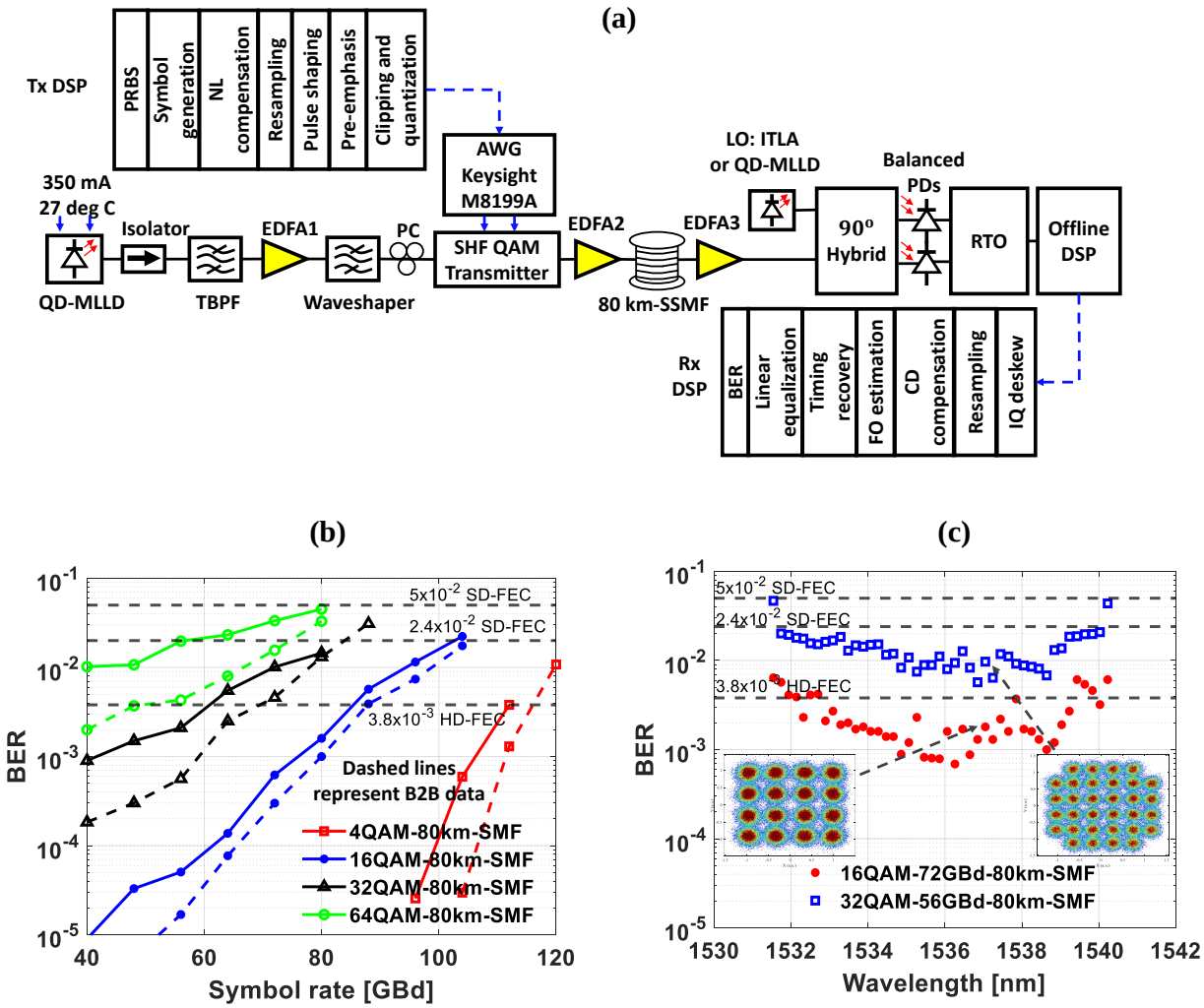

Fig. 4.6 (a) Experimental setup for the coherent transmission experiment with the SHF QAM transmitter, and DSP routine used in both the transmitter and receiver. (b) BER as a function of symbol rate for one of the channels of the QD-MLLD with modulation formats ranging from 4 to 64QAM. (c) BER as a function of wavelengths of the 45 channels usable for transmission over 80 km-SSMF using 16QAM at 72GBd (red dots) and 32QAM at 56GBd (blue squares).

45 channels used for transmission where each channel was characterized individually. We employ 16QAM at 72 GBd signaling and 32QAM at 56 GBd signaling; the inset highlights the constellation diagrams of the corresponding data points. For 16QAM signaling, the majority of the BER values fall below the 6.7% OH HD-FEC threshold. This suggests robust performance and the ability to transmit data at high speeds for almost all channels from the comb source. A noteworthy observation is that there are some challenges at the channels residing on the edges of the comb spectrum. For 32QAM signaling, most BER values remain below the 20% OH SD-FEC threshold. However, there are exceptions – the channels located at both ends of the comb spectrum exhibit slightly higher error rates. The reason behind this behavior can be traced to the fact that these edge channels possess lower peak power-to-noise ratios compared to the channels situated in the middle of the spectrum.

Fig. 4.4(a) also highlights that the channels on the edges have higher RIN. To ensure the reliability of our findings, each BER value underwent multiple measurements, and we computed the average BER. This approach ensures that the reported BER values accurately represent the performance of the channels. Despite variations in the modulation formats and symbol rates, the measured BER values across the channels of the comb source exhibit consistent behavior for high-speed data transmission. This consistency is a positive indicator of the comb source's suitability for various communication applications.

Fig. 4.7 (a) shows the BER performance at different line rates for different modulation formats. The constellation diagram of 16QAM signaling at 96 GBd in Fig. 4.7 (b) indicates the impact of RIN which leads to a scattering of the constellation points for the outer symbols. It is also worth mentioning that reduced phase noise should improve the transmission performance, especially at high-order modulation format and high symbol rates [147].

It is important to note that these results are primarily limited by the bandwidth limitations from the SHF QAM transmitter and BPDs. We also optimize the AWG output voltage, pulse shaping roll-off factor, and the clipping ratio at each symbol rate to achieve the lowest BER.

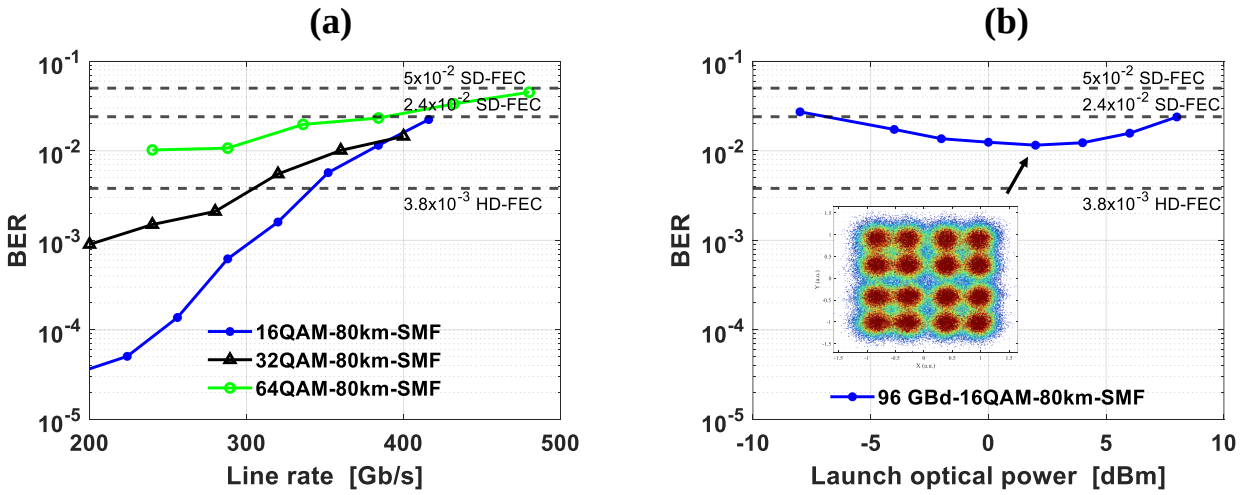

Fig. 4.7 (a) BER as a function of line rate for different modulation formats after 80 km-SSMF transmission. (b) BER as a function of launch optical power for 80 km SSMF.

Table 4.2 Summary of net bitrates after 80 km-SSMF transmission for a single comb line on a single polarization

BER threshold	FEC OH	Modulation format	Net bitrate [Gbps]
3.8×10^{-3}	6.7%	112 GBd 4QAM 85 GBd 16QAM 60 GBd 32QAM	111.1 338.7 298.8
2.4×10^{-2} [148]	20%	104 GBd 16QAM 80 GBd 32QAM	332.8 320
5×10^{-2} [149]	25%	80 GBd 64QAM	447.8

4.3.2 QD-MLLD for super-channel transmission

For a given frequency spacing, the super-channel capacity depends on two parameters: the number of carriers derived from the comb source, determining the number of sub-channels, and the power levels and OCNR of the respective carriers, which dictate the modulation formats for each sub-channel, assuming the carrier linewidth is low enough. Examining the spectrum of the QD-MLLD as depicted in Fig. 4.1 (c), we observe power variations of 2 to 3 dB between the middle comb lines. In practical super-channel transmission systems, it is preferable to maintain uniform power levels across all sub-channels. Given that the ASE noise from the EDFA does not exhibit the same power distribution, it becomes necessary to either attenuate or amplify to address the optical power variations across all sub-channels.

For super-channel DWDM transmission experiments, we use the programmable optical filter (Finisar Waveshaper 1000s) to select 10 comb lines at 100 GHz frequency spacing and equalize the power variations as much as possible. Fig. 4.8(a) shows the 10 modulated comb lines after 80 km-SSMF transmission; the inset shows the comb lines before modulation, captured with an optical spectrum resolution of 10 pm. We transmit 4QAM at 96 GBd, with a guard band of 8 GHz between the modulated signals (4 GHz on each side). On the receiver side, we tune the LO frequency to detect the corresponding channel. Each channel is detected multiple times to ensure the reliability of our measurements. Fig. 4.8(b) shows the BER values of the transmitted WDM channels. All the BER values fall below the threshold of 3.8×10^{-3} accounting for a HD-FEC scheme with 6.7% OH. The net bitrate achieved through this approach is 1.79 Tb/s using only a single polarization scheme. We also use the programmable optical filter to select 20 comb lines at 50 GHz frequency spacing. Fig. 4.8(c) shows 20 modulated carriers at 16QAM 50 GBd before transmission; 200 Gb/s per channel.

Fig. 4.8(d) shows the BER performance of the 20 channels for 4 and 16QAM at 50 GBd signaling after 80 km of SSMF transmissions. The BER of all the 20 channels for 16QAM at 50 GBd lies below the SD-FEC threshold with 20% OH, while the 4QAM signals lie below the HD-FEC threshold. This leads to aggregate data rates of 2 and 4 Tb/s for 4QAM and 16QAM, and net rates of 1.875 Tb/s and 3.2 Tb/s, respectively [129]. It is worth mentioning that these bit rates can be easily doubled if the SHF QAM transmitter is a dual polarization modulator. Unfortunately, we did not have access to a dual polarization emulator either.

Based on these results, the most significant discovery lies not in the net bit rate itself but in the remarkable capability of the comb source to support symbol rates of nearly 100 GBd over extensive transmission distances. This highlights the robustness of the QD-MLLD and its efficiency in enabling high-speed data transmission, making it a promising technology for future high-capacity communication systems.

4.3.3 Comparison of the performance between QD-MLLD and ITLA

In this section, we conduct a comprehensive comparison of the performance between the QD-MLLD and a commercial narrow-linewidth external cavity laser ITLA. The optical output power from the QD-MLLD and the ITLA is kept the same for a fair comparison, approximately around 14 dBm. We explore scenarios where the QD-MLLD serves as the LO and the ITLA as the signal carrier and vice versa and compare to the use of separate ITLAs for the LO and signal carrier. Fig. 4.9(a) shows the BER values as a function of symbol rate up to 120 GBd for different modulation formats (4QAM, 16QAM, 32QAM, and 64QAM) for three scenarios: (1) red curves: two ITLAs are used for signal carrier and LO, (2) blue curves: QD-MLLD is used as a signal carrier and ITLA is used as a LO, and (3) black curves:

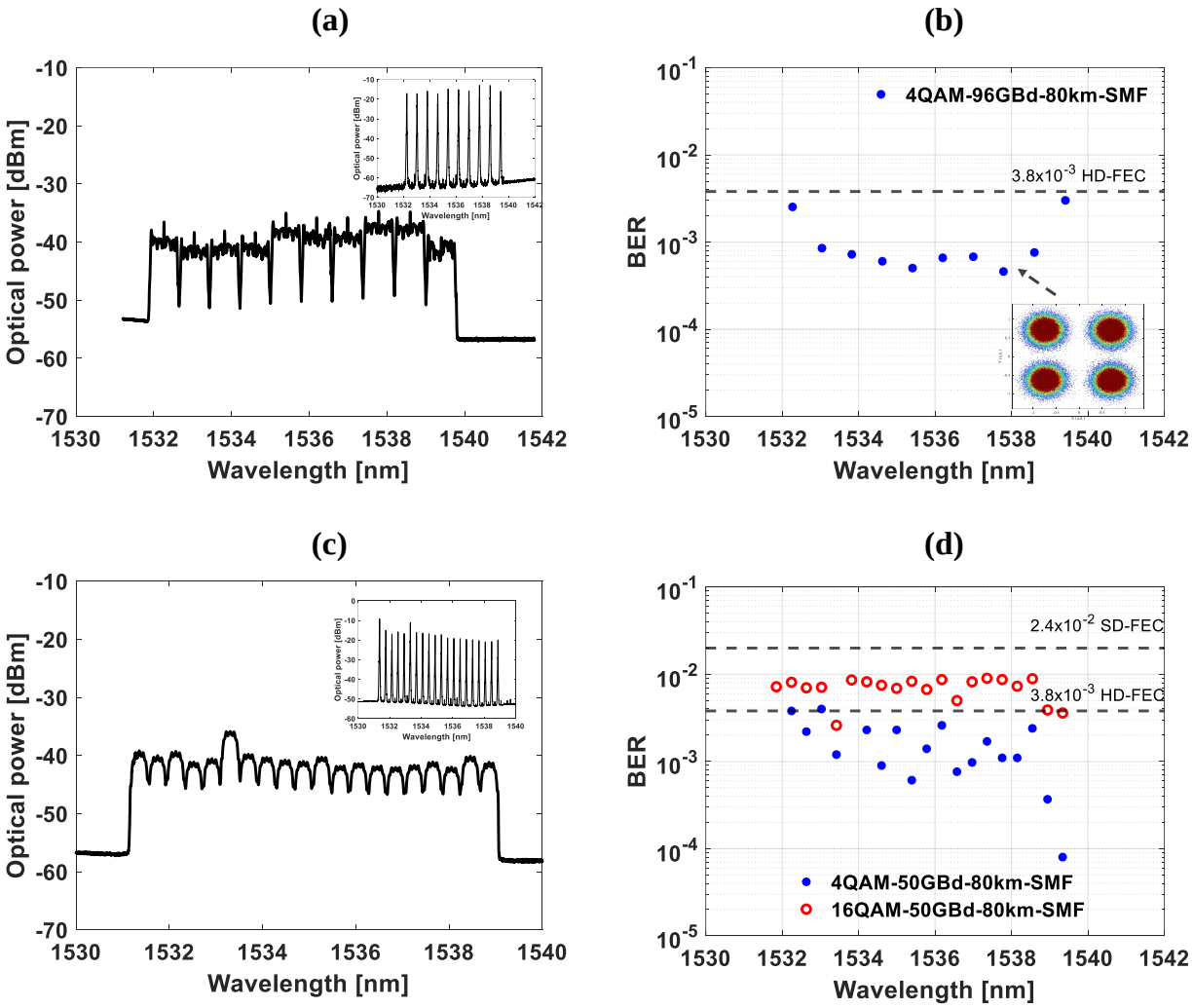

Fig. 4.8 (a) Comb spectra of the 10 channels before modulation (inset) and after transmitting over 80 km-SSMF. (b) BER of the 10 transmitted channels with 100 GHz spacing using 4QAM at 96 GBd modulation signal, the inset shows the constellation diagram of one of the channels. (c) Comb spectra of the 20 channels before modulation (inset) and after transmitting over 80 km-SSMF. (d) BER of the 20 transmitted channels with 50 GHz spacing using 4QAM and 16QAM at 50 GBd modulation signal.

ITLA is used as a signal carrier and QD-MLLD is used as a LO.

The results demonstrate that the QD-MLLD and the ITLA exhibit comparable performance. However, when the comb source is used as the LO, there is a slight degradation in performance, which can be attributed to variations in the comb source power. To further assess their performance, we compare the BER as a function of Optical Signal-to-Noise Power Ratio (OSNR). For 16QAM at a symbol rate of 56 GBd, the three cases exhibit approximately similar behavior as shown in Fig. 4.9(b). However, we can see a degradation in the performance when we use the QD-MLLD as an LO, due to the extra EDFA and TBPF used to boost the power of a single carrier from the QD-MLLD. In Fig. 4.9(c), we provide samples of constellation diagrams for different modulation formats that remain below the FEC thresholds.

Based on our findings, the choice between QD-MLLD and ITLA depends on the specific requirements of the optical communication system, considering factors such as wavelength control, noise performance, and target applications.

4.3.4 Coherent transmission with QD-MLLD and on-chip silicon photonic modulator

We perform coherent transmission with the QD-MLLD and a SiP single-segment IQ modulator. The design and characterization of the SiP have been reported in [2]. Briefly, the SiP is fabricated at AMF using a CMOS-compatible process. It consists of two child MZMs connected in parallel. Each MZM has phase shifters with a length of 4 mm. The child MZMs are configured for a series push-pull configuration, requiring a single RF signal per MZM for operations [150]. A 50 Ω termination is added to each electrode for efficient power

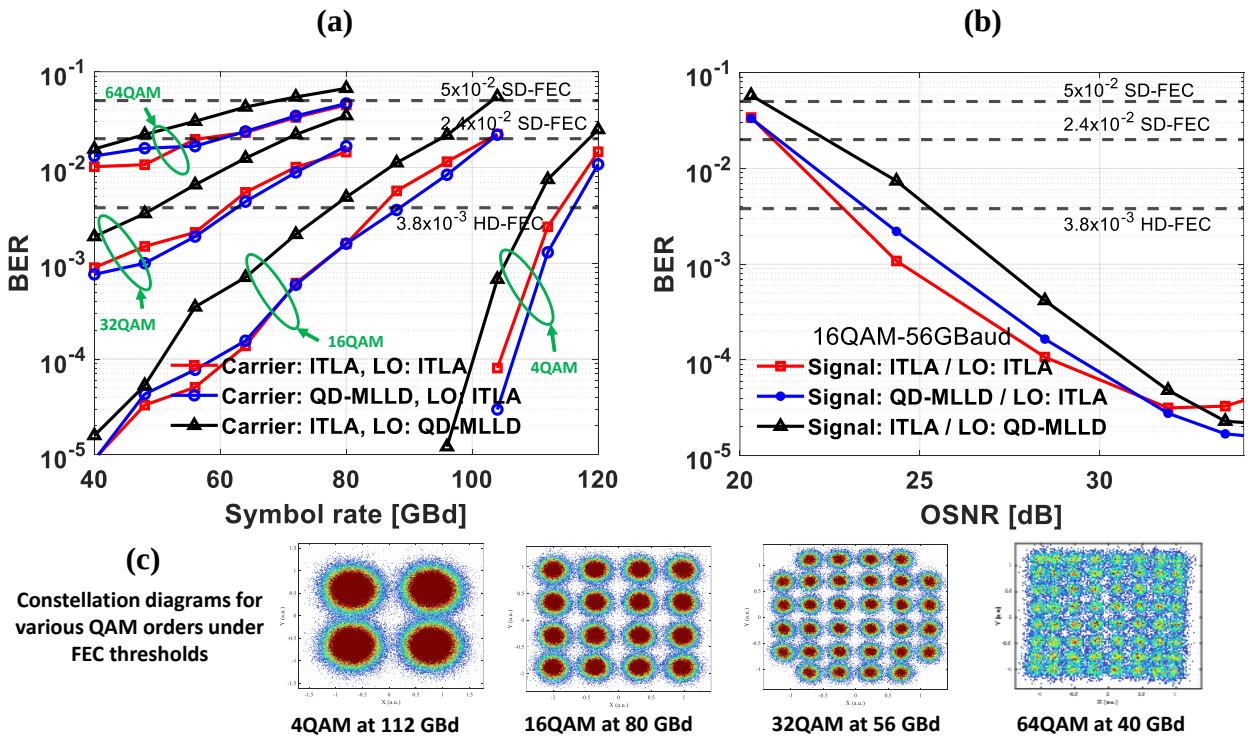

Fig. 4.9 (a) BER versus symbol rate for different modulation formats in three cases: red (ITLA as carrier and LO), blue (QD-MLLD as carrier and ITLA as LO), and black (ITLA as Carrier and QD-MLLD as LO). (b) OSNR measurement for the three cases at 16QAM 56 GBd. (c) Constellation diagrams for modulation formats from 4QAM to 64QAM.

transfer and testing. There are 4 thermo-optic heaters used for biasing the modulator. The measured DC V_π at 0 V reverse bias is 8.5 V, indicating $V_\pi L = 3.4$ V-cm. The small-signal response of the SiP modulator is shown in Fig. 4.10 (b) for different biasing voltages. The modulator has a 3-dB (6-dB) bandwidth of 20 (28.5) GHz without reverse biasing that increases to 28 (38.5) GHz at 3V reverse bias. The inset shows a microscopic image of the fabricated chip along with the FAU and ground-signal signal-ground (GSSG) high-frequency RF probes used in the experiments. VGCs are used to input and output light into the chip. The insertion loss of the modulator is 4.5 dB, and the overall insertion loss including the

VGCs is approximately around 18 dB.

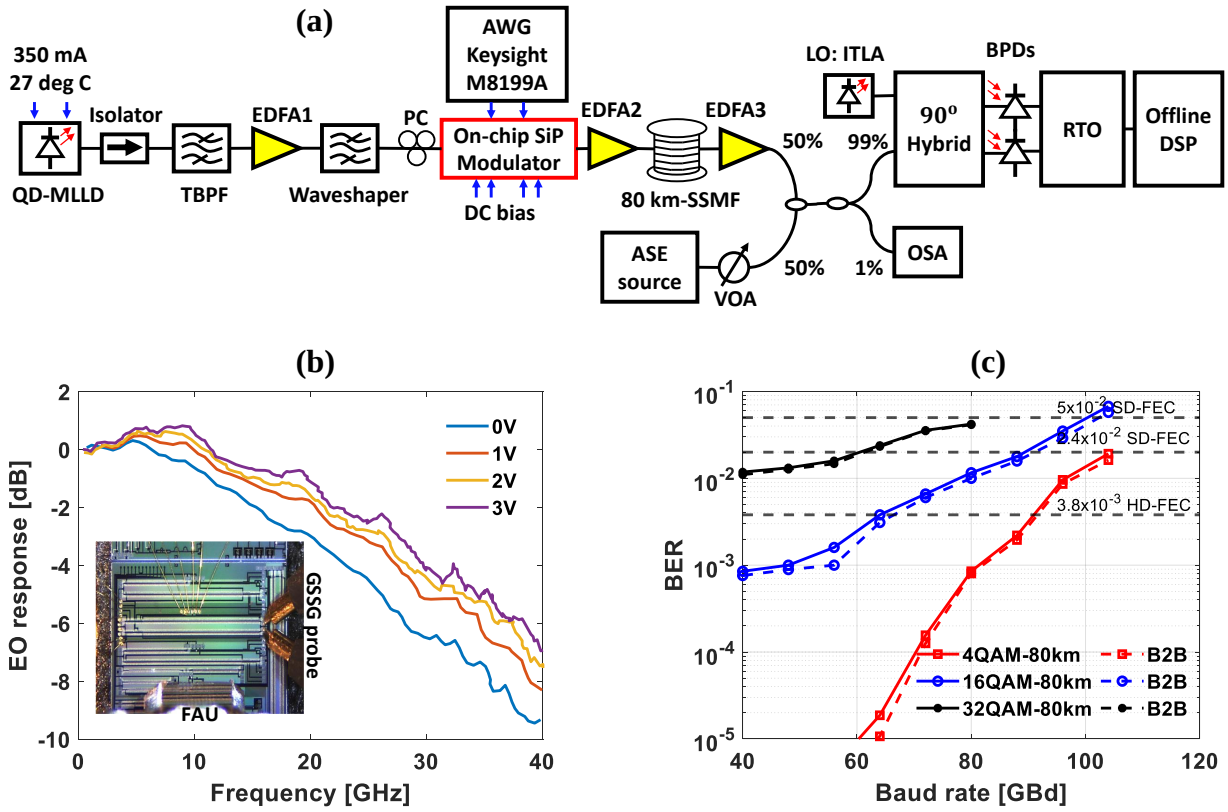

Fig. 4.10 (a) Experimental setup for the coherent transmission experiment with the SiP modulator. (b) The EO response S21 of the SiP modulator, the inset is a microscopic image of the SiP chip [2]. (c) BER as a function of symbol rate for one of the channels of the QD-MLLD with modulation formats ranging from 4 to 32QAM after b2b (dash lines) and 80 km-SSMF (straight lines) transmission.

The experimental setup is shown in Fig. 4.10(a). We use the same equipment and DSP routine illustrated earlier in Fig. 4.6 (a). Fig. 4.10(c) shows the BER results across various symbol rates for one of the channels from the comb source. We achieve symbol rates of up to 88 GBd with 16QAM signaling and 56 GBd with 32QAM signaling, all below the SD-FEC threshold with 20% OH. We achieve maximum symbol rates of 104 GBd with 4QAM and 16QAM signals, and 80 GBd for 32QAM signals, indicating aggregate bit rates of 208 Gb/s,

416 Gb/s, and 400 Gb/s, respectively.

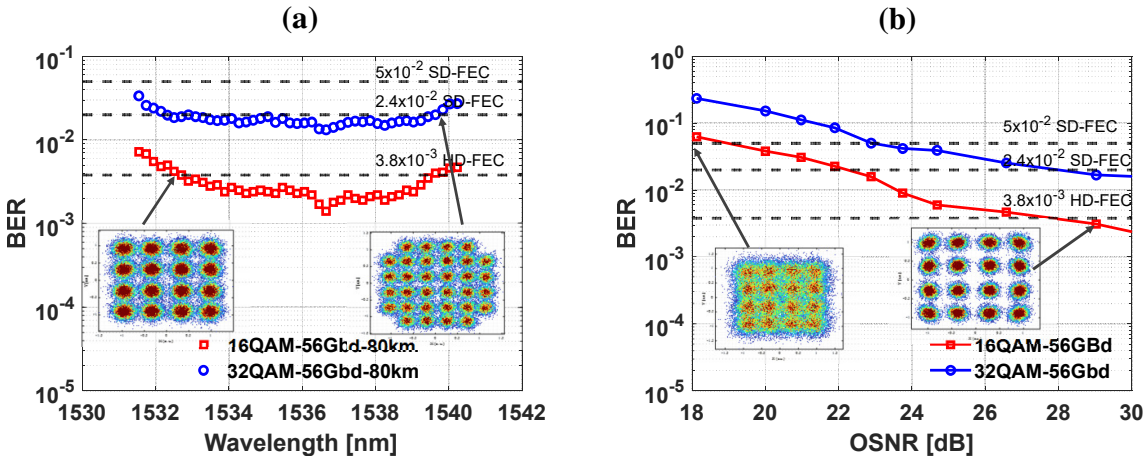

Fig. 4.11 (a) BER as a function of wavelengths of the 45 channels usable for transmission over 80 km-SSMF using 16QAM at 56GBd (red squares) and 32QAM at 56GBd (blue circle). (b) OSNR measurement of one of the QD-MLLD channels with the SiP modulator at 16QAM 56 GBd and 32QAM 56 GBd.

It is important to note that the results are not limited to a single wavelength as in [2]. Again, we conduct comprehensive WDM experiments, ensuring consistent and robust performance across all lines from the QD-MLLD with the SiP modulator. Fig. 4.11(a) provides an overview of the performance of all channels from the comb source using the SiP modulator. All channels demonstrate consistent performance, underscoring the stability of both the comb source and the SiP modulator across multiple wavelengths. We test each channel using 16QAM and 32QAM at 56 GBd. As observed earlier, channels at the edges exhibit somewhat diminished performance due to lower peak power-to-noise ratios; nevertheless, their BER values remain below the SD-FEC threshold with 25% OH (BER $< 5 \times 10^{-2}$). Furthermore, we measured the BER as a function of OSNR measurements to further evaluate the combined performance of the SiP modulator and the QD-MLLD. Fig. 4.11(b) summa-

rizes these results for 56 GBd using 16QAM and 32QAM. The corresponding BER values for OSNR of 22 dB and higher are below the SD-FEC threshold with 25% OH for 32QAM signaling and below the SD-FEC threshold with 20% OH for 16QAM signaling. The highest aggregate data rates achieved using the SiP modulator and QD-MLLD are 208, 416, and 400 Gb/s on a single polarization. Again, it is important to mention that these results are primarily limited by the bandwidth limitations from the SiP modulator, AWG, RTO and BPDs. The SiP modulator also has a nonlinear transfer function that affects high-order QAM modulation formats. However, our findings suggest that improvements in AWG can empower a low bandwidth IQ modulator to function beyond 100 GBd. This is attributed to the slow roll-off frequency response of the modulator as illustrated in Fig. 4.10 (b).

4.4 Summary

Our study demonstrates the remarkable efficiency and robustness of the QD-MLLD in coherent WDM transmission over 80 km of SSMF. It highlights the QD-MLLD's superior frequency and phase noise performance, enabling coherent transmission with high modulation formats and symbol rates. The QD-MLLD, as a comb source, offers several advantages such as emitting a broadband comb spectrum while requiring only a single DC supply, and the compact size. QD-MLLD generates ultrashort pulses and has relatively narrow optical and RF linewidth.

Although our system utilizes a single polarization scheme due to limitations of the SHF QAM transmitter and the SiP modulator, it can be readily upgraded to a dual-polarization setup, effectively doubling the net bit rates achieved. All the measured BER values across the comb source channels consistently fall within acceptable FEC thresholds. We demonstrate

the QD-MLLD's flexibility by showcasing that it can be programmed using a programmable optical filter to manipulate the frequency spacing between the comb lines, to match the target application requirements. Additionally, our findings indicate that the QD-MLLD can perform both as LOs and signal carriers, and its performance closely matches that of the commercial narrow-linewidth ITLA, further emphasizing its competitive edge.

Another notable aspect is the potential for hybrid integration with silicon photonics. Our transmission experiments successfully demonstrate that the QD-MLLD can function very well with a SiP modulator, opening doors and marking a promising future for hybrid integration in optical transceiver modems for coherent optical communication systems, whether for short or long-distance fiber transmissions. Our study culminates in the impressive achievement of utilizing the QD-MLLD to attain a high modulation format of 64QAM at an impressive symbol rate of 80 GBd, resulting in a net bit rate of 447.8 Gb/s per line.

Chapter 5

Securing Data Transmission in Coherent Optical Communications

In the previous chapter, we have seen how QD-MLLDs function very well in coherent communication systems and allows high-capacity and high-speed optical transmission for data rates beyond Tb/s. However, coherent transmission systems require protection against eavesdropping attacks. Nowadays, eavesdroppers can easily obtain fiber-tapping tools and tap into a fiber link to get access to confidential data. This data could be information about patients in hospitals, bank card information, or any sensitive data. Therefore, in this chapter, we demonstrate novel encryption techniques to secure the existing optical fiber links.

The work in this chapter is based on collaboration projects with Quantropi Inc. and our publications in [151–158]. We have adjusted our work to align with the structure and notations used in this thesis.

5.1 Introduction

To satisfy the increasing demand for data confidentiality and authenticity, it is important to ensure that communications are being properly secured. Since optical communication links have evolved from conventional applications in telecommunications to become the preferred infrastructure for transmitting substantial amounts of information, extensive research has been investigated to improve the optical networks' performance. These improvements include spectral efficiency, data rate, and DSP speed [159, 160]. In long-haul optical fiber transmission, eavesdropping attacks are more likely to occur, wherein an eavesdropper can steal optical signals by tapping into the physical transmission links [161–163]. Various encryption techniques have been proposed and investigated to enhance the secrecy of information in fiber networks including QKD [164], optical chaos-based communications [165], optical steganography [37, 166], and XOR encryption [38, 167].

QKD can be achieved by encrypting the key information in the quantum states of a single photon, this is now known as the BB84 protocol [168]. QKD has the advantage of indicating whether an eavesdropper is trying to get the key information or not. However, QKD requires specialized infrastructure, including a single photon transmitter, detector, and quantum communication channels. QKD also has limited communication distance and low data rates [169].

Optical chaos-based communication can be seen as a jamming signal over an information signal. On the transmitter side, the information signal is coupled into a fiber loop and amplified by an EDFA, while on the receiver side, the chaotic signal is split and one of the taps goes through an open loop to regenerate the chaos, and the other tap is launched into a photodetector. To decrypt the signal correctly, the EDFA on the receiver side must

match with the one on the transmitter side [170–172]. The chaotic signals generated by such systems are not truly random, which can make them more susceptible to eavesdropping attacks by adversaries who can predict the behavior of the system.

Optical steganography is based on hiding the information signal in public channels, preventing eavesdroppers from detecting the stealth signal [37,173]. One of the optical steganography techniques is done by using a temporal phase mask to encode the information signal by spreading the signal through CD, and only the right dispersion compensation receiver can decode the stealth signal correctly. However, data rates beyond 10 Gb/s remain a challenge in optical steganography [174].

Optical XOR gates have been recently investigated due to their high-speed encryption and electromagnetic wave immunity. However, the implementation of XOR gates requires special infrastructure and is limited in terms of transmission distance [38, 175].

In this chapter, we present a comprehensive exploration of innovative encryption techniques with quantum-inspired principles, designed for the existing optical fiber links. First, we demonstrate an encryption approach based on a round-trip mechanism, wherein no additional parties are required to have information about the secret key or the so-called codeword. The encryption is done using an external PM driven by an independent AWG, while decryption occurs within the receiver's DSP framework. Second, we demonstrate a one-way transmission system, and the information is encrypted using a Displacement Operator in Coherent States (DOCS). In this approach, both encryption and decryption operations are conducted within the transmitter and receiver DSP, respectively. Lastly, we showcase a novel dual polarization encryption method, wherein X-polarized symbols undergo encryption with a distinct codeword compared to Y-polarized symbols. We demonstrate thorough theoretical

examination and are experimentally validated over an 80 km span of SSMF at an impressive aggregate bit rate of up to 580 Gb/s, utilizing a 32QAM format. The measured BER values consistently fall below the SD-FEC threshold.

5.2 Encryption based on randomized phases in phase space

The work in this section builds upon our theoretical and experimental results published in [151, 154–157], with additional details.

Although this thesis does not focus on quantum theory, we would like to highlight the quantum distinguishability because our encryption technique is quantum-inspired based on the B92 protocol [176]. In quantum mechanics, it is not always possible to distinguish between arbitrary states. For example, there is no process allowed by quantum mechanics that will reliably distinguish between the states $|0\rangle$ and $(|0\rangle + |1\rangle)/\sqrt{2}$. Suppose, we try to distinguish the two states by measuring in the computational basis (states $|0\rangle$ and $|1\rangle$ are known as a computational basis):

1. If we have been given the state $|0\rangle$, the measurement yields 0 with probability of 1.
2. However, when we measure $(|0\rangle+|1\rangle)/\sqrt{2}$, the measurement yields 0 with probability of 1/2 and 1 with probability 1/2

Thus, while a measurement result of 1 implies that the state must have been $(|0\rangle+|1\rangle)/sqrt2$, since it could not have been $|0\rangle$, we cannot infer anything about the identity of the quantum state from a measurement result of 0. Therefore, a quantum state contains hidden information that is not accessible to measurement and thus plays a key role in quantum algorithms

and quantum cryptography [177, 178]. The roundtrip mechanism in a coherent transmission system is based on adding an ambiguous phase signal to the channel that is only known by the transmitter, Bob, while another authenticated user, Alice, adds the sensitive information signal into it. In this case, only Bob can distinguish and inverse the phase signal to extract Alice's information signal.

The theoretical roundtrip mechanism in coherent communication systems, as demonstrated in [151] for quantum-inspired encryption, introduces a key principle where the transmitter (Bob) doesn't need to share key information with other entities. The following steps demonstrate the main aspects of the encryption and decryption process:

1. On the transmitter side, an authenticated user, Bob, generates a phase-modulated signal using a random phase mask known only to him.

2. The encrypted signal is transmitted to another authenticated user, Alice, through a public fiber channel.

3. Alice incorporates her information signal into the phase-encrypted signal and transmits it back to Bob over another public fiber channel. The phase-encrypted signal acts as an envelope for Alice's information signal.

4. Only the authenticated user, Bob, possesses the capability to decrypt the phase information using the reverse of the phase mask. Then, he can decode Alice's signal using typical coherent receiver DSP techniques.

5.2.1 Operating principle

The primary objective of any encryption technique is to protect sensitive data against eavesdroppers and facilitate the extraction of information exclusively at the receiver's end. Adversaries attempting to tap into the fiber channel should not be able to extract any information. For our roundtrip encryption approach, assume the electric field of a CW, at Bob transmitter, is expressed as follows:

$$E_{Bob,Tx}(t) = E_0 . e^{j(2\pi f_c t + \phi_0)} \tag{5.1}$$

where E_0 is the amplitude of the electric field, f_c is the carrier frequency of the laser beam, ϕ_0 and is the phase offset. We modulate the CW beam with a phase modulation signal $P(t)$ in exponential form, then the output electric field is given by:

$$E_{Bob,Tx}(t) = E_0 . e^{j(2\pi f_c t + \phi_0)} . e^{jP(t)} \tag{5.2}$$

The AWG, responsible for driving the PM, generates a random electrical signal denoted as $mod(t)$, and its amplitude is adjusted by an RF amplifier and an RF attenuator. This electrical signal induces random phase changes in the PM, switching between two or four phases denoted as $\Delta\varphi_m$. For instance, a set of random phases could include $0, \pi/4, 3\pi/4$, and π, or simply 0 and π. The output of the PM can now be expressed as follows:

$$E_{Bob,Tx}(t) = E_0 . e^{j(2\pi f_c t + \phi_0)} . e^{j\Delta\varphi_m \, mod(t)} \tag{5.3}$$

This signal, now carrying random phases, is transmitted to Alice over an optical fiber channel. Assuming the impulse response of the first fiber channel is denoted as $f_{fiber,1}(t)$, Alice will

receive a signal expressed as follows:

$$E_{Bob,Tx}(t) = E_0 . e^{j(2\pi f_c t + \phi_0)} . e^{j\Delta\varphi_m \, mod(t)} \otimes f_{fiber,1}(t) \tag{5.4}$$

Alice now modulates this signal using an IQ modulator driven by an independent AWG. Assuming Alice employs a QAM modulation format with a general formula, she then transmits the signal back to Bob over another fiber channel with an impulse response denoted as $f_{fiber,2}(t)$. The received signal at Bob's receiver can be expressed as follows:

$$E_{Bob,Rx}(t) = \{E_0 . e^{j(2\pi f_c t + \phi_0)} . e^{j\Delta\varphi_m \, mod(t)} \otimes f_{fiber,1}(t)\} . s_{QAM}(t) \otimes f_{fiber,2}(t) \tag{5.5}$$

A demonstration of this process is shown in Fig. 5.1. From Eq. 5.5, it is evident that

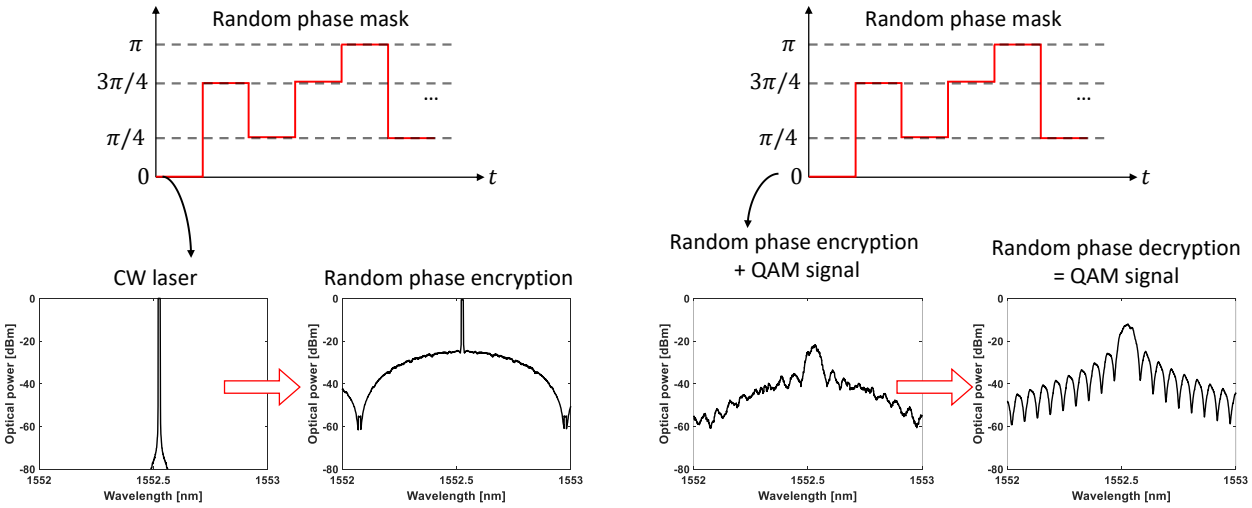

Fig. 5.1 A demonstration of random phase mask encryption and decryption over a QAM signal.

decoding Alice's signal requires decrypting the random phase mask first. Otherwise, the phases of the QAM symbols become randomly mixed in the phase space with the phase mask signal. A QAM signal, denoted as $s_{QAM}(t) = I(t) + j\,Q(t)$, consists of $I(t)$ and $Q(t)$,

representing the in-phase and quadrature components of the modulating signal, respectively. The in-phase component, $I(t)$, and the quadrature component, $Q(t)$, are two independent signals typically used to encode separate sequences of digital information, defined as follows:

$$I(t) = \sum_{i=1}^{n} a_i \,.\, \cos(2\pi f_{\text{symbol}} t - \phi_i) \tag{5.6}$$

$$Q(t) = \sum_{i=1}^{n} a_i \,.\, \sin(2\pi f_{\text{symbol}} t - \phi_i) \tag{5.7}$$

where, n is the number of symbols in the QAM constellation, a_i represents the amplitude of the i-th symbol, f_{symbol} is the symbol rate, and ϕ_i is the phase of the i-th symbol. It is clear that without the correct phase mask, one cannot differentiate between QAM symbols.

As there are two independent AWGs, one for phase mask encryption and another for QAM modulation, symbol synchronization plays a crucial role in the decryption process. It is important to note that these AWGs are physically distant from each other, making the use of traditional synchronization techniques like an external clock or trigger synchronization impractical. Consequently, Bob must incorporate a pilot signal or reference signal into the phase mask stream to achieve synchronization.

In Fig. 5.2, we present a flowchart outlining the synchronization process. Initially, Bob receives the encrypted signal containing Alice's information. Then, he applies the phase mask—known only to him—to the original sequence and attempts to demodulate Alice's information signal. Successful synchronization is indicated by the expected BER falling below the FEC thresholds. At this point, Bob can extract Alice's information signal and implement the necessary DSP optimization steps. If the received symbols are not synchronized with the phase mask sequence, the phase mask sequence is shifted by one symbol, and the process is repeated until synchronization is achieved.

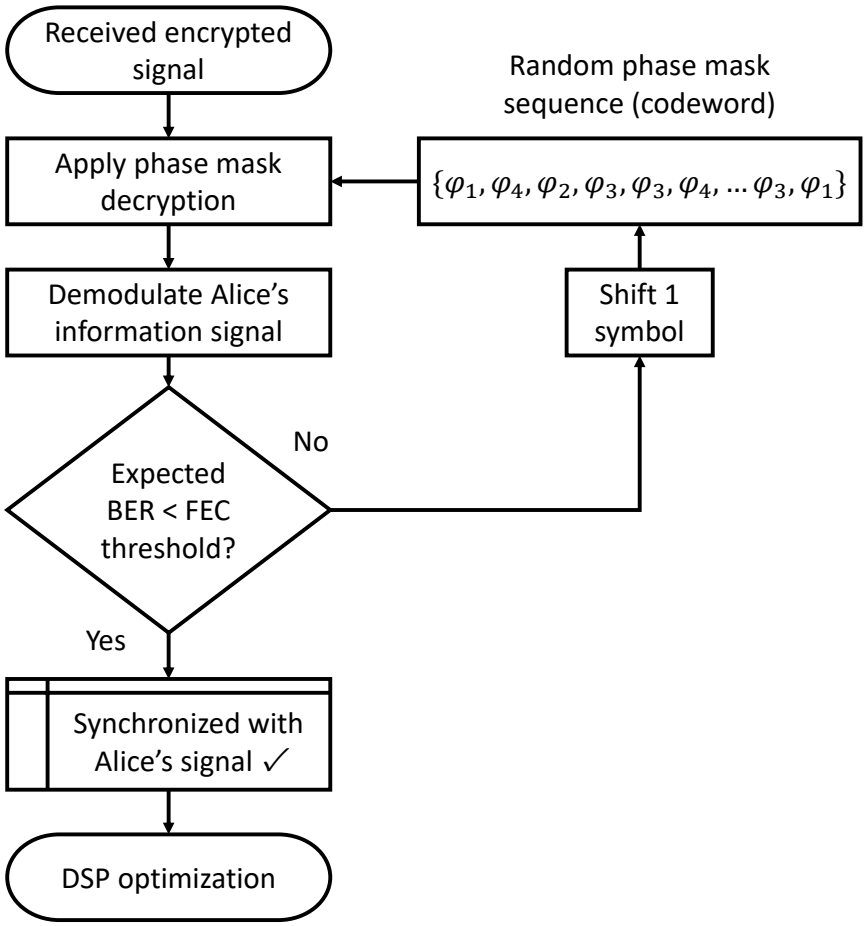

Fig. 5.2 Flowchart depicting the synchronization between the phase mask on Bob's receiver side and the QAM modulation signal from Alice.

Since the phase mask consists of a series of random phases, fluctuating randomly among four different values (φ_1, φ_2, φ_3, φ_4), Bob needs to perform the synchronization process every time he receives a signal from Alice. This step is crucial because phase masks are random and can change frequently during transmission and reception. We emphasize that Bob does not need to share the phase mask (codeword) with any other parties, marking a significant contribution to our approach. Given that this encryption primarily operates in the phase space, we denote it as Encryption in Phase Space (EPS). In the next section, we experimentally validate the EPS technique in a roundtrip coherent transmission system.

5.2.2 Experimental setup and results

Fig. 5.3 illustrates the experimental setup of the roundtrip mechanism and DSP routines. At Bob's transmitter, a μITLA is employed as the primary light source for the entire transmission. The selection of a narrow-linewidth laser source is crucial to minimize fiber nonlinearity. The μITLA boasts a linewidth of less than 100 kHz and a maximum output power of 14 dBm. The output from the μITLA undergoes modulation through a PM. The PM features an insertion loss of 4.1 dB, a V_π of 2.4 V, a polarization crosstalk of 25 dB, and a 3 dB bandwidth of 25 GHz. On the electrical side, a DAC, an RF amplifier, and an RF attenuator are used to drive the PM with the electrical signal used for encryption. The generation of the random phase mask involves several steps: random symbols are generated with the insertion of a pilot signal to facilitate synchronization. The following processes include upsampling, RRC pulse shaping, resampling, clipping, and quantization to match the DAC1 sampling rate (88 GSa/s). The initial phase of the PM, denoted as $\Delta\varphi_m$, is controlled by the RF amplifier and the RF attenuator. The random phase modulated signal is then transmitted over 80 km of SSMF (Spool 1), and the optical power is boosted using EDFA1 up to 10 dBm to align with the dual polarization IQ modulator on Alice's side.

At Alice's transmitter, a dual-polarization IQ modulator is employed to incorporate Alice's information signal with the phase-modulated signal, which now serves as an envelope for Alice's information. On Alice's electrical side, DAC2 operates at a sampling rate of 70 GSa/s. Alice employs a standard DSP routine for a QAM modulation signal. This routine includes mapping the source data to the desired QAM modulation format, followed by processes such as upsampling, RRC pulse shaping, resampling, clipping, and quantization. Then Alice transmits the signal back to Bob through another 80 km of SSMF (Spool 2).

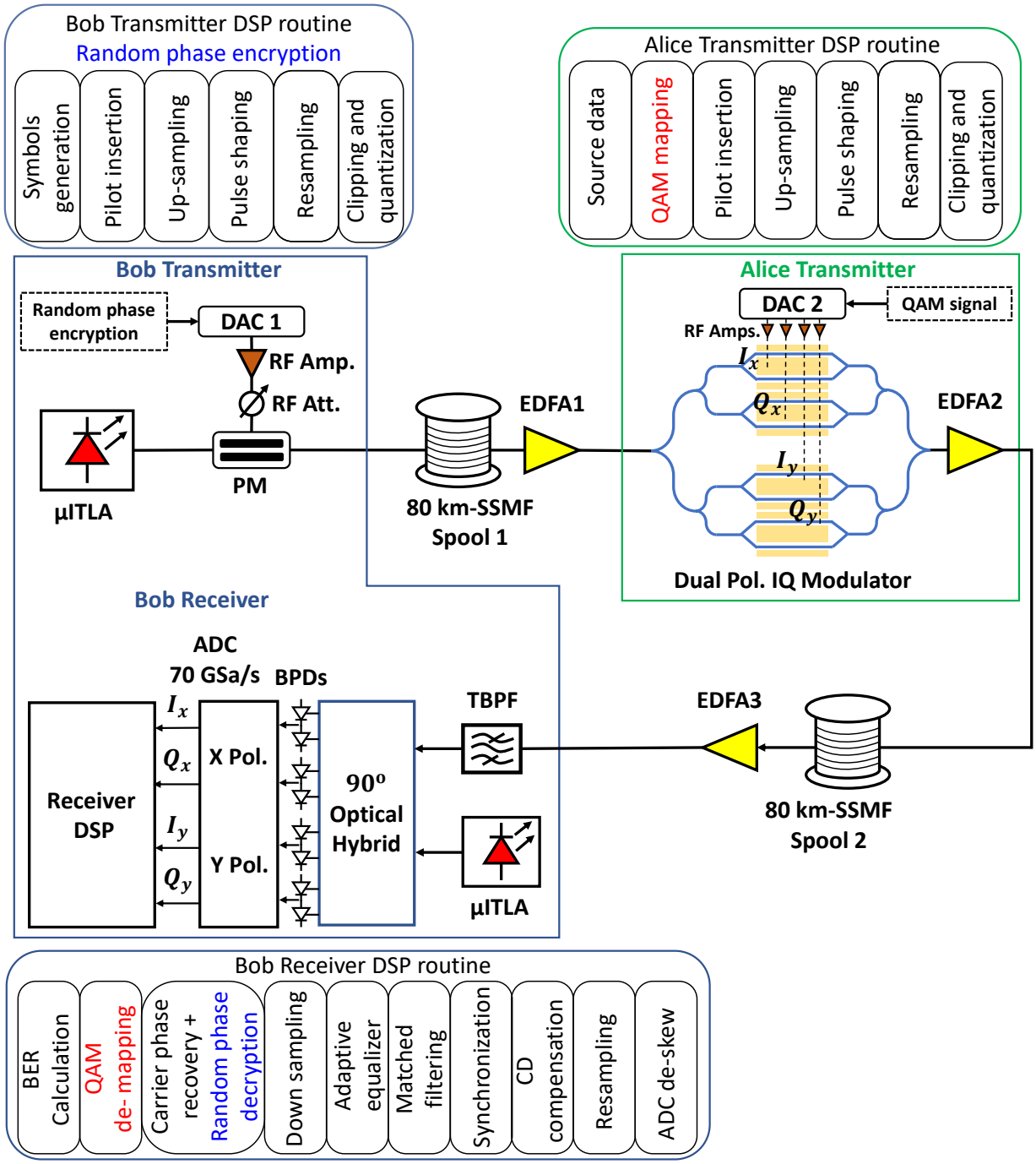

Fig. 5.3 Experimental setup for the round-trip mechanism employing random phase encryption using an external phase modulator and DSP routines.

At Bob's receiver side, a TBPF is used to filter out ASE noise, and the received encrypted signal is launched into a 90^o optical hybrid. This signal is then mixed with another μITLA serving as a LO. The optical signal is converted to an electrical signal using BPDs. An ADC operating at the same sampling rate as DAC2 (70 GSa/s) is employed to capture the signal. The receiver DSP undergoes several steps. First, ADC de-skew to compensate for the mismatching between the in-phase, $I(t)$, and quadrature, $Q(t)$, components. Then, resampling to match DAC2 sampling rate, and CD compensation to compensate for the roundtrip fiber length. A synchronization step is crucial to synchronize with Alice's signal, which is phase-encrypted. Then, matched filtering and adaptive equalizer are applied to maximize the SNR and mitigate the effects of channel impairments, respectively. The flowchart presented in Fig. 5.2 is then employed along with the BPS carrier phase recovery algorithm to decrypt the random phase mask and recover the phases of the QAM symbols to extract Alice's information signal. Again, the exact phase mask needs to be applied to demodulate Alice's signal successfully.

In our experiments, we use the QPSK modulation format with a symbol rate of 50 GBd, resulting in an aggregate data rate of 200 Gb/s. It is important to remember that the initial phase of the PM, denoted as $\Delta\varphi$, varies with the RF power driving the PM. We control $\Delta\varphi$ using an RF attenuator. We determine the value of $\Delta\varphi$ empirically. For each value of $\Delta\varphi$, we applied the synchronization flowchart presented in Fig. 5.2. It is crucial to note that the length of the phase mask series is constrained by the DAC memory; in our case, the DAC memory length is 2^{16} symbols. Initially, during the experiment's outset, we used a repetition of four phase values throughout the entire memory, facilitating quicker synchronization. Once the validation of our encryption technique was confirmed, we transitioned to utilizing the full memory length with random phase values.

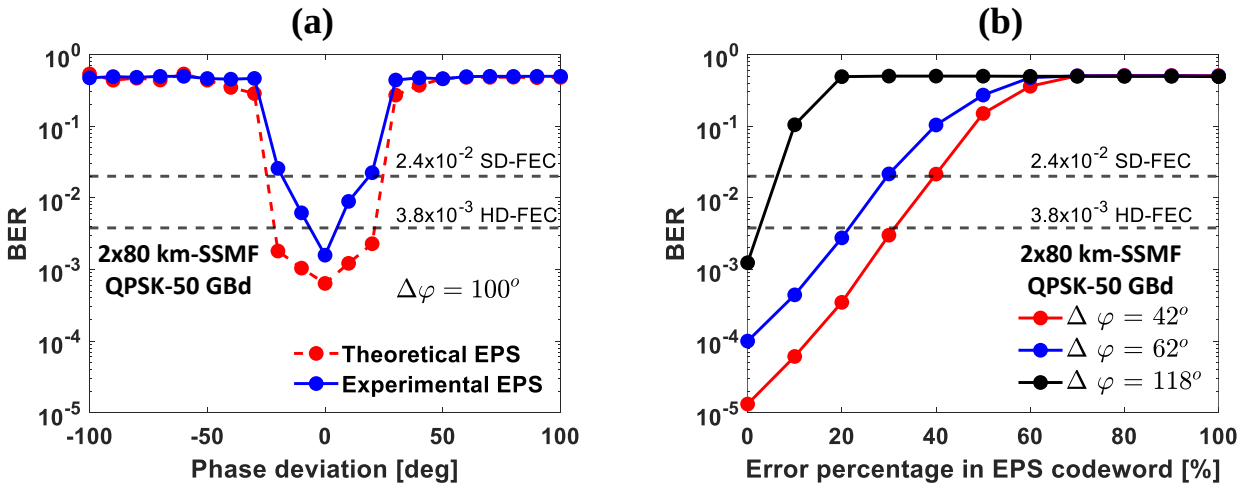

Fig. 5.4 (a) Measured and simulated BER as functions of phase deviation in a roundtrip transmission system. (b) Experimental results of the roundtrip mechanism utilizing a phase modulator with 4 random phase levels: BER as a function of the error percentage in the codeword.

Fig. 5.4 (a) presents the experimental and theoretical BER values as a function of phase deviation with a $\Delta\varphi$ of 100^o, calculated empirically. In this scenario, synchronization is successfully achieved, allowing the use of the exact codeword for decryption. Therefore, we investigate the influence of varying the overall phase deviation. The theoretical analysis indicates a $\pm 20^o$ phase tolerance, while the experimental results demonstrate that phase deviations exceeding 5^o cause the BER to rise above the HD-FEC threshold. Beyond approximately 20^o, the BER surpasses the SD-FEC threshold.

In Fig. 5.4 (b), the experimental results show the BER values concerning the error percentage in the EPS codeword, namely, the phase mask series. The investigation includes three distinct initial phase values: 42^o, 62^o, and 118^o. It is assumed that adversaries can achieve synchronization but cannot accurately guess the exact codeword employed for encryption. The conducted experiments reveal that the information signal can still be extracted despite errors in the codeword, particularly for specific initial phase values, such as $\Delta\varphi$ of

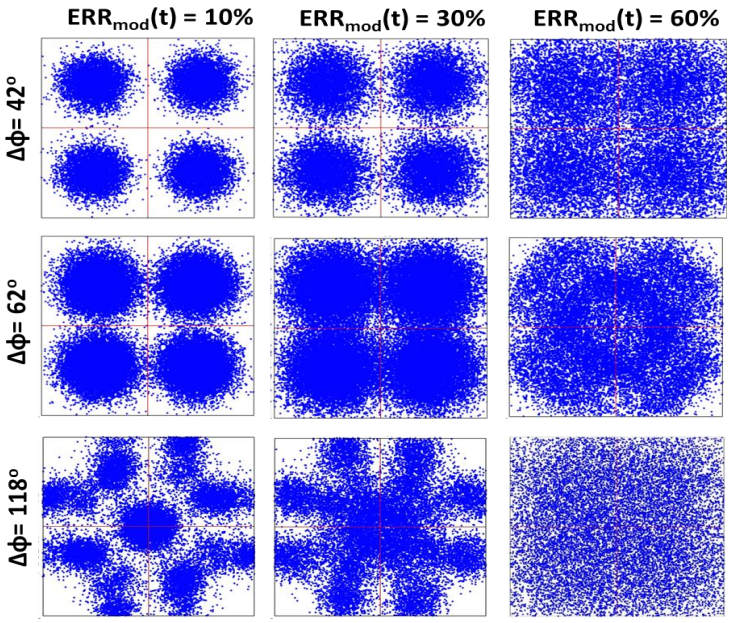

Fig. 5.5 Constellation diagrams of QPSK in the roundtrip mechanism with an external phase modulator for various phase deviations and error percentages in the used codeword.

42^o. The error percentage in the codeword remains tolerable for $\Delta\varphi$ of 42^o, reaching up to 40% before hitting the SD-FEC threshold. On the contrary, for higher initial phase values, like when $\Delta\varphi$ is 118^o, the error percentage in the codeword reduces to 7%. This observation emphasizes the critical role played by the initial phase in the encryption process. Therefore, a careful selection of the initial phase can enhance the robustness of the encryption scheme, allowing for a lower tolerance of errors in the EPS codeword while maintaining BER values within acceptable limits.

The corresponding constellation diagrams are presented in Fig. 5.5 for QPSK modulation format signal at a symbol rate of 50 GBd after 2×80 km of SSMF transmission.

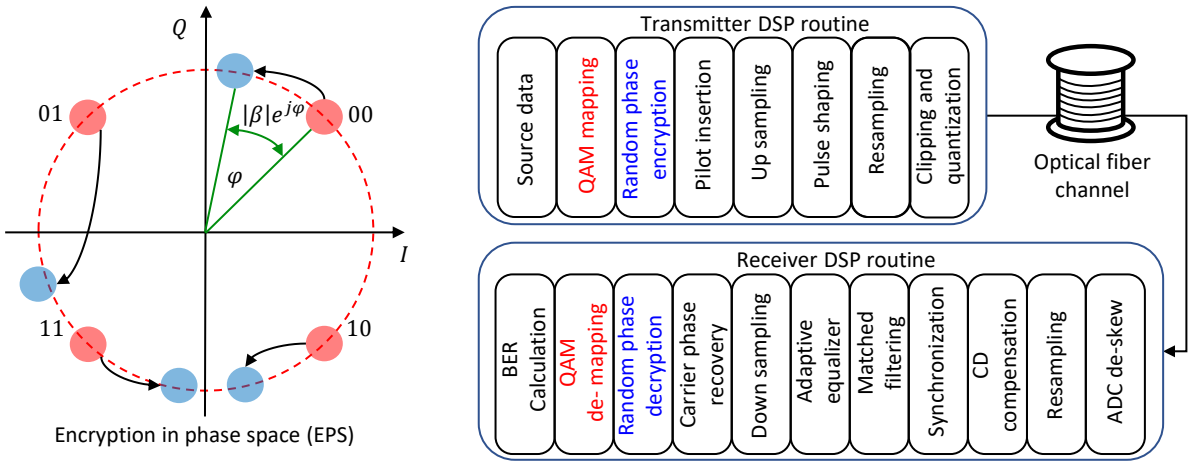

Fig. 5.6 Illustration of the EPS encryption technique and the DSP routine in one-way coherent optical transmission system.

5.2.3 Discussion

As we notice, the roundtrip encryption mechanism system is complex and requires a long process of synchronization in the DSP. This process can be eliminated by introducing another PM before the 90^o optical hybrid to inverse the phase mask introduced by the first PM. However, this process requires careful investigation to estimate the initial phase for the first modulator and apply the inverse of it for the second one. Although the roundtrip encryption mechanism might not be as practical as one-way transmission systems, it provides significant data confidentiality since the authenticated transmitter does not share the codeword with any other entities. In eavesdropping attacks, where an eavesdropper taps into the fiber link to extract sensitive information, adversaries should have complete knowledge of the codeword and synchronization to decrypt the information signal. The advantage of this technique is that Bob does not share the codeword with any other entities, therefore, the codeword can be changed frequently for every reception form Alice.

The codeword values are not constrained to $0, \pi/4, 3\pi/4, \pi$; it could consist of any random phase values filling up the DAC memory. In other words, the codeword can contain 2^{16} random phase values. However, this further complicates the synchronization process.

In case eavesdroppers tap twice into the fiber link or capture the signal to perform parallel phase synchronization, Bob or Alice should monitor the optical power to observe if there is any power drop cause by eavesdroppers after tapping into the fiber link, then they should stop the transmission.

We prove that the EPS encryption can be implemented in one-way transmission, and the corresponding DSP process is illustrated in Fig. 5.6. This process mimics the impact of the PM on QAM symbols. Following QAM mapping, the symbols are rotated randomly in the phase space using a random phase mask, as depicted in Fig. 5.6 (constellation diagram). In the next section, we present the general form of the EPS technique, in which QAM symbols are displaced using random amplitudes and phases. We refer to this encryption technique as encryption based on displacement operators in coherent states.

5.3 Encryption based on displacement operators

5.3.1 Operating principle

An example of a geometric representation based on the DOCS encryption technique for coherent optical transmission is shown in Fig. 5.7. Assume we have typical QPSK modulation format symbols defined in the phase space as illustrated in red dots. After applying the displacement operator, denoted as $\hat{D}(\alpha)$, the symbols are displaced to another position in the phase space as illustrated in blue dots. The $\hat{D}(\alpha)$ displaces any input state $|\alpha\rangle$ to any

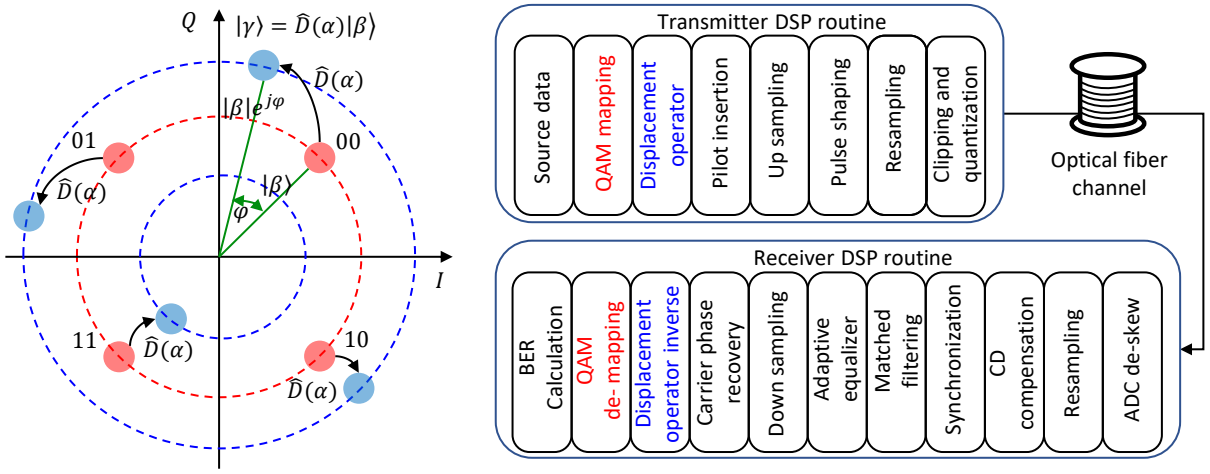

Fig. 5.7 Illustration of the DOCS encryption technique and the DSP routine in transmitter and receiver of a coherent optical transmission system. BER: bit error ratio. CD: chromatic dispersion. ADC: analog-to-digital conversion.

other state $|\beta\rangle$ in the phase space [179]. A phase shift operator $\hat{d}(\alpha = |\beta|e^{j\varphi})$ is a special case of a displacement operator, where symbols are displaced with a fixed amplitude and random phases in the phase space, as we mentioned in the previous discussion. In [158], we proved that the DOCS is a unitary reversible operator. Therefore, applying the displacement operator to a coherent state, and then the inverse of the displacement operator to it returns the coherent state to its original location in phase space. The displacements applied to the information symbols can be completely random in phase space, namely, phases are not just restricted to 0 and π, nor amplitudes are restricted to certain values. Therefore, the number of possible random displacement masks can be vast. For example, if the phase mask has $N = 30$ values, and the phase shifts $\varphi = \pi \times m$, where $m \in (0, 1, 2, ...\, 6)$, then there are 7^{30} possibilities in the random phase mask. The same formula can be used to determine the possibilities in the amplitude variation mask. The total number of possibilities is the summation of the phase and amplitude masks.

The displacement operator in a coherent state can be expressed as follows:

$$\hat{D}(t) = |\beta(t)|\, e^{j(\varphi(t)+\Delta\varphi)} \tag{5.8}$$

where $\beta(t)$ and $\varphi(t)$ are the amplitude variation and the phase deviation applied to the information signal, respectively, and $\Delta\varphi$ is an initial random phase of the displacement operator. Let us assume an information signal, $s(t)$, then, the encrypted information signal can be expressed as follows:

$$s(t)_{En} = s(t) \otimes |\beta(t)|\, e^{j(\varphi(t)+\Delta\varphi)}\, \hat{e} \tag{5.9}$$

where, $\hat{e}$ is the polarization unit vector. The information signal, $s(t)$, can be modulated using any modulation format. In our demonstration, we focus on QPSK and QAM modulation formats. After transmitting the encrypted signal over optical fiber, and assuming the impulse response of the fiber channel is $f(t)_{\text{fiber}}$, the received signal can be expressed as follows:

$$s(t)_{Rx} = s(t)_{En} \otimes f(t)_{\text{fiber}} \tag{5.10}$$

To decrypt the signal, we apply the inverse of the displacement operator to the received signal as follows:

$$s(t)_{De} = \{s(t)_{Rx} \otimes |\beta^{'}(t)|\, e^{-j(\varphi(t)+\Delta\varphi)}\} \otimes f^{'}(t)_{\text{fiber}} \tag{5.11}$$

where $f^{'}(t)_{\text{fiber}}$ is the CD compensation element corresponding to the fiber channel. The amplitude variation codeword, $\beta(t)$, should be chosen carefully to satisfy the power constraint of the system. Symbols with a high Peak-to-Average Power Ratio (PAPR) introduce a larger nonlinear phenomenon and limit the system's performance [180]. The DAC and ADC

operate with a finite Effective Number of Bits (ENoB), which adds quantization noise to the information signal [181]. The phase deviation codeword, $\varphi(t)$, can be chosen randomly as we mentioned earlier. We emphasize this point because such encryption is novel and represents one of our main contributions. In general, high-order modulation formats tend to have a lower tolerance to noise due to the reduction in the Euclidean distance between constellation points. In higher-order modulation formats, more bits are transmitted per symbol, resulting in a denser constellation diagram. Thus, the DOCS encryption technique affects higher-order modulation formats than lower-order ones.

The baseline DSP flow is shown in Fig. 5.7. On the transmitter side, the data source is obtained by generating a Pseudo-Random Binary Sequence (PRBS), which is then mapped into QAM symbols. Then, the generated symbols are processed by the displacement operator encryption scheme. Pilot symbols are appended to the symbols for synchronization. The encrypted symbol sequence is up-sampled to 2 sps, shaped by a RRC pulse filter, and re-sampled to match the DAC sampling rate. On the receiver side, a series of signal processing techniques are applied to ensure accurate reception of the signal before decryption. These techniques include ADC de-skew, resampling, CD compensation, synchronization, matched filtering, adaptive equalization, down-sampling to 1 sps, and carrier phase recovery which is based on the BPS algorithm [182]. Then, the inverse of the displacement operator is applied to decrypt the signal, and symbols are de-mapped into QAM symbols and then bits for BER calculations.

5.3.2 Experimental setup and results

The experimental setup of a secure coherent optical transmission system using the DOCS encryption technique is shown in Fig. 5.8. The transmitter side comprises a μITLA, a DAC, a DP-IQM, and an EDFA. The μITLA generates light at a wavelength of 1550 nm, and the DP-IQM modulates the optical signal with the encrypted mapped and pre-emphasized data sequence. Both polarizations are encrypted using the same displacement operator. The sampling rate of the DAC and ADC is the same and approximately 70 GSa/s with 8-bit resolution. The DP-IQM has 4 channels representing IQ and dual polarization status and are organized in order as XI, XQ, YI, and YQ, respectively. Then, the optical signal is amplified with an EDFA before it is launched into the 80-km of SSMF. On the receiver side, a typical coherent detection system is used. A μITLA is used as a LO and mixed with the encrypted signal through a 90^o optical hybrid. The beating signal is detected by BPDs, and the electrical signal is captured for signal processing. The transmitter and receiver DSP steps to employ the DOCS encryption and decryption technique are illustrated in Fig. 5.7.

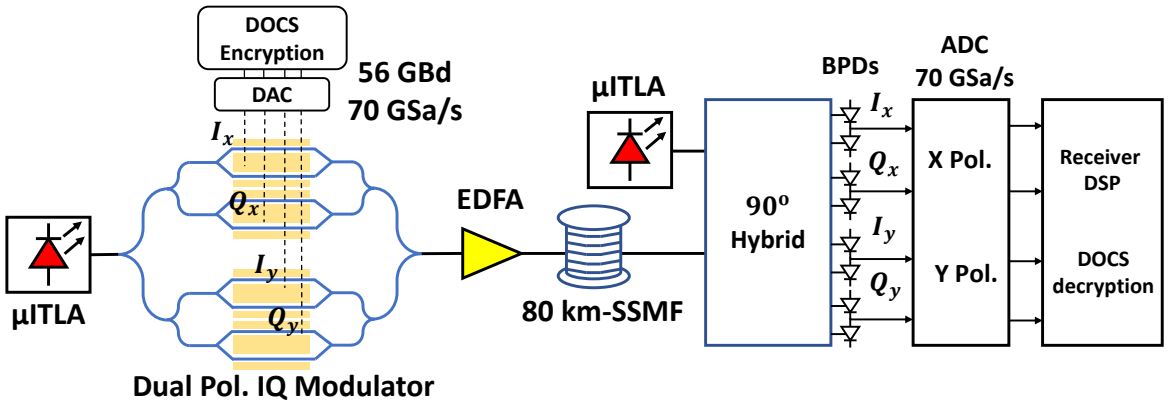

Fig. 5.8 The experimental setup of the DOCS encryption technique in a typical coherent optical transmission.

To assess the performance of the DOCS encryption technique, first, spectra, and his-

tograms are calculated at the transmitter side with and without the DOCS encryption technique. Then, BER analyses are presented for each case at different codeword symbol shifts, phase deviations, and Received Optical Power (ROP) over 80-km SSMF transmission. We also investigate the performance of the system when two random displacement operators are applied to the two polarization states, X and Y, separately.

5.3.3 Loaded electrical signals characteristics

The double-sideband spectra of QPSK, 16QAM, and 32QAM before and after pre-emphasizes are shown in Fig. 5.9 (a) and (b), respectively. The double-sideband spectra are obtained by Fast Fourier Transform (FFT) of the data sequence of the corresponding modulation format. Fig. 5.9 row (c) represents cumulative distribution histograms of a typical QPSK, a QPSK with the DOCS encryption technique applied to the two polarization states, a QPSK with two random displacement operators each applied to X-Y polarization states and QPSK quantified cumulative distribution histogram, respectively. Fig. 5.9 rows (d) and (e) represent the same thing for 16QAM and 32QAM modulation formats, respectively. These histograms are important to show the penalty of signal qualities with and without the DOCS encryption technique. Reduced signal qualities come as a trade-off for high-level signal encryption.

5.3.4 Performance evaluation of the DOCS encryption technique

We evaluate the system performance with and without encryption to better assess the penalty of applying the DOCS encryption technique. The experimental results presented in this section are dual-polarization at 56 GBd after 80-km SSMF transmission. The aggregate

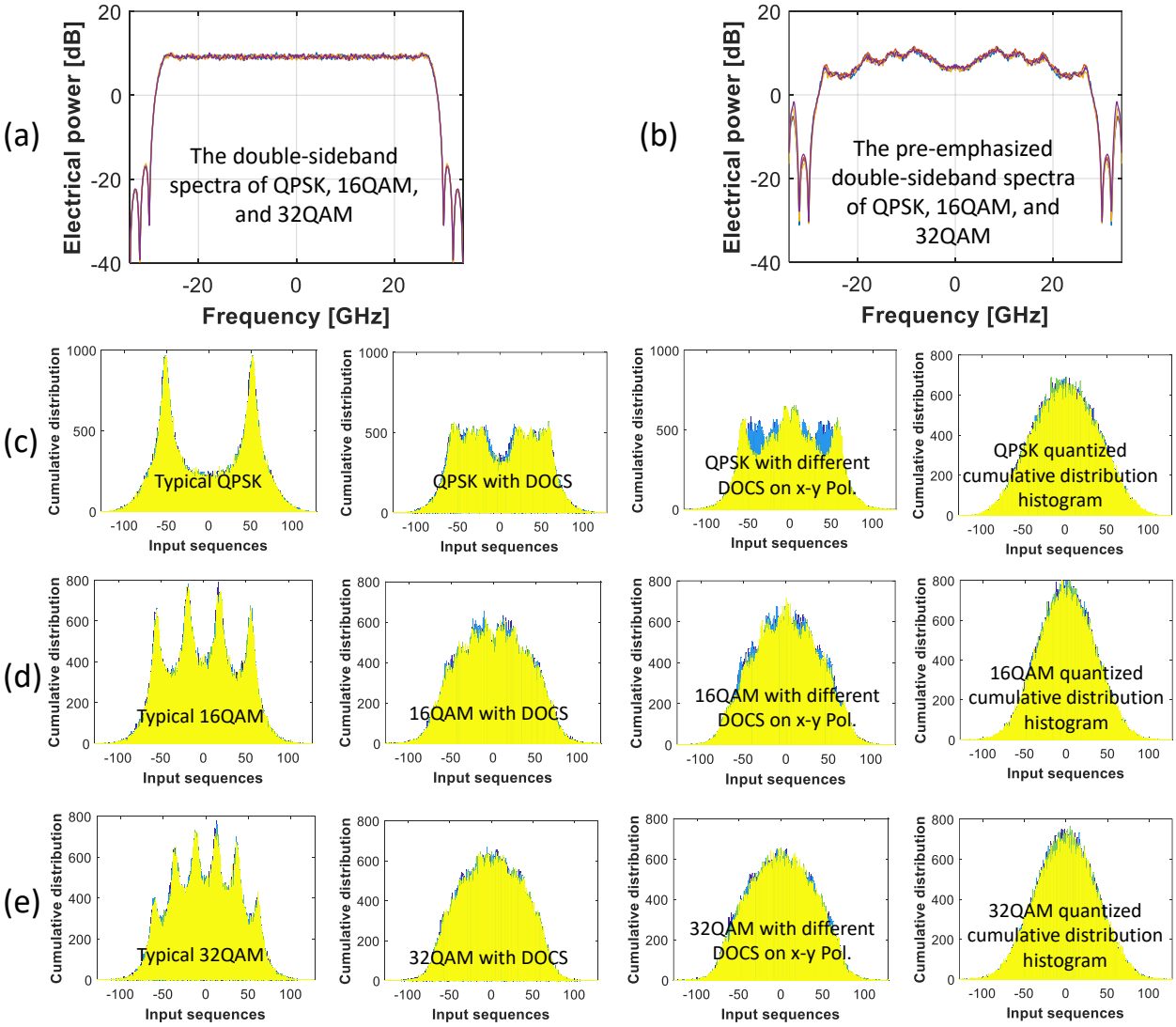

Fig. 5.9 (a) The double-sideband spectra, and (b) the pre-emphasized double-sideband spectra of transmitted QPSK, 16QAM, and 32QAM. Rows (c), (d), and (e) represent the cumulative distribution histogram of a typical QAM modulation format, QAM with DOCS encryption technique, QAM with different DOCS encryption employed on the X and Y polarization states, and the corresponding quantified cumulative distribution for QPSK, 16QAM, and 32QAM, respectively.

bit rates achieved are 224, 448, and 560 Gb/s for QPSK, 16QAM, and 32QAM modulation formats, respectively.

Fig. 5.10 (a) shows the average BER as a function of ROP for QPSK, 16QAM, and 32QAM with (straight lines) and without (dashed lines) employing the DOCS encryption technique. As expected, there is a noticeable degradation in performance compared to the case without encryption. However, most of the points scored BER values below the SD-FEC threshold 2.4×10^{-2}. For ROP > -20 dBm, QPSK and 16QAM scored BER lower than the HD-FEC threshold 3.8×10^{-3}. In general, the trade-off in using higher-order modulation formats like 32QAM is that they offer higher data rates, but they are more sensitive to noise including, but not limited to, DAC, ADC, RF amplifiers, and BPDs. In the ROP analysis, the encryption and decryption are considered to be matched and synchronized. The constellation diagrams of QPSK, 16QAM, and 32QAM are shown in Fig. 5.11 column 1 (correct decryption). Since we use a pilot signal to help with symbol synchronization, it becomes impractical for the adversary to find the right synchronization between the transmitted and received symbols, assuming the adversary has complete knowledge of the transmitted data and the codeword used for encryption.

For an eavesdropper to decrypt the signal correctly, the exact codeword must be used with the right synchronization, amplitude variations, and phase deviation. Since the DOCS encryption technique is completely random and any values of amplitude variations and phase deviations can be used within the phase space of the QAM symbols, the decryption process using brute force becomes more and more complicated. To begin the eavesdropping analysis against our robust system, we assume that an eavesdropper taps into the fiber link and uses the exact receiver technology as an authenticated receiver without knowledge of the codeword used, this assumption is well-known in cryptography as Kerckhoffs' Principle [183].

Fig. 5.10 (b) shows the BER as a function of the codeword symbol shift. The results indicate that employing the correct codeword for decryption, but with a single-symbol shift

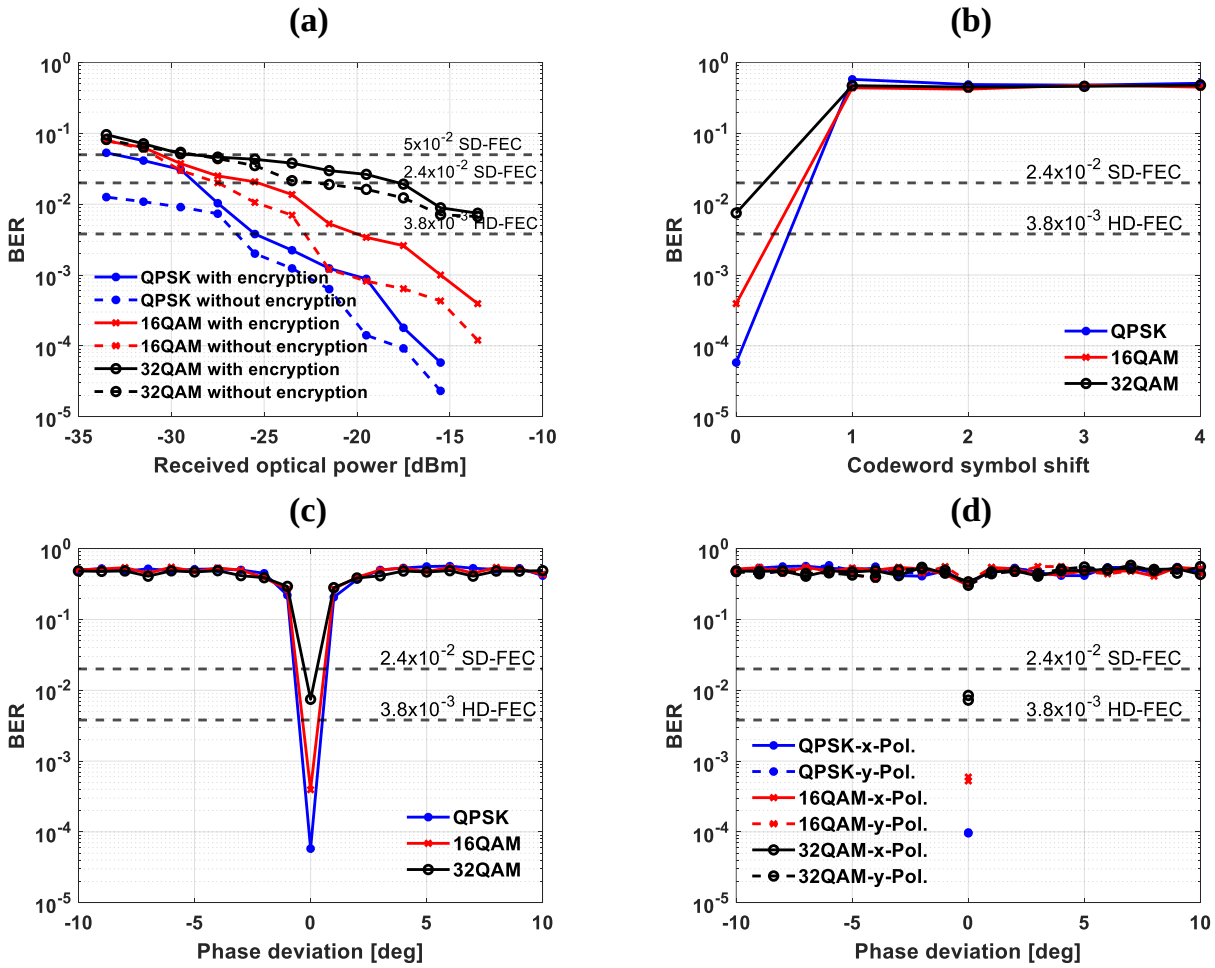

Fig. 5.10 (a) Measured BER as a function of ROP for different modulation formats with and without the DOCS encryption. (b) Measured BER as a function of the shifts in the exact codeword used for encryption and decryption for different modulation formats. (c) Measured BER as a function of the phase deviation of the exact codeword used for encryption and decryption for different modulation formats. (d) Measured BER as a function of phase deviation of two random DOCS codewords used to encrypt the two polarization states to add another layer of security.

(or more), results in an immediate increase in the BER to approximately 50%. A single-symbol shift in the exact codeword means that information symbols are displaced to new geometry in the phase space, which means every false attempt complicates the decryption process in a real-time scenario. The corresponding constellation diagrams are shown in Fig

5.11 column 2 (1 symbol shift) for QPSK, 16QAM, and 32QAM. Next, we assume the correct synchronization and amplitude variations are found but not the correct phase deviation. Fig. 5.10 (c) shows the BER as a function of the phase deviation used to decrypt the signal. A single-phase deviation shift (or more) also leads to an immediate increase in the BER to approximately 50% for the tested modulation formats. Since the received encrypted signal has an ambiguous structure, the BPS algorithm failed to compensate for the mismatching of the phase deviation even with the exact codeword and perfect synchronization. It is also important to note that signals using low-order modulation formats, such as QPSK, can tolerate more key noise than signals using high-order modulation formats, such as 32QAM, at the same symbol rate of 56 GBd. The corresponding constellation diagrams are shown in Fig. 5.11 column 3 (1 phase shift) for QPSK, 16QAM, and 32QAM.

5.3.5 Dual-polarization encryption

We further explore the performance of the system when each polarization state, X and Y, is encrypted with two random and different displacement operators. Equation 5.9 can be expressed for the two polarization states as follows:

$$\begin{bmatrix} s_{En,x}(t) \\ s_{En,y}(t) \end{bmatrix} = \begin{bmatrix} s_x(t) & 0 \\ 0 & s_y(t) \end{bmatrix} \begin{bmatrix} |\beta_x(t)|\, e^{j(\varphi_x(t)+\delta\varphi_x)} \\ |\beta_y(t)|\, e^{j(\varphi_y(t)+\delta\varphi_y)} \end{bmatrix} \tag{5.12}$$

Fig. 5.10 (d) shows the measured BER as a function of phase deviation for different encryption in the X-Y polarization. Data points below the SD-FEC threshold are with the correct phase deviation and synchronization for each polarization. If the inverse of the X-polarized displacement operator is applied to decrypt the Y-polarized signal, the measured BER is above 30%, and vice versa. The corresponding constellation diagrams are shown in

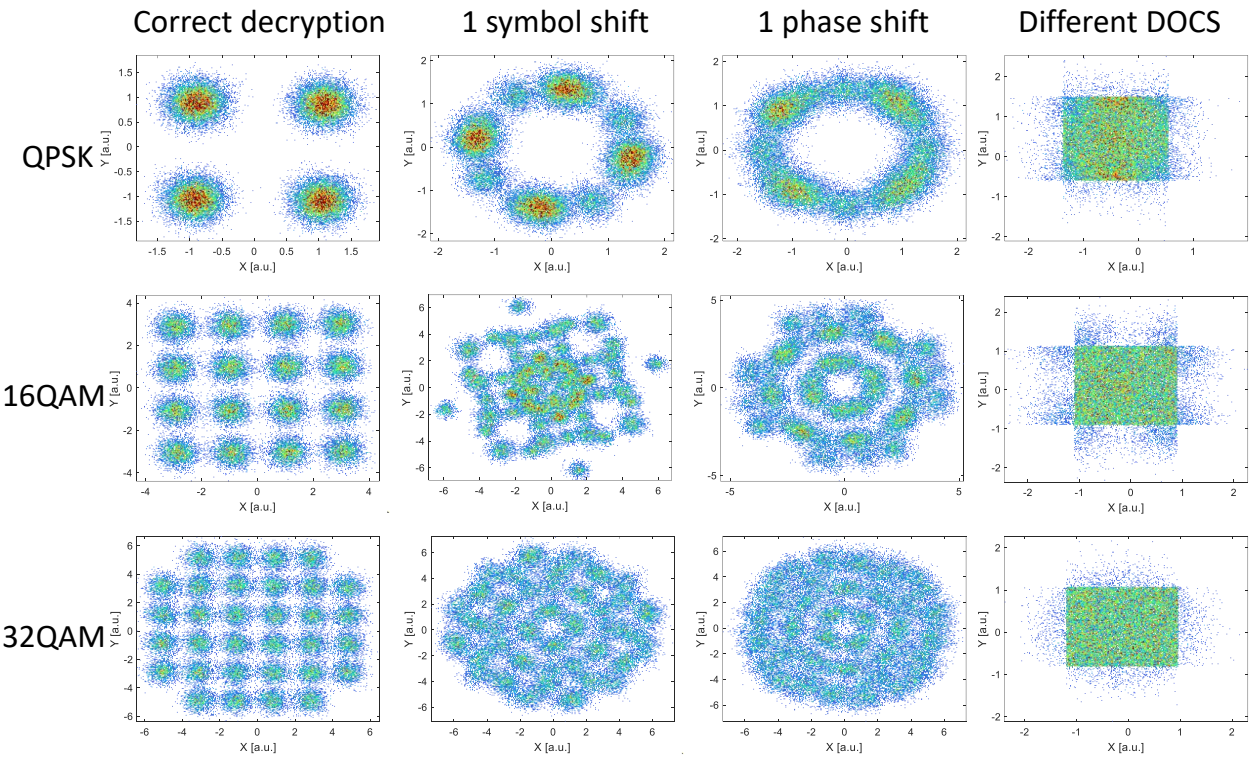

Fig. 5.11 Constellation diagrams of QPSK, 16QAM, and 32QAM when the correct DOCS decryption is used, a single-symbol shift in the correct codeword, a single-phase shift in the correct codeword, and a different DOCS decryption, respectively.

Fig. 5.12. In general, if a false displacement operator is applied to decrypt the signal, the adversary should not be able to extract any information from the signal. The constellation diagrams in this case are shown in Fig. 5.11, column 4.

5.4 Summary

In this chapter, we have demonstrated an encryption technique based on a roundtrip mechanism for coherent optical communication systems. In this mechanism, encryption relies on an external PM to incorporate the phase mask series, known as the codeword. The codeword is

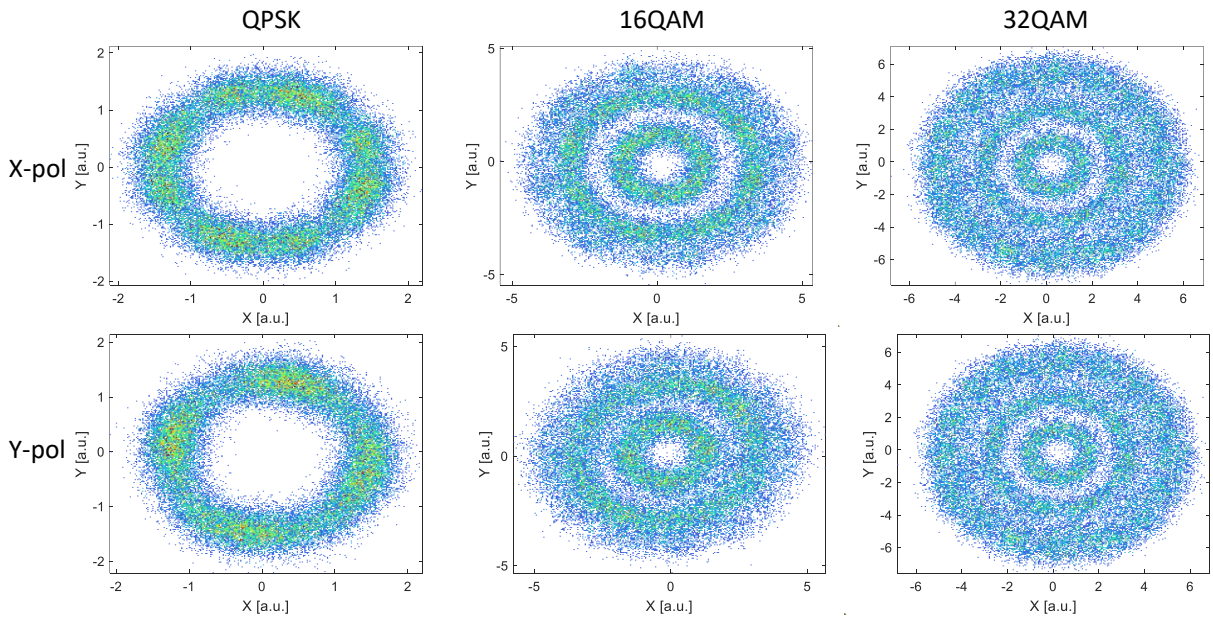

Fig. 5.12 The two polarization states are encrypted with two different displacement operators. Constellation diagrams of QPSK, 16QAM, and 32QAM when the decryption of X-polarized symbols is done using the Y-polarized displacement operator and vice versa.

entirely random, and its length is determined by the DAC memory length. The advantage of this technique is that the authenticated transmitter does not need to share any information about the codeword with other entities. Any user intending to send an information signal to the authenticated user must wait for the authenticated user to transmit the phase-encrypted signal. This phase-encrypted signal serves as an envelope for the other user's information signal. The trade-off involves stringent synchronization requirements, especially when using two independent DACs. However, this technique proves robust against eavesdropping attacks. We showcased the measured BER as a function of the error percentage in the codeword to test the robustness of such a technique. Additionally, we emphasized that the initial phase of the PM is a crucial factor affecting BER performance.

Furthermore, we mimicked the PM and employed the EPS in the DSP to enable a one-

way transmission system. Moreover, we proposed and demonstrated DSP-based encryption using the displacement operator (the general form of EPS) with coherent states in a conventional coherent optical communication system. Our investigation focused on assessing the system's performance with and without encryption, allowing us to quantify the impact of the proposed encryption technique. Experimental results indicate the feasibility of implementing the DOCS encryption technique within the existing coherent optical communication infrastructure. The security aspect of DOCS encryption becomes evident when considering potential eavesdropping attempts. If an adversary gains access to the fiber link and detects the encrypted signal, complete knowledge of the DOCS encryption is required for successful decryption. Any false trial by the adversary only introduces additional ambiguity to the received signal, enhancing the security of the communication channel.

The integration of the DOCS encryption/decryption technique with coherent DSP at the transmitter/receiver ends establishes a robust foundation for secure data transmission. The proposed encryption technique is tested over 80 km of SSMF transmissions using dual polarization at 56 GBd. The aggregate bit rates achieved are 224, 448, and 560 Gb/s for QPSK, 16QAM, and 32QAM modulation formats, respectively. Our experimental results demonstrate that attempting to decrypt the signal with any symbol shift, phase deviation shift, or a different codeword results in a BER of approximately 50%. We further increased the complexity of the system by employing two random and distinct displacement operators to independently encrypt the X-polarization and Y-polarization symbols. If the X-polarized symbols are decrypted with the displacement operator applied to the Y-polarized symbols, data cannot be decrypted, and vice versa. This highlights the resilience of DOCS encryption against eavesdropping attacks, showcasing its effectiveness in ensuring the confidentiality of the transmitted data

Chapter 6

Summary and Future Work

6.1 Summary

QD-MLLDs and silicon photonics are most likely to become key elements of future WDM transceivers, leading to efficient and high-capacity transmission systems. Coherent WDM communications can be realized by deploying a pair of QD-MLLDs; one serves as a multi-wavelength laser source at the transmitter, while the other acts as several LOs at the receiver. Several integrated filtering devices need to be used to filter or select each channel and avoid ISI. A transmission system cannot be completed without ensuring data secrecy, therefore, employing encryption techniques is important for every communication link. In the framework of this thesis, we presented SiP devices, QD-MLLDs, and encryption techniques.

Regarding silicon photonic devices, we proposed a fully reconfigurable WBG that can be utilized to filter multiple bands. One of the designed devices has a uniform heater structure on top of the waveguide that controls different sections of the silicon waveguide by changing

the heat of that section and thus changing the refractive index. Heating multiple sections at the same time led to the generation of multiple stop-bands. One of the advantages of the proposed device is that it can replace multiple WBG connected in series. We performed thorough simulations using COMOSL Multiphysics to study the thermal distribution along the waveguide, then we used the TMM algorithm to simulate the WBG transmission responses. Furthermore, we proposed another WBG with a tilted heater structure to introduce chirped WBG. The induced chirp is relatively low and cannot be detected in experiments, however, we demonstrated simulation results to predict the value of chirp for different voltages.

We also investigated the possibility of generating OFC using 3-cascaded MZMs on SOI platform. We proved that 2-cascaded MZMs can generate 9 comb flexible comb lines with a frequency spacing up to 16 GHz, limited to the RF signal generator and bandwidth of the MZM. The proposed modulators are identical, and each one has a 3 dB bandwidth of 15 GHz under a 6 V bias voltage. The design of the 3-cascaded MZMs can be further optimized to reduce the insertion loss, which in return improves the OFC generated using the EO method.

Concerning QD-MLLDs for future coherent modems, we investigated the performance of a QD-MLLD for high-capacity coherent transmission systems. The simple operation of such devices and their compact size make them promising candidates for compact and efficient WDM transceivers. We demonstrated a comprehensive characterization of the QD-MLLD. This characterization includes investigation of the RIN profile, RF and optical linewidth, frequency and phase noise for each line. The QD-MLLD can generate up to 45 usable comb lines for transmission. The comb spectrum can be programmed with a programmable filter to control the frequency spacing between the comb lines. The natural frequency spacing of our QD-MLLD is 25 GHz, and we shaped the comb lines to have a frequency spacing of 50 GHz and 100 GHz. Therefore, we utilized this approach to demonstrate super-channel

transmission with a minimum guard band between the comb lines. Although our experiment utilizes a single polarization, it can be easily upgraded to dual polarization to double the data rates. The performance of each line was investigated, and our experimental results indicated that almost all channels exhibited similar performance. Thus, the QD-MLLD was proven to be a stable and suitable source for coherent WDM transmission systems. We achieved net data rates up to 447.8 Gb/s per line using 64QAM at a high symbol rate of 80 GBd over 80 km of SSMF. Furthermore, we provided a comprehensive comparison between the comb source and a commercial narrow-linewidth ITLA. Our results conclude that the QD-MLLD is a competitive laser source and its performance is similar to the narrow linewidth ITLA. Furthermore, we investigated the possibility of using the QD-MLLD as LOs for coherent transmission over 80 km of SSMF. We proved that the QD-MLLD can be used either as signal carriers or LOs or both. We also investigated the performance of QD-MLLD with a single segment SiP modulator on-chip and achieved symbol rates up to 80 GBd at 32 QAM. The BER values are below the SD-FEC threshold.

In order to ensure data confidentiality, we proposed several encryption techniques. The first one is based on a roundtrip mechanism in which an authenticated user at the transmitter sends a phase-encrypted signal to another user. That phase-encrypted signal acts as an envelope for the other user to incorporate their information signal and send it back to the first user through another fiber channel. We took into consideration eavesdropping attacks, or the so-called tapping attacks, wherein adversaries tap into the fiber link to steal sensitive information. Our experimental results indicated that without knowledge of the secret key or the codeword, adversaries cannot extract any information from the signal. The encryption technique was based on a completely random phase mask that was only known by the authenticated user. Since complete randomization can be implemented, the

authenticated user can change the codeword more frequently for every transmission to ensure data confidentiality. Furthermore, we proposed another encryption technique for one-way transmission systems that is DSP-based. We introduced displacement operators that can displace the QAM symbols randomly. In other words, the codeword randomly changes the amplitudes and phases of the QAM symbols. Without that codeword, symbols cannot be demodulated at the receiver side. Synchronization is also an important factor to be considered because any mismatch would fail to decrypt the signal. Finally, we proposed a novel dual-polarization encryption in which the X and Y polarization symbols are encrypted with two different and random codewords. Our experimental results are recorded for different modulation formats, 4/16/32QAM at a high symbol rate of 56 GBd.

6.2 Future research avenues

The development of silicon photonics and optical communications is growing rapidly, and research never stops. Although the objectives of this research have been achieved, probing deeper, there are still other research opportunities to be investigated. Below, we propose directions for future research that could be derived from the work we presented in this thesis:

- Improved design of the chirped WBG based on tilted heater structure can be further investigated. The tilted heater element can be designed closer to the waveguide to observe higher changes in the refractive index of the waveguide. Thus, leading to a larger group delay that could be realized in experiments.

- On-chip OFCs generators using cascaded MZMs can be further improved by eliminating the Y-branches between each modulator to reduce the insertion loss. Improvement on

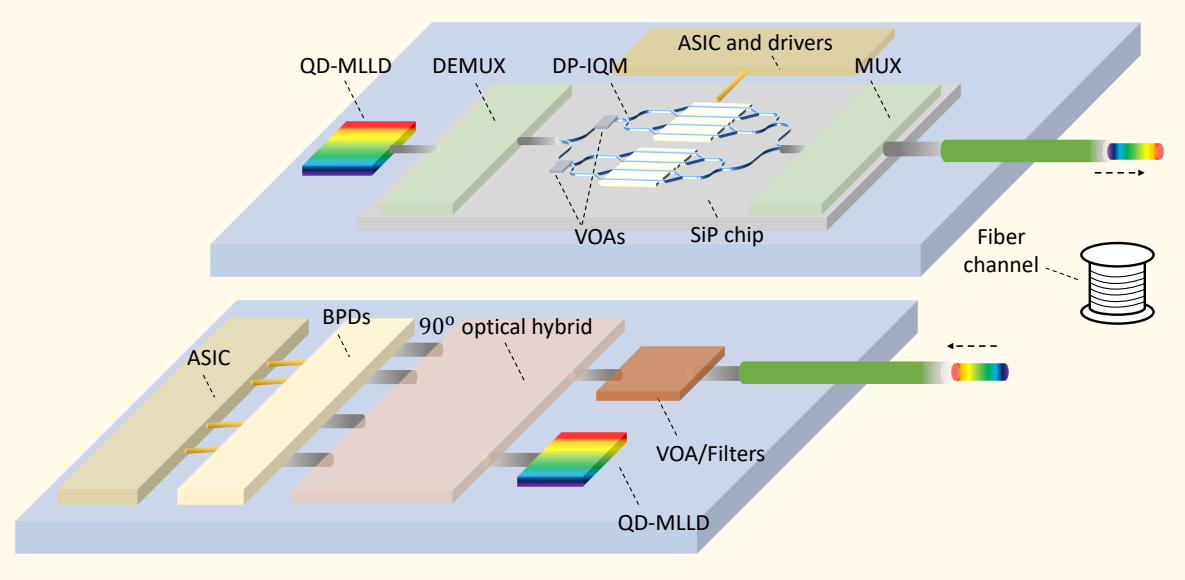

Fig. 6.1 Schematic of future fully integrated coherent transmission WDM system with QD-MLLD as source and LO.

the modulator design to extend the 3 dB bandwidth could also be a new project to generate OFCs with larger frequency spacing.

- QD-MLLDs are still under investigation and development. The design of such devices can be further investigated, for example, to observe the effect of adding more quantum dashes/dots. Integration with silicon photonics could be a new project to develop a hybrid integrated coherent transmitter, and the same goes for the receiver. We propose a schematic view of future fully integrated coherent transmission in Fig. 6.1. We are certain that in the next few years, that will be commercially available.

- Other physical layer encryption techniques can be investigated such as by employing two PMs, one at the transmitter and another at the receiver. An IQ modulator could also be realized instead of the PM.

References

[1] "Follow the latest trend news in the semiconductor industry, Yole Group." https://www.yolegroup.com/product/report/silicon-photonics-2023/. Accessed: 2024-02-09.

[2] E. Berikaa, M. S. Alam, A. Samani, S. Lessard, and D. V. Plant, "Net 1 Tbps/λ transmission over 80 km of SSMF using a single segment sip IQM with all-electronic equalization," in *2022 Optical Fiber Communications Conference and Exhibition (OFC)*, pp. 1–3, 2022.

[3] R. Zhang, K. Kuzmin, Y.-W. Chen, and W. I. Way, "800G/λ self-homodyne coherent links with simplified DSP for next-generation intra-data centers," *Journal of Lightwave Technology*, vol. 41, no. 4, pp. 1216–1222, 2023.

[4] J. Zhang, J. Yu, B. Zhu, F. Li, H.-C. Chien, Z. Jia, Y. Cai, X. Li, X. Xiao, Y. Fang, and Y. Wang, "Transmission of single-carrier 400G signals (515.2-gb/s) based on 128.8-GBaud PDM QPSK over 10,130- and 6,078 km terrestrial fiber links," *Optics Express*, vol. 23, pp. 16540–16545, Jun 2015.

[5] F. Buchali, A. Klekamp, L. Schmalen, and T. Drenski, "Implementation of 64qam at 42.66 GBaud using 1.5 samples per symbol DAC and demonstration of up to 300 km

fiber transmission," in *OFC 2014*, pp. 1–3, 2014.

[6] R. Rios-Müller, J. Renaudier, P. Brindel, A. Ghazisaeidi, I. Fernandez, P. Tran, C. Simonneau, L. Schmalen, and G. Charlet, "Spectrally-efficient 400-Gb/s single carrier transport over 7 200 km," *Journal of Lightwave Technology*, vol. 33, no. 7, pp. 1402–1407, 2015.

[7] J. C. Geyer, C. Doerr, M. Aydinlik, N. Nadarajah, A. Caballero, C. Rasmussen, and B. Mikkelsen, "Practical implementation of higher order modulation beyond 16-QAM," in *2015 Optical Fiber Communications Conference and Exhibition (OFC)*, pp. 1–3, 2015.

[8] L. Kull, "Challenges in implementing high-speed, low-power ADCs in CMOS," in *2015 Optical Fiber Communications Conference and Exhibition (OFC)*, pp. 1–3, 2015.

[9] G. Bennett, K.-t. Wu, A. Malik, S. Roy, and A. Awadalla, "A review of high-speed coherent transmission technologies for long-haul DWDM transmission at 100G and beyond," *IEEE Communications Magazine*, vol. 52, no. 10, pp. 102–110, 2014.

[10] J. Zhang, J. Yu, B. Zhu, Z. Jia, F. Li, X. Li, H. C. Chien, S. Shi, C. Ge, Y. Xia, and Y. Chen, "WDM transmission of twelve 960 Gb/s channels based on 120-GBaud ETDM PDM-16QAM over 1200-km Terawave fiber link," in *2016 Optical Fiber Communications Conference and Exhibition (OFC)*, pp. 1–3, 2016.

[11] G. Raybon, A. L. Adamiecki, P. Winzer, C. Xie, A. Konczykowska, F. Jorge, J.-Y. Dupuy, L. L. Buhl, S. Chandrashekhar, S. Draving, M. Grove, and K. Rush, "Single-carrier 400G interface and 10-channel WDM transmission over 4,800 km using all-ETDM 107-Gbaud PDM-QPSK," in *2013 Optical Fiber Communication Conference*

and Exposition and the National Fiber Optic Engineers Conference (OFC/NFOEC), pp. 1–4, 2013.

[12] V. Torres-Company, J. Schroder, A. Fulop, M. Mazur, L. Lundberg, O. B. Helgason, M. Karlsson, and P. A. Andrekson, "Laser frequency combs for coherent optical communications," *Journal of Lightwave Technology*, vol. 37, no. 7, pp. 1663–1670, 2019.

[13] P. Marin-Palomo, J. N. Kemal, T. J. Kippenberg, W. Freude, S. Randel, and C. Koos, "Performance of chip-scale optical frequency comb generators in coherent WDM communications," *Optics Express*, vol. 28, no. 9, pp. 12897–12910, 2020.

[14] P. Delfyett, S. Gee, M.-T. Choi, H. Izadpanah, W. Lee, S. Ozharar, F. Quinlan, and T. Yilmaz, "Optical frequency combs from semiconductor lasers and applications in ultrawideband signal processing and communications," *Journal of Lightwave Technology*, vol. 24, no. 7, pp. 2701–2719, 2006.

[15] A. Y. Liu, S. Srinivasan, J. Norman, A. C. Gossard, and J. E. Bowers, "Quantum dot lasers for silicon photonics," *Photon. Res.*, vol. 3, pp. B1–B9, Oct 2015.

[16] G. Liu, P. J. Poole, Z. Lu, J. Liu, Y. Mao, P. Barrios, and M. Vachon, "Comparison of noise characteristics of InAs/InP quantum dash and quantum well mode-locked lasers," in *OSA Advanced Photonics Congress 2021*, p. NoW2A.4, Optica Publishing Group, 2021.

[17] J. C. Norman, D. Jung, Z. Zhang, Y. Wan, S. Liu, C. Shang, R. W. Herrick, W. W. Chow, A. C. Gossard, and J. E. Bowers, "A review of high-performance quantum dot lasers on silicon," *IEEE Journal of Quantum Electronics*, vol. 55, no. 2, pp. 1–11, 2019.

[18] A. A. Ukhanov, A. Stintz, P. G. Eliseev, and K. J. Malloy, "Comparison of the carrier induced refractive index, gain, and linewidth enhancement factor in quantum dot and quantum well lasers," *Applied Physics Letters*, vol. 84, pp. 1058–1060, 02 2004.

[19] C. Shang, Y. Wan, J. Selvidge, E. Hughes, R. Herrick, K. Mukherjee, J. Duan, F. Grillot, W. W. Chow, and J. E. Bowers, "Perspectives on advances in quantum dot lasers and integration with si photonic integrated circuits," *ACS Photonics*, vol. 8, pp. 2555–2566, Sep 2021.

[20] Y. Wan, J. Norman, S. Liu, A. Liu, and J. E. Bowers, "Quantum dot lasers and amplifiers on silicon: Recent advances and future developments," *IEEE Nanotechnology Magazine*, vol. 15, no. 2, pp. 8–22, 2021.

[21] G. Liu, P. J. Poole, Z. Lu, J. Liu, C.-Y. Song, Y. Mao, and P. Barrios, "Mode-locking and noise characteristics of InAs/InP quantum dash/dot lasers," *Journal of Lightwave Technology*, vol. 41, no. 13, pp. 4262–4270, 2023.

[22] X. Guo, A. He, and Y. Su, "Recent advances of heterogeneously integrated III–V laser on Si," *Journal of Semiconductors*, vol. 40, p. 101304, oct 2019.

[23] G. Kurczveil, C. Zhang, A. Descos, D. Liang, M. Fiorentino, and R. Beausoleil, "On-chip hybrid silicon quantum dot comb laser with 14 error-free channels," in *2018 IEEE International Semiconductor Laser Conference (ISLC)*, pp. 1–2, 2018.

[24] S. Liu, D. Jung, J. C. Norman, M. J. Kennedy, A. C. Gossard, and J. E. Bowers, "490 fs pulse generation from passively mode-locked single section quantum dot laser directly grown on on-axis GaP/Si," *Electronics Letters*, vol. 54, no. 7, pp. 432–433, 2018.

[25] Z. Lu, J. Liu, P. J. Poole, Y. Mao, J. Weber, G. Liu, and P. Barrios, "InAs/InP quantum dash semiconductor coherent comb lasers and their applications in optical networks," *J. Lightwave Technol.*, vol. 39, pp. 3751–3760, Jun 2021.

[26] V. Vujicic, C. Calò, R. Watts, F. Lelarge, C. Browning, K. Merghem, A. Martinez, A. Ramdane, and L. P. Barry, "Quantum dash mode-locked lasers for data centre applications," *IEEE Journal of Selected Topics in Quantum Electronics*, vol. 21, no. 6, pp. 53–60, 2015.

[27] G.-H. Duan, A. Shen, A. Akrout, F. V. Dijk, F. Lelarge, F. Pommereau, O. LeGouezigou, J.-G. Provost, H. Gariah, F. Blache, F. Mallecot, K. Merghem, A. Martinez, and A. Ramdane, "High performance InP-based quantum dash semiconductor mode-locked lasers for optical communications," *Bell Labs Technical Journal*, vol. 14, no. 3, pp. 63–84, 2009.

[28] J. Wang, W.-J. Jiang, Y.-W. Chen, M. Al-Qadi, K. Li, K. Kuzmin, J. Ackert, D. Dougherty, W. Liu, C. Chen, H. Yamada, C. Ho, P. Wang, Y. Y. Zhao, Y. Zhou, X. Liu, K. Schmidt, J. Nee, K. McGreer, M. Boudreau, J. Sun, W. I. Way, and H. Xu, "Silicon photonics IQ modulator targeted for 800ZR data center interconnection," in *2022 European Conference on Optical Communication (ECOC)*, pp. 1–4, 2022.

[29] S. Zhalehpour, J. Lin, M. Guo, H. Sepehrian, Z. Zhang, L. A. Rusch, and W. Shi, "All-silicon IQ modulator for 100 GBaud 32QAM transmissions," in *2019 Optical Fiber Communications Conference and Exhibition (OFC)*, pp. 1–3, 2019.

[30] Z. Zheng, A. Mohammadi, O. Jafari, H. Sepehrian, J. Lin, X. Zhang, L. A. Rusch, and W. Shi, "Silicon IQ modulator for 120 Gbaud QAM," in *2021 European Conference on Optical Communication (ECOC)*, pp. 1–4, 2021.

[31] X. Wang, W. Shi, H. Yun, S. Grist, N. A. F. Jaeger, and L. Chrostowski, "Narrow-band waveguide Bragg gratings on SOI wafers with CMOS-compatible fabrication process," *Opt. Express*, vol. 20, pp. 15547–15558, Jul 2012.

[32] D. Mu, H. Qiu, J. Jiang, X. Wang, Z. Fu, Y. Wang, X. Jiang, H. Yu, and J. Yang, "A four-channel DWDM tunable add/drop demultiplexer based on silicon waveguide Bragg gratings," *IEEE Photonics Journal*, vol. 11, no. 1, pp. 1–8, 2019.

[33] H.-C. Liu and A. Yariv, "Designing coupled-resonator optical waveguides based on high-Q tapered grating-defect resonators," *Opt. Express*, vol. 20, pp. 9249–9263, Apr 2012.

[34] T. Segawa, S. Matsuo, T. Ishii, Y. Ohiso, Y. Shibata, and H. Suzuki, "High-speed wavelength-tunable optical filter using cascaded Mach–Zehnder interferometers with apodized sampled gratings," *IEEE Journal of Quantum Electronics*, vol. 44, no. 10, pp. 922–930, 2008.

[35] M. Furdek and N. Skorin-Kapov, "Physical-layer attacks in all-optical WDM networks," in *2011 Proceedings of the 34th International Convention MIPRO*, pp. 446–451, 2011.

[36] Y. Wu, H. Luo, L. Deng, Q. Yang, X. Dai, D. liu, and M. Cheng, "60 gb/s coherent optical secure communication over 100 km with hybrid chaotic encryption using one dual-polarization IQ modulator," *Opt. Lett.*, vol. 47, pp. 5285–5288, Oct 2022.

[37] B. Wu, Z. Wang, Y. Tian, M. P. Fok, B. J. Shastri, D. R. Kanoff, and P. R. Prucnal, "Optical steganography based on amplified spontaneous emission noise," *Opt. Express*, vol. 21, pp. 2065–2071, Jan 2013.

[38] K. Chan, C.-K. Chan, L. K. Chen, and F. Tong, "Demonstration of 20-Gb/s all-optical XOR gate by four-wave mixing in semiconductor optical amplifier with RZ-DPSK modulated inputs," *IEEE Photonics Technology Letters*, vol. 16, no. 3, pp. 897–899, 2004.

[39] P. Eraerds, N. Walenta, M. Legré, N. Gisin, and H. Zbinden, "Quantum key distribution and 1 Gbps data encryption over a single fibre," *New Journal of Physics*, vol. 12, p. 063027, jun 2010.

[40] T. Murphy, J. Hastings, and H. Smith, "Fabrication and characterization of narrowband Bragg-reflection filters in silicon-on-insulator ridge waveguides," *Journal of Lightwave Technology*, vol. 19, no. 12, pp. 1938–1942, 2001.

[41] M. Hammood, A. Mistry, M. Ma, H. Yun, L. Chrostowski, and N. A. F. Jaeger, "Compact, silicon-on-insulator, series-cascaded, contradirectional-coupling-based filters with >50 dB adjacent channel isolation," *Opt. Lett.*, vol. 44, pp. 439–442, Jan 2019.

[42] J. St-Yves, H. Bahrami, P. Jean, S. LaRochelle, and W. Shi, "Widely bandwidth-tunable silicon filter with an unlimited free-spectral range," *Opt. Lett.*, vol. 40, pp. 5471–5474, Dec 2015.

[43] Z. Zhang, J. C. Norman, S. Liu, A. Malik, and J. E. Bowers, "Integrated dispersion compensated mode-locked quantum dot laser," *Photon. Res.*, vol. 8, pp. 1428–1434, Sep 2020.

[44] Y. Sun, D. Wang, C. Deng, M. Lu, L. Huang, G. Hu, B. Yun, R. Zhang, M. Li, J. Dong, A. Wang, and Y. Cui, "Large group delay in silicon-on-insulator chirped spiral Bragg grating waveguide," *IEEE Photonics Journal*, vol. 13, no. 5, pp. 1–5, 2021.

[45] O. Jafari, W. Shi, and S. Larochelle, "Mach-Zehnder silicon photonic modulator assisted by phase-shifted Bragg gratings," *IEEE Photonics Technology Letters*, vol. 32, no. 8, pp. 445–448, 2020.

[46] W. Zhang and J. Yao, "A fully reconfigurable waveguide Bragg grating for programmable photonic signal processing," *Nature Communications*, vol. 9, p. 1396, Apr 2018.

[47] W. Zhang and J. Yao, "Silicon-based on-chip electrically-tunable spectral shaper for continuously tunable linearly chirped microwave waveform generation," *Journal of Lightwave Technology*, vol. 34, no. 20, pp. 4664–4672, 2016.

[48] P. Marin-Palomo, J. N. Kemal, M. Karpov, A. Kordts, J. Pfeifle, M. H. P. Pfeiffer, P. Trocha, S. Wolf, V. Brasch, M. H. Anderson, R. Rosenberger, K. Vijayan, W. Freude, T. J. Kippenberg, and C. Koos, "Microresonator-based solitons for massively parallel coherent optical communications," *Nature*, vol. 546, no. 7657, pp. 274–279, 2017.

[49] S. Fujii, S. Tanaka, T. Ohtsuka, S. Kogure, K. Wada, H. Kumazaki, S. Tasaka, Y. Hashimoto, Y. Kobayashi, T. Araki, K. Furusawa, N. Sekine, S. Kawanishi, and T. Tanabe, "Dissipative kerr soliton microcombs for FEC-free optical communications over 100 channels," *Optics Express*, vol. 30, no. 2, pp. 1351–1364, 2022.

[50] J. Pfeifle, V. Brasch, M. Lauermann, Y. Yu, D. Wegner, T. Herr, K. Hartinger, P. Schindler, J. Li, D. Hillerkuss, R. Schmogrow, C. Weimann, R. Holzwarth, W. Freude, J. Leuthold, T. J. Kippenberg, and C. Koos, "Coherent terabit communications with microresonator kerr frequency combs," *Nature Photonics*, vol. 8, no. 5, pp. 375–380, 2014.

[51] B. Corcoran, M. Tan, X. Xu, A. Boes, J. Wu, T. G. Nguyen, S. T. Chu, B. E. Little, R. Morandotti, A. Mitchell, and D. J. Moss, "Ultra-dense optical data transmission over standard fibre with a single chip source," *Nature Communications*, vol. 11, no. 1, p. 2568, 2020.

[52] J. Pfeifle, V. Vujicic, R. T. Watts, P. C. Schindler, C. Weimann, R. Zhou, W. Freude, L. P. Barry, and C. Koos, "Flexible terabit/s Nyquist-WDM super-channels using a gain-switched comb source," *Optics Express*, vol. 23, no. 2, pp. 724–738, 2015.

[53] P. M. Anandarajah, R. Maher, Y. Q. Xu, S. Latkowski, J. O'Carroll, S. G. Murdoch, R. Phelan, J. O'Gorman, and L. P. Barry, "Generation of coherent multicarrier signals by gain switching of discrete mode lasers," *IEEE Photonics Journal*, vol. 3, no. 1, pp. 112–122, 2011.

[54] Y. Cui, Z. Wang, Y. Xu, Y. Jiang, J. Yu, and Z. Huang, "Generation of flat optical frequency comb using cascaded PMs with combined harmonics," *IEEE Photonics Technology Letters*, vol. 34, no. 9, pp. 490–493, 2022.

[55] H. Sun, M. Khalil, Z. Wang, and L. R. Chen, "Recent progress in integrated electro-optic frequency comb generation," *Journal of Semiconductors*, vol. 42, no. 4, p. 041301, 2021.

[56] G. Liu, P. J. Poole, Z. Lu, J. Liu, Y. Mao, M. Vachon, and P. Barrios, "InAs/InP quantum dot mode-locked laser with an aggregate 12.544 Tbit/s transmission capacity," *Optics Express*, vol. 30, no. 3, pp. 3205–3214, 2022.

[57] Z. Lu, J. Liu, Y. Mao, K. Zeb, G. Liu, P. J. Poole, J. Weber, M. Rahim, G. Pakulski, C. Song, M. Vachon, P. Barrios, D. Poitras, S. Wang, and W. Jiang, "Quantum

dash multi-wavelength lasers for Tbit/s coherent communications and 5G wireless networks," *Journal of the European Optical Society-Rapid Publications*, vol. 17, no. 1, p. 9, 2021.

[58] A. Akrout, F. van Dijk, G.-H. Duan, A. Shen, F. Lelarge, and A. Ramdane, "Low phase noise optical oscillator at 30Ghz using a quantum dash mode-locked laser associated with an optical self injection loop," in *2009 International Topical Meeting on Microwave Photonics*, pp. 1–3, 2009.

[59] K. Merghem, A. Akrout, A. Martinez, G. Aubin, A. Ramdane, F. Lelarge, and G.-H. Duan, "Pulse generation at 346 GHz using a passively mode locked quantum-dash-based laser at 1.55 μm," *Applied Physics Letters*, vol. 94, p. 021107, 01 2009.

[60] J. N. Kemal, P. Marin-Palomo, K. Merghem, G. Aubin, F. Lelarge, A. Ramdane, S. Randel, W. Freude, and C. Koos, "32QAM WDM transmission at 12 Tbit/s using a quantum-dash mode-locked laser diode (QD-MLLD) with external-cavity feedback," *Optics Express*, vol. 28, pp. 23594–23608, Aug 2020.

[61] Z. Lu, J. Liu, L. Mao, C.-Y. Song, J. Weber, and P. Poole, "12.032 Tbit/s coherent transmission using an ultra-narrow linewidth qantum dot 34.46-GHz C-band coherent comb laser," in *Next-Generation Optical Communication: Components, Sub-Systems, and Systems VIII* (G. Li and X. Zhou, eds.), vol. 10947, p. 109470J, International Society for Optics and Photonics, SPIE, 2019.

[62] P. Marin-Palomo, J. N. Kemal, P. Trocha, S. Wolf, K. Merghem, F. Lelarge, A. Ramdane, W. Freude, S. Randel, and C. Koos, "Comb-based WDM transmission at 10 Tbit/s using a DC-driven quantum-dash mode-locked laser diode," *Optics Express*, vol. 27, no. 22, pp. 31110–31129, 2019.

[63] D. K. Shin, B. M. Henson, R. I. Khakimov, J. A. Ross, C. J. Dedman, S. S. Hodgman, K. G. H. Baldwin, and A. G. Truscott, "Widely tunable, narrow linewidth external-cavity gain chip laser for spectroscopy between 1.0 – 1.1 μm," *Opt. Express*, vol. 24, pp. 27403–27414, Nov 2016.

[64] H. Asghar, E. Sooudi, P. Kumar, W. Wei, and J. G. McInerney, "Optimum stabilization of self-mode-locked quantum dash lasers using dual optical feedback with improved tolerance against phase delay mismatch," *Opt. Express*, vol. 25, pp. 15796–15805, Jul 2017.

[65] L. N. Venkatasubramani, H. Xu, M. Buyalo, A. Gubenko, Y. Yu, and L. Barry, "100 Gbps/λ transmission with quantum dot O-band comb source using 50 GBd PAM4/16QAM-OFDM signals," in *2023 Optical Fiber Communications Conference and Exhibition (OFC)*, pp. 1–3, 2023.

[66] M. T. A. Khan, E. Alkhazraji, A. M. Ragheb, H. Fathallah, K. K. Qureshi, S. Alshebeili, and M. Z. M. Khan, "100 Gb/s single channel transmission using injection-locked 1621 nm quantum-dash laser," *IEEE Photonics Technology Letters*, vol. 29, no. 6, pp. 543–546, 2017.

[67] M. Khan, E. Alkhazraji, M. A. Shemis, A. Ragheb, H. Fathallah, S. Alshebeili, and M. Khan, "Up to 128 Gb/s DP-QPSK transmission using injection-locked quantum-dash laser for NG-PONs," in *2017 Asia Communications and Photonics Conference (ACP)*, pp. 1–3, 2017.

[68] M. A. Shemis, E. Alkhazraji, A. M. Ragheb, M. T. A. Khan, M. Esmail, H. Fathallah, S. A. Alshebeili, and M. Z. M. Khan, "Broadly tunable self-injection locked InAs/InP

quantum-dash laser based fiber/FSO/hybrid fiber-FSO communication at 1610 nm," *IEEE Photonics Journal*, vol. 10, no. 2, pp. 1–10, 2018.

[69] L. Chrostowski and M. Hochberg, *Silicon Photonics Design From Devices to Systems*. Cambridge University Press, 2015.

[70] L. A. Coldren, S. W. Corzine, and M. L. Mašanović, *Mirrors and Resonators for Diode Lasers*, ch. Three, pp. 91–155. John Wiley & Sons, Ltd, 2012.

[71] G. P. Agrawal, *Signal Propagation in Fibers*, ch. 3, pp. 63–106. John Wiley & Sons, Ltd, 2005.

[72] M. S. Alam, X. Li, M. Jacques, Z. Xing, A. Samani, E. El-Fiky, P.-C. Koh, and D. V. Plant, "Net 220 Gbps/λ IM/DD transmssion in O-band and C-band with silicon photonic traveling-wave MZM," *Journal of Lightwave Technology*, vol. 39, no. 13, pp. 4270–4278, 2021.

[73] R. Ramaswami and K. N. Sivarajan, *Optical networks: a practical perspective*. San Francisco, CA, USA: Morgan Kaufmann Publishers Inc., 1998.

[74] G. P. Agrawal, *Fiber-Optic Communication Systems*. John Wiley & Sons, 3rd ed., 2002.

[75] G. Agrawal, *Nonlinear Fiber Optics (Fifth Edition)*. Optics and Photonics, Boston: Academic Press, fifth edition ed., 2013.

[76] M. Kuschnerov, F. N. Hauske, K. Piyawanno, B. Spinnler, M. S. Alfiad, A. Napoli, and B. Lankl, "DSP for coherent single-carrier receivers," *Journal of Lightwave Technology*, vol. 27, no. 16, pp. 3614–3622, 2009.

[77] X. S. Yao and L. Yan, "Polarization management for polarization-division-multiplexing and coherent detection systems," in *2008 Digest of the IEEE/LEOS Summer Topical Meetings*, pp. 147–148, 2008.

[78] S. J. Savory, "Digital coherent optical receivers: Algorithms and subsystems," *IEEE Journal of Selected Topics in Quantum Electronics*, vol. 16, no. 5, pp. 1164–1179, 2010.

[79] S. Haykin, *Communication Systems*. Wiley Publishing, 5th ed., 2009.

[80] I. Fatadin, S. J. Savory, and D. Ives, "Compensation of quadrature imbalance in an optical QPSK coherent receiver," *IEEE Photonics Technology Letters*, vol. 20, no. 20, pp. 1733–1735, 2008.

[81] S. J. Savory, "Digital filters for coherent optical receivers," *Opt. Express*, vol. 16, pp. 804–817, Jan 2008.

[82] M. S. Faruk and S. J. Savory, "Digital signal processing for coherent transceivers employing multilevel formats," *Journal of Lightwave Technology*, vol. 35, no. 5, pp. 1125–1141, 2017.

[83] S. Hoffmann, S. Bhandare, T. Pfau, O. Adamczyk, C. Wordehoff, R. Peveling, M. Porrmann, and R. Noe, "Frequency and phase estimation for coherent QPSK transmission with unlocked DFB lasers," *IEEE Photonics Technology Letters*, vol. 20, no. 18, pp. 1569–1571, 2008.

[84] M. S. Faruk and K. Kikuchi, "Compensation for in-phase/quadrature imbalance in coherent-receiver front end for optical quadrature amplitude modulation," *IEEE Photonics Journal*, vol. 5, no. 2, pp. 7800110–7800110, 2013.

[85] M. Torbatian, D. Lavery, M. Osman, D. Yao, D. S. Millar, Y. Gao, A. Kakkar, Z. A. El-Sahn, C. Doggart, A. E. Morra, N. Abughalieh, S. Yang, X. Chen, R. Maher, H. Sun, K.-T. Wu, and P. Kandappan, "Performance oriented DSP for flexible long haul coherent transmission," *Journal of Lightwave Technology*, vol. 40, no. 5, pp. 1256–1272, 2022.

[86] I. Fatadin, D. Ives, and S. J. Savory, "Blind equalization and carrier phase recovery in a 16-QAM optical coherent system," *Journal of Lightwave Technology*, vol. 27, no. 15, pp. 3042–3049, 2009.

[87] X. Zhou, K. Zhong, Y. Gao, C. Lu, A. P. T. Lau, and K. Long, "Modulation-format-independent blind phase search algorithm for coherent optical square M-QAM systems," *Opt. Express*, vol. 22, pp. 24044–24054, Oct 2014.

[88] J. G. Proakis, *Digital Communications 5th Edition*. McGraw Hill, 2007.

[89] M. Gioannini, "Numerical modeling of the emission characteristics of semiconductor quantum dash materials for lasers and optical amplifiers," *IEEE Journal of Quantum Electronics*, vol. 40, no. 4, pp. 364–373, 2004.

[90] R. Rosales, S. G. Murdoch, R. Watts, K. Merghem, A. Martinez, F. Lelarge, A. Accard, L. P. Barry, and A. Ramdane, "High performance mode locking characteristics of single section quantum dash lasers," *Opt. Express*, vol. 20, pp. 8649–8657, Apr 2012.

[91] G. Roelkens, A. Abassi, P. Cardile, U. Dave, A. De Groote, Y. De Koninck, S. Dhoore, X. Fu, A. Gassenq, N. Hattasan, Q. Huang, S. Kumari, S. Keyvaninia, B. Kuyken, L. Li, P. Mechet, M. Muneeb, D. Sanchez, H. Shao, T. Spuesens, A. Z. Subramanian, S. Uvin, M. Tassaert, K. Van Gasse, J. Verbist, R. Wang, Z. Wang,

J. Zhang, J. Van Campenhout, X. Yin, J. Bauwelinck, G. Morthier, R. Baets, and D. Van Thourhout, "III-V-on-silicon photonic devices for optical communication and sensing," *Photonics*, vol. 2, no. 3, pp. 969–1004, 2015.

[92] M. Khalil, H. Sun, and L. R. Chen, "Electrically reconfigurable waveguide Bragg gratings for multiple tunable wavelength-division multiplexing filters," in *Optica Advanced Photonics Congress 2022*, p. ITh2B.6, Optica Publishing Group, 2022.

[93] M. Khalil, H. Sun, E. Berikaa, D. V. Plant, and L. R. Chen, "Electrically reconfigurable waveguide bragg grating filters," *Opt. Express*, vol. 30, pp. 39643–39651, Oct 2022.

[94] M. Hochberg and T. Baehr-Jones, "Towards fabless silicon photonics," *Nature Photonics*, vol. 4, pp. 492–494, Aug 2010.

[95] S. Kaushal, R. Cheng, M. Ma, A. Mistry, M. Burla, L. Chrostowski, and J. Azaña, "Optical signal processing based on silicon photonics waveguide Bragg gratings: review," *Frontiers of Optoelectronics*, vol. 11, pp. 163–188, Jun 2018.

[96] G. Jiang, R. Chen, Q. Zhou, J. Yang, M. Wang, and X. Jiang, "Slab-modulated sidewall Bragg gratings in silicon-on-insulator ridge waveguides," *IEEE Photonics Technology Letters*, vol. 23, no. 1, pp. 6–8, 2011.

[97] W. Zhang, N. Ehteshami, W. Liu, and J. Yao, "Silicon-based on-chip electrically tunable sidewall Bragg grating Fabry Perot filter," *Optics Letters*, vol. 40, pp. 3153–3156, Jul 2015.

[98] C. Klitis, M. Sorel, and M. J. Strain, "Active on-chip dispersion control using a tunable silicon Bragg grating," *Micromachines*, vol. 10, no. 9, 2019.

[99] M. Spasojevic and L. Chen, "Discretely tunable optical delay lines using serial and step-chirped sidewall Bragg gratings in SOI," *Electronics Letters*, vol. 49, no. 9, pp. 608–610, 2013.

[100] M. Burla, L. R. Cortés, M. Li, X. Wang, L. Chrostowski, and J. Azaña, "Integrated waveguide Bragg gratings for microwave photonics signal processing," *Optics Express*, vol. 21, pp. 25120–25147, 2013.

[101] W. Shi, V. Veerasubramanian, D. Patel, and D. V. Plant, "Tunable nanophotonic delay lines using linearly chirped contradirectional couplers with uniform Bragg gratings," *Opt. Lett.*, vol. 39, pp. 701–703, Feb 2014.

[102] J. A. Davis, A. Li, N. Alshamrani, and Y. Fainman, "Silicon photonic chip for 16-channel wavelength division de-multiplexing in the O-band," *Opt. Express*, vol. 28, pp. 23620–23627, Aug 2020.

[103] G. Eranna, *Crystal Growth and Evaluation of Silicon for VLSI and ULSI*. CRC Press 1st ed., 2014.

[104] J. F. Shackelford, Y.-H. Han, S. Kim, and S.-H. Kwon, *CRC materials science and engineering handbook*. CRC Press 1st ed., 2016.

[105] M. W. Chase, "NIST-JANAF thermochemical tables," *Journal of Physical and Chemical Reference Data*, vol. 9, 1998.

[106] P. Patsalas, C. Charitidis, S. Logothetidis, C. Dimitriadis, and O. Valassiades, "Combined electrical and mechanical properties of titanium nitride thin films as metallization materials," *Applied Physics*, vol. 86, no. 9, pp. 5296–5298, 1999.

[107] Y. O. Barmenkov, D. Zalvidea, S. Torres-Peiró, J. L. Cruz, and M. V. Andrés, "Effective length of short Fabry-Perot cavity formed by uniform fiber Bragg gratings," *Opt. Express*, vol. 14, pp. 6394–6399, Jul 2006.

[108] W. Zhang and J. Yao, "Photonic generation of linearly chirped microwave waveforms using a silicon-based on-chip spectral shaper incorporating two linearly chirped waveguide Bragg gratings," *Journal of Lightwave Technology*, vol. 33, no. 24, pp. 5047–5054, 2015.

[109] F. Falconi, C. Porzi, G. J. Sharp, M. Sorel, and A. Bogoni, "Widely tunable silicon photonics narrow-linewidth passband filter based on phase-shifted waveguide bragg grating," in *2018 International Topical Meeting on Microwave Photonics (MWP)*, pp. 1–4, 2018.

[110] A. B. Dar and R. K. Jha, "Design and comparative performance analysis of different chirping profiles of tanh apodized fiber bragg grating and comparison with the dispersion compensation fiber for long-haul transmission system," *Journal of Modern Optics*, vol. 64, no. 6, pp. 555–566, 2017.

[111] R. Cheng, Y. Han, and L. Chrostowski, "Characterization and compensation of apodization phase noise in silicon integrated Bragg gratings," *Opt. Express*, vol. 27, pp. 9516–9535, Apr 2019.

[112] M. Zhang, B. Buscaino, C. Wang, A. Shams-Ansari, C. Reimer, R. Zhu, J. M. Kahn, and M. Lončar, "Broadband electro-optic frequency comb generation in a lithium niobate microring resonator," *Nature*, vol. 568, pp. 373–377, Apr 2019.

[113] M. Khalil, R. Maram, B. Naghdi, A. Samani, M. Jacques, L. R. Chen, and D. V. Plant, "Electro-optic frequency comb generation using cascaded silicon microring modula-

tors," in *OSA Advanced Photonics Congress (AP) 2020 (IPR, NP, NOMA, Networks, PVLED, PSC, SPPCom, SOF)*, p. IM3A.6, Optica Publishing Group, 2020.

[114] Z. Wang, M. Ma, H. Sun, M. Khalil, X. Jin, K. Yim, L. R. Chen, and R. Adams, "On-chip frequency comb generation using cascaded MZMs in SiP for microwave photonics applications," in *2019 International Topical Meeting on Microwave Photonics (MWP)*, pp. 1–3, 2019.

[115] S. Liu, K. Wu, L. Zhou, L. Lu, B. Zhang, G. Zhou, and J. Chen, "Optical frequency comb and Nyquist pulse generation with integrated silicon modulators," *IEEE Journal of Selected Topics in Quantum Electronics*, vol. 26, no. 2, pp. 1–8, 2020.

[116] P. Sekhar, C. Fredrick, D. R. Carlson, Z. L. Newman, and S. A. Diddams, "20 GHz fiber-integrated femtosecond pulse and supercontinuum generation with a resonant electro-optic frequency comb," *APL Photonics*, vol. 8, p. 116111, 11 2023.

[117] D. R. Carlson, D. D. Hickstein, and S. B. Papp, "Broadband, electro-optic, dual-comb spectrometer for linear and nonlinear measurements," *Opt. Express*, vol. 28, pp. 29148–29154, Sep 2020.

[118] E. Lucas, P. Brochard, R. Bouchand, S. Schilt, T. Südmeyer, and T. J. Kippenberg, "Ultralow-noise photonic microwave synthesis using a soliton microcomb-based transfer oscillator," *Nature Communications*, vol. 11, p. 374, Jan 2020.

[119] T. M. Fortier, M. S. Kirchner, F. Quinlan, J. Taylor, J. C. Bergquist, T. Rosenband, N. Lemke, A. Ludlow, Y. Jiang, C. W. Oates, and S. A. Diddams, "Generation of ultrastable microwaves via optical frequency division," *Nature Photonics*, vol. 5, pp. 425–429, Jul 2011.

[120] P. J. Winzer, D. T. Neilson, and A. R. Chraplyvy, "Fiber-optic transmission and networking: the previous 20 and the next 20 years," *Optics Express*, vol. 26, no. 18, pp. 24190–24239, 2018.

[121] Y. Mao, Z. Lu, J. Liu, P. J. Poole, and G. Liu, "Pulse timing jitter estimated from optical phase noise in mode-locked semiconductor quantum dash lasers," *Journal of Lightwave Technology*, vol. 38, no. 17, pp. 4787–4793, 2020.

[122] M. AL-QADI, C. Laperle, D. Charlton, M. O'Sullivan, C. Xie, and R. Hui, "Multi-channel 16-QAM single-sideband transmission and kramers–kronig detection using a single QD-MLL as the light source," *Journal of Lightwave Technology*, vol. 38, no. 22, pp. 6163–6169, 2020.

[123] J. N. Kemal, P. Marin-Palomo, V. Panapakkam, P. Trocha, S. Wolf, K. Merghem, F. Lelarge, A. Ramdane, S. Randel, W. Freude, and C. Koos, "Coherent WDM transmission using quantum-dash mode-locked laser diodes as multi-wavelength source and local oscillator," *Optics Express*, vol. 27, no. 22, pp. 31164–31175, 2019.

[124] M. T. A. Khan, E. Alkhazraji, A. M. Ragheb, H. Fathallah, K. K. Qureshi, S. Alshebeili, and M. Z. M. Khan, "100 Gb/s single channel transmission using injection-locked 1621 nm quantum-dash laser," *IEEE Photonics Technology Letters*, vol. 29, no. 6, pp. 543–546, 2017.

[125] V. Vujicic, A. Anthur, V. Panapakkam, R. Zhou, Q. Gaimard, K. Merghem, F. Lelarge, A. Ramdane, and L. P. Barry, "Tbit/s optical interconnects based on low linewidth quantum-dash lasers and coherent detection," in *2016 Conference on Lasers and Electro-Optics (CLEO)*, pp. 1–2, 2016.

[126] J. Pfeifle, I. Shkarban, S. Wolf, J. N. Kemal, C. Weimann, W. Hartmann, N. Chimot, S. Joshi, K. Merghem, A. Martinez, M. Weber, A. Ramdane, F. Lelarge, W. Freude, and C. Koos, "Coherent terabit communications using a quantum-dash mode-locked laser and self-homodyne detection," in *2015 Optical Fiber Communications Conference and Exhibition (OFC)*, pp. 1–3, 2015.

[127] M. Gay, A. O'Hare, L. Bramerie, Z. Hao, S. Fresnel, C. Peucheret, P. Besnard, S. Joshi, S. Barbet, and F. Lelarge, "Single quantum dash mode-locked laser as a comb-generator in four-channel 112 Gbit/s WDM transmission," in *OFC 2014*, pp. 1–3, 2014.

[128] M. Khalil, Y. Xie, E. Berikaa, J. Liu, Z. Lu, P. J. Poole, G. Liu, J. Weber, D. V. Plant, and L. R. Chen, "Performance of quantum-dash mode-locked lasers (QD-MLLDs) for high-capacity coherent optical communications," *Opt. Express*, vol. 32, pp. 217–229, Jan 2024.

[129] M. Khalil, E. Berikaa, M. S. Alam, K. A. Shahriar, Y. Xie, J. Liu, Z. Lu, P. J. Poole, J. Weber, D. V. Plant, and L. R. Chen, "Performance of quantum-dash mode-locked laser diode (QD-MLLD) for data rates beyond tb/s in WDM coherent transmission over 80 km-SMF," in *Advanced Photonics Congress 2023*, p. SpW4E.2, Optica Publishing Group, 2023.

[130] D. Zhou, R. Piron, M. Dontabactouny, E. Homeyer, O. Dehaese, T. Batte, M. Gicquel, F. Grillot, K. Tavernier, J. Even, and S. Loualiche, "Effect of stack number on the threshold current density and emission wavelength in quantum dash/dot lasers," *physica status solidi c*, vol. 6, no. 10, pp. 2217–2221, 2009.

[131] M. Z. M. Khan, T. K. Ng, U. Schwingenschlogl, P. Bhattacharya, and B. S. Ooi, "Effect of the number of stacking layers on the characteristics of quantum-dash lasers," *Opt. Express*, vol. 19, pp. 13378–13385, Jul 2011.

[132] T. Habruseva, S. O'Donoghue, N. Rebrova, F. Kéfélian, S. P. Hegarty, and G. Huyet, "Optical linewidth of a passively mode-locked semiconductor laser," *Optics Letters*, vol. 34, no. 21, pp. 3307–3309, 2009.

[133] R. Rosales, K. Merghem, A. Martinez, F. Lelarge, A. Accard, and A. Ramdane, "Timing jitter from the optical spectrum in semiconductor passively mode locked lasers," *Opt. Express*, vol. 20, no. 8, pp. 9151–9160, 2012.

[134] H. Haus and A. Mecozzi, "Noise of mode-locked lasers," *IEEE Journal of Quantum Electronics*, vol. 29, no. 3, pp. 983–996, 1993.

[135] J. Reid, D. T. Cassidy, and R. T. Menzies, "Linewidth measurements of tunable diode lasers using heterodyne and etalon techniques," *Appl. Opt.*, vol. 21, pp. 3961–3965, Nov 1982.

[136] T. Okoshi, K. Kikuchi, and A. Nakayama, "Novel method for high resolution measurement of laser output spectrum," *Electronics Letters*, vol. 16, pp. 630–631, 1980.

[137] E. Bava, G. Galzerano, and C. Svelto, "Frequency-noise sensitivity and amplitude-noise immunity of discriminators based on fringe-side Fabry–Pérot cavities," *IEEE Transactions on Ultrasonics, Ferroelectrics, and Frequency Control*, vol. 49, no. 8, pp. 1150–1159, 2002.

[138] Y. Ben M'Sallem, Q. T. Le, L. Bramerie, Q.-T. Nguyen, E. Borgne, P. Besnard, A. Shen, F. Lelarge, S. LaRochelle, L. A. Rusch, and J.-C. Simon, "Quantum-dash

mode-locked laser as a source for 56-Gb/s DQPSK modulation in WDM multicast applications," *IEEE Photonics Technology Letters*, vol. 23, no. 7, pp. 453–455, 2011.

[139] R. Maldonado-Basilio, S. Latkowski, and P. Landais, "720-fs pulse generation with 40 GHz passively-mode locked quantum-dash Fabry-Pérot laser," in *2009 35th European Conference on Optical Communication*, pp. 1–2, 2009.

[140] A. Yadav, N. B. Chichkov, E. A. Avrutin, A. Gorodetsky, and E. U. Rafailov, "Edge emitting mode-locked quantum dot lasers," *Progress in Quantum Electronics*, vol. 87, p. 100451, 2023.

[141] Y.-C. Xin, D. J. Kane, V. Kovanis, N. G. Usechak, and L. F. Lester, "Frequency resolved optical gating characterization of a passively mode-locked quantum dot laser," in *Frontiers in Optics 2008/Laser Science XXIV/Plasmonics and Metamaterials/Optical Fabrication and Testing*, p. FThS3, Optica Publishing Group, 2008.

[142] C. Iaconis and I. A. Walmsley, "Spectral phase interferometry for direct electric-field reconstruction of ultrashort optical pulses," *Opt. Lett.*, vol. 23, pp. 792–794, May 1998.

[143] T. Rahman, S. Calabrò, N. Stojanovic, L. Zhang, J. Wei, and C. Xie, "LUT-assisted pre-compensation for 225 Gb/s/λ O-band transmission," in *45th European Conference on Optical Communication (ECOC 2019)*, pp. 1–4, 2019.

[144] S. J. Savory, "Digital coherent optical receivers: Algorithms and subsystems," *IEEE Journal of Selected Topics in Quantum Electronics*, vol. 16, no. 5, pp. 1164–1179, 2010.

[145] P. Ciblat and M. Ghogho, "Blind NLLS carrier frequency-offset estimation for QAM, PSK, and PAM modulations: performance at low SNR," *IEEE Transactions on Communications*, vol. 54, no. 10, pp. 1725–1730, 2006.

[146] I. Fatadin, D. Ives, and S. J. Savory, "Compensation of frequency offset for differentially encoded 16- and 64-QAM in the presence of laser phase noise," *IEEE Photonics Technology Letters*, vol. 22, no. 3, pp. 176–178, 2010.

[147] K. Roberts, Q. Zhuge, I. Monga, S. Gareau, and C. Laperle, "Beyond 100 Gb/s: capacity, flexibility, and network optimization [invited]," *Journal of Optical Communications and Networking*, vol. 9, no. 4, pp. C12–C23, 2017.

[148] S. Zhalehpour, M. Guo, J. Lin, Z. Zhang, H. Sepehrian, Y. Qiao, W. Shi, and L. A. Rusch, "All silicon IQ modulator with 1Tb/s line rate," in *2020 Optical Fiber Communications Conference and Exhibition (OFC)*, pp. 1–3, 2020.

[149] Z. Zheng, A. Mohammadi, X. Zhang, W. Shi, and L. A. Rusch, "Pushing capacity limits with multi-segment SiP modulators," *Journal of Lightwave Technology*, vol. 41, no. 19, pp. 6176–6186, 2023.

[150] A. Samani, M. Chagnon, D. Patel, V. Veerasubramanian, S. Ghosh, M. Osman, Q. Zhong, and D. V. Plant, "A low-voltage 35-GHz silicon photonic modulator-enabled 112-Gb/s transmission system," *IEEE Photonics Journal*, vol. 7, no. 3, pp. 1–13, 2015.

[151] R. Kuang and N. Bettenburg, "Quantum public key distribution using randomized Glauber states," in *2020 IEEE International Conference on Quantum Computing and Engineering (QCE)*, pp. 191–196, 2020.

[152] A. Chan, M. Khalil, K. A. Shahriar, D. V. Plant, L. R. Chen, and R. Kuang, "Encryption in phase space for classical coherent optical communications," *Scientific Reports*, vol. 13, p. 12965, Aug 2023.

[153] A. Chan, M. Khalil, K. A. Shahriar, L. R. Chen, D. V. Plant, and R. Kuang, "On the security of an optical layer encryption using coherent-based TF-QKD in classical optical fiber links," in *2022 4th International Conference on Computer Communication and the Internet (ICCCI)*, pp. 105–110, 2022.

[154] M. Khalil, A. Chan, K. A. Shahriar, L. R. Chen, D. V. Plant, and R. Kuang, "Security performance of public key distribution in coherent optical communications links," in *2021 3rd International Conference on Computer Communication and the Internet (ICCCI)*, pp. 123–129, 2021.

[155] A. Chan, M. Khalil, K. A. Shahriar, L. R. Chen, D. V. Plant, and R. Kuang, "Security analysis of a next generation TF-QKD for secure public key distribution with coherent detection over classical optical fiber networks," in *2021 7th International Conference on Computer and Communications (ICCC)*, pp. 416–420, 2021.

[156] K. A. Shahriar, M. Khalil, A. Chan, L. R. Chen, R. Kuang, and D. V. Plant, "Enhancing data security in optical fiber communication through dual layer encryption with randomized phases," in *Frontiers in Optics + Laser Science 2022 (FIO, LS)*, Technical Digest Series, (Rochester, New York), p. JW5A.80, Optica Publishing Group, Oct 2022.

[157] K. A. Shahriar, M. Khalil, A. Chan, L. R. Chen, R. Kuang, and D. V. Plant, "Physical-layer secure optical communication based on randomized phase space in pseudo-3-party infrastructure," in *Conference on Lasers and Electro-Optics*, Technical Digest Series, (San Jose, California), p. SF4L.3, Optica Publishing Group, May 2022.

[158] R. Kuang and A. Chan, "Quantum encryption in phase space with displacement operators," *EPJ Quantum Technology*, vol. 10, p. 26, Jun 2023.

[159] J. Yu and J. Zhang, "Recent progress on high-speed optical transmission," *Digital Communications and Networks*, vol. 2, no. 2, pp. 65–76, 2016.

[160] J. He, R. A. Norwood, M. Brandt-Pearce, I. B. Djordjevic, M. Cvijetic, S. Subramaniam, R. Himmelhuber, C. Reynolds, P. Blanche, B. Lynn, and N. Peyghambarian, "A survey on recent advances in optical communications," *Computers & Electrical Engineering*, vol. 40, no. 1, pp. 216–240, 2014. 40th-year commemorative issue.

[161] M. P. Fok, Z. Wang, Y. Deng, and P. R. Prucnal, "Optical layer security in fiber-optic networks," *IEEE Transactions on Information Forensics and Security*, vol. 6, no. 3, pp. 725–736, 2011.

[162] N. Skorin-Kapov, M. Furdek, S. Zsigmond, and L. Wosinska, "Physical-layer security in evolving optical networks," *IEEE Communications Magazine*, vol. 54, no. 8, pp. 110–117, 2016.

[163] Q. Zhu, X. Yu, Y. Zhao, A. Nag, and J. Zhang, "Resource allocation in quantum-key-distribution- secured datacenter networks with cloud–edge collaboration," *IEEE Internet of Things Journal*, vol. 10, no. 12, pp. 10916–10932, 2023.

[164] D. Rosenberg, J. W. Harrington, P. R. Rice, P. A. Hiskett, C. G. Peterson, R. J. Hughes, A. E. Lita, S. W. Nam, and J. E. Nordholt, "Long-distance decoy-state quantum key distribution in optical fiber," *Phys. Rev. Lett.*, vol. 98, p. 010503, Jan 2007.

[165] A. Argyris, D. Syvridis, L. Larger, V. Annovazzi-Lodi, P. Colet, I. Fischer, J. García-Ojalvo, C. R. Mirasso, L. Pesquera, and K. A. Shore, "Chaos-based communications at high bit rates using commercial fibre-optic links," *Nature*, vol. 438, pp. 343–346, Nov 2005.

[166] C. Huang, P. Y. Ma, B. J. Shastri, P. Mittal, and P. R. Prucnal, "Robustness of optical steganographic communication under coherent detection attack," *IEEE Photonics Technology Letters*, vol. 31, no. 4, pp. 327–330, 2019.

[167] Z. Li and G. Li, "Ultrahigh-speed reconfigurable logic gates based on four-wave mixing in a semiconductor optical amplifier," *IEEE Photonics Technology Letters*, vol. 18, no. 12, pp. 1341–1343, 2006.

[168] C. H. Bennett and G. Brassard, "Quantum cryptography: Public key distribution and coin tossing," *Theoretical Computer Science*, vol. 560, pp. 7–11, 2014. Theoretical Aspects of Quantum Cryptography – celebrating 30 years of BB84.

[169] H. Wang, Y. Pi, W. Huang, Y. Li, Y. Shao, J. Yang, J. Liu, C. Zhang, Y. Zhang, and B. Xu, "High-speed gaussian-modulated continuous-variable quantum key distribution with a local local oscillator based on pilot-tone-assisted phase compensation," *Opt. Express*, vol. 28, pp. 32882–32893, Oct 2020.

[170] L. Yang, L. Zhang, R. Yang, L. Yang, B. Yue, and P. Yang, "Chaotic dynamics of erbium-doped fiber laser with nonlinear optical loop mirror," *Optics Communications*, vol. 285, no. 2, pp. 143–148, 2012.

[171] C. Xue, N. Jiang, Y. Lv, C. wang, G. Li, S. Lin, and K. Qiu, "Security-enhanced chaos communication with time-delay signature suppression and phase encryption," *Opt. Lett.*, vol. 41, pp. 3690–3693, Aug 2016.

[172] N. Jiang, A. Zhao, C. Xue, J. Tang, and K. Qiu, "Physical secure optical communication based on private chaotic spectral phase encryption/decryption," *Opt. Lett.*, vol. 44, pp. 1536–1539, Apr 2019.

[173] Z. Wang and P. R. Prucnal, "Optical steganography over a public DPSK channel with asynchronous detection," *IEEE Photonics Technology Letters*, vol. 23, no. 1, pp. 48–50, 2011.

[174] R. Lavrov, M. Jacquot, and L. Larger, "Nonlocal nonlinear electro-optic phase dynamics demonstrating 10 Gb/s chaos communications," *IEEE Journal of Quantum Electronics*, vol. 46, no. 10, pp. 1430–1435, 2010.

[175] M. Jinno and T. Matsumoto, "Ultrafast all-optical logic operations in a nonlinear sagnac interferometer with two control beams," *Opt. Lett.*, vol. 16, pp. 220–222, Feb 1991.

[176] J.-M. Mérolla, Y. Mazurenko, J.-P. Goedgebuer, H. Porte, and W. T. Rhodes, "Phase-modulation transmission system for quantum cryptography," *Opt. Lett.*, vol. 24, pp. 104–106, Jan 1999.

[177] M. A. Nielsen and I. L. Chuang, *Quantum Computation and Quantum Information: 10th Anniversary Edition*. Cambridge University Press, 2010.

[178] D. Dieks, "Overlap and distinguishability of quantum states," *Physics Letters A*, vol. 126, no. 5, pp. 303–306, 1988.

[179] M. G. Paris, "Displacement operator by beam splitter," *Physics Letters A*, vol. 217, no. 2, pp. 78–80, 1996.

[180] P. C. Schindler, R. Schmogrow, M. Dreschmann, J. Meyer, I. Tomkos, J. Prat, H.-G. Krimmel, T. Pfeiffer, P. Kourtessis, A. Ludwig, D. Karnick, D. Hillerkuss, J. Becker, C. Koos, W. Freude, and J. Leuthold, "Colorless FDMA-PON with flexible bandwidth

allocation and colorless, low-speed ONUs [invited]," *Journal of Optical Communications and Networking*, vol. 5, no. 10, pp. A204–A212, 2013.

[181] S. Varughese, D. Lippiatt, S. Tibuleac, and S. E. Ralph, "Frequency dependent ENoB requirements for 400G/600G/800G optical links," *Journal of Lightwave Technology*, vol. 38, no. 18, pp. 5008–5016, 2020.

[182] T. Pfau, S. Hoffmann, and R. Noe, "Hardware-efficient coherent digital receiver concept with feedforward carrier recovery for M-QAM constellations," *Journal of Lightwave Technology*, vol. 27, no. 8, pp. 989–999, 2009.

[183] S. Mrdovic and B. Perunicic, "Kerckhoffs' principle for intrusion detection," in *Networks 2008 - The 13th International Telecommunications Network Strategy and Planning Symposium*, vol. Supplement, pp. 1–8, 2008.